SUPERPLASTIC BEHAVIOUR OF SHEET MATERIALS

UNDER

BIAXIAL STRESSES

SUPERPLASTIC BEHAVIOUR OF SHEET MATERIALS UNDER BIAXIAL STRESSES

by

ISMAIL MORADI-BIDHENDI, B.Sc., M.Sc.

THE UNIVERSITY OF ASTON IN BIRMINGHAM

A thesis submitted for the degree of

DOCTOR OF PHILOSOPHY

Department of Mechanical Engineering

The University of Aston in Birmingham

June 1981

Superplastic behaviour of sheet materials under biaxial stresses

ISMAIL MORADI-BIDHENDI

Submitted for the degree of Doctor of Philosophy of the University of Aston in Birmingham

June 1981

Summary

The deformation of a superplastic zinc-aluminium eutectoid alloy is examined by subjecting thin circular diaphragms to one-sided hydrostatic pressure at elevated temperature. The geometry, the stress, the strain, and the strain-rate are determined at various points covering the whole specimen and at various stages of the forming process.

One distinctive feature of this study is the use of the curvatures of the thin shell for the stress analysis. It is shown that the ratio of the two principal stresses at a point in the formed shell is related in a simple way to the ratio between the principal curvatures at that point. In fact the ratio between the principal curvatures is also a measure of the deviation of the local geometry from the spherical shape.

The rheological properties of the material under this biaxial stress system are presented in triangular coordinates. The nature of the stresses, strains and strain-rates at the dome and the rim of the bulge are discussed in detail. It is shown that the strain rates vary widely in the material at different regions. The biaxial stress is analysed into a strain proportional and a strain-rate proportional component which represent respectively, the quasi-solid and the quasi-liquid behaviour of the superplastic material.

Keywords: Bulge test
superplastic
zinc-aluminium alloy

ACKNOWLEDGMENTS

The author wishes to express his gratitude and sincere thanks to the following:

Professor T.C. Hsü, under whose supervision the work was carried out, for his help and encouragement at all stages of the project.

Professor K. Foster, Head of the Department of Mechanical Engineering, for permitting the use of all the equipment in the Department.

All the technicians in the Department of Mechanical Engineering, for their help in the acquisition and manufacture of apparatus, in particular Messrs. H. Pratt, D. Green and G. Watson.

Mrs. H. Papadopoulos, for carefully typing the manuscript.

Finally, my wife Hideh, for her help and support during the years of this research.

* * * *

CONTENTS

LIST OF FIGURES

NOTATION

A	cross sectional area
a	radius of die hole
b	strain hardening index
D	diameter
F	resultant force
F( )	notation for functions
H	polar height
$\underline{i}$, $\underline{j}$, $\underline{k}$	unit vectors for principal stresses
K	a constant
L	tensile load
ℓ	longitudinal displacement of specimen
m	strain-rate sensitivity index
N	index of sphericality
P	pressure
$\bar{p}$	prolateness of a surface of revolution
R	radius of spherical shell
r	radial distance during deformation
S	arc length of the meridian section
T	time
t	through-thickness of the specimen
v	volume of the shell
z	ratio of the solid to liquid behaviour

α , β	angle of any position vector in the triangular coordinate system
δ	differential operator
ε	natural strain
ε_1 , ε_2 , ε_3	principal strains
$\bar{\varepsilon}$	effective strain
$\dot{\varepsilon}$	natural strain-rate
$\dot{\varepsilon}_1$, $\dot{\varepsilon}_2$, $\dot{\varepsilon}_3$	principal strain-rates
$\bar{\dot{\varepsilon}}$	effective strain-rate
ζ	characteristic index for stress
η	characteristic index for strain
θ	angle of inclination of meridian section
ρ	principal radius of curvature
σ	flow stress
σ_1 , σ_2 , σ_3	principal stresses
$\bar{\sigma}$	effective stress
σ_m	hydrostatic stress
σ'	deviatoric stress
τ	shear stress
ϕ	angle subtended by ρ_s through the pole and die edge for a spherical bulge

Notes

A dot ($\cdot$) above a parameter	refers to the first derivative with respect to time
Suffix o	refers to original dimension

Suffix θ, s, t	refers to circumferential, meridional-tangential and through-thickness directions respectively.
suffix p	refers to the pole of the bulge
∂	refers to partial derivative
$\int d\bar{\varepsilon}$	length of strain path

CHAPTER 1

INTRODUCTION

Chapter 1

INTRODUCTION

Superplastic alloys have been considered by engineers and metallurgists with less than perfect justification, to be materials of exceptionally high ductility. Actually, superplasticity is not a matter of ductility, which is defined by the strain at fracture under quasi-static conditions, but is due to the dependence of flow stress on the strain rate, in other words, it is a rheological phenomenon. The basis of superplasticity is neither in the late development of the localised neck in the material when stretched, nor in the large strain at the fracture, but lies in the fact that the neck does not aggravate itself after it is formed, the strain-rate effect on the flow stress preventing the formation of the highly localised necking in the tension test specimens of ordinary ductile metals.

The deformation characteristics of some superplastic materials are similar to those of heated thermoplastics and consequently certain forming processes developed by the plastics industries are applicable to superplastic sheet metal forming processes. Most of these forming operations involve free bulging of the material, at one stage or another. Therefore the axisymmetrical bulge test seems to be the most suitable test to predict the mechanical behaviour of these materials under biaxial tensile stress.

The bulge test, widely used for determining the ductility of sheet materials, consists of clamping the test material over a circular die hole and deforming the sheet with hydrostatic pressure on one side of it till it forms a bulge. The ductility of the test material is represented by the height of the bulge when fracture occurs. The hydrostatic pressure in the bulge test transmits a uniform pressure over the entire bulge during the test and the process is in a frictionless state. The failure usually occurs at the pole, where balanced biaxial stretching occurs. By making suitable grids onto the face of the specimen and measuring their geometrical transformation, the mechanical behaviour of the work material can be determined.

In the last decade a number of papers (56 - 67)* have been published on the bulge test of superplastic materials. In these papers flow stress is assumed to be a unique function of strain-rate and any strain dependence is neglected. This stress-strain rate relation is obtained from a uniaxial tensile test, using an empirical equation in the form

$$\sigma = k (\dot{\varepsilon})^m \qquad (1.1)$$

where σ is flow stress, k is a constant for any given testing conditions and is a function of grain size and temperature, $\dot{\varepsilon}$ is strain-rate and m is the strain-rate sensitivity index of the material defined as

$$m = \frac{\delta(\ln\sigma)}{\delta(\ln\dot{\varepsilon})} \qquad (1.2)$$

*Numbers in brackets designate reference at the end of the thesis.

The stress-strain-rate relations so obtained, are applied to stress states that are biaxial and in some cases triaxial, by using the effective stress and effective strain rate of plasticity theory. However, there is concern among some of the researchers about the validity of such concepts in this context.

In the bulge test of superplastic material, some investigators have introduced special assumptions in order to simplify the problem and bypass potentially difficult experimental measurements. These assumptions are as follows:

1. At any instant the membrane is equivalent to part of a thin sphere subjected to internal pressure (56), (58), (64 - 67).

2. The thickness of the bulge remains uniform at any stage of the forming operation (56), (66).

These assumptions, naturally cannot be simultaneously satisfied in the bulging of superplastic sheet material. The work presented in this thesis is therefore undertaken to analyse the deformation behaviour of superplastic material with a more realistic approach involving no assumptions of this type.

CHAPTER 2

LITERATURE SURVEY

Chapter 2

I - Physical metallurgy of superplasticity

2.1 The Historical Review

The first data on the viscous behaviour of eutectic alloys can be found in the paper published by W. Rosenhain et al (1) in 1920. A few years later, the exceptional ductile behaviour of some non-ferrous alloys was observed by F. Hargreaves (2) and C.H.M. Jenkins (3), whilst in 1934 Pearson (4) published a photograph of a tensile specimen of Sn - Bi alloy which had been fractured after 1950% elongation. He showed that in the case of extruded tin-lead entectic even higher ductility can be obtained.

It is surprising that these sensational results were ignored by both scientists and engineers for 28 years before the next paper on superplasticity was published in western literature (5).

However, the term "superplasticity" was first used in Russian literature (6) to describe the high ductility in combination with very low flow stress. The work of Bochvar and Sviderskaya (6) was the initiation of the intensive study of superplasticity in Russia.

The properties of alloys of Zn - Al system were studied and it was discovered that superplasticity only occurs with Zn - Al alloys in certain conditions of heat treatment. Research on these and other alloys (11 - 14) was continued in order to develop an understanding of this phenomenon and the

subject became fashionable in that country during the 1950's and 1960's (7).

The renaissance of superplasticity in the western literature was publication of a paper by Backofen and his co-workers (15) in 1964 in the U.S.A.. Since then hundreds of papers have been published concerning the basic facts, theoretical explanations and practical implications of superplasticity and it has become one of the most interesting research subjects throughout the world.

2.2 Types of Superplasticity

From the many studies that have been carried out, it is well understood that superplastic materials can be classified into two groups:-

1. Those in which a characteristic microstructure exists and which are said to exhibit "structural superplasticity", usually referred to as "micrograin" or "isothermal" superplasticity.
2. Those in which special environmental conditions are necessary and which are said to exhibit "environmental superplasticity".

2.3 Structural Superplasticity

The special microstructure conditions for a material to behave superplastically are:-

1. A fine equi-axed grain size of the order 1 to 10 μm which is stable under the conditions of deformation.
2. A working temperature above approximately half the absolute melting point.

3. The use of slow strain rates.

Structural superplasticity has received much more attention than environmental superplasticity. The reason is that if superplasticity is to be applied to commercial fabrication of metals, it would be more feasible to have the equipment operating at a constant temperature than to cycle it repeatedly over a range of temperatures as in the case of environmental superplasticity.

Structural superplasticity has been observed mostly in two-phase alloys, many of which are based on eutectic or eutectoid compositions, but relatively pure metals can also behave superplastically under special testing conditions (23). A list of known superplastic materials can be found in reference (22).

Two-phase alloys having fine-grained structure are called "microduplex structure". Such a structure can be created by a variety of methods (16 - 21), utilizing one or more of the familiar metallurgical processes of hot working, cold-working, recrystallization and precipitation. All of these processes are included in the general term "thermomechanical processing".

2.3.1 Proposed mechanisms

Several detailed explanations of the mechanisms have been proposed to account for structural superplasticity,

but it is not yet clear which deformation mechanism or combination of mechanisms predominate in these structures when superplastic deformation occurs.

It has been explained (23) that it is unrealistic to say that some of the proposed mechanisms apply to a very wide range of materials. However, the proposed theories are known as:
Nabarro-Herring diffusion creep (24 - 25), Coble creep (26) dislocation motion (27 - 28), Grain boundary sliding (29 - 30, 31 - 32), dynamic recrystallization (33 - 34), Grain boundary sliding with accommodation by dislocation motion (35 - 36), Grain rotation (37), Grain boundary sliding combined with diffusion creep (25), (39) and Grain boundary sliding combined with several Grain deformation mechanisms (40). It can be seen that current thinking leans toward a combination of proposed mechanisms depending upon the material and experimental conditions involved.

2.4 Environmental Superplasticity

This form of superplasticity occurs in a wide range of polycrystalline materials in a particular set of environmental conditions. There are three well-known conditions under which this phenomenon occurs:

1. During temperature cycling through a phase transformation.
2. During temperature cycling of a material with anisotropic thermal expansion.

3. During neutron irradiation.

Large elongations of 150 to 500% have been produced by a small tensile stress on the material in one of the above conditions. A list of known environmental superplastic materials can be found in reference (22).

The materials for which environmental superplasticity has been shown to occur are usually subjected to phase transformation. In the remaining two areas, relatively limited work has been reported.

2.4.1 Phase Transformation

Phase transformation superplasticity has been observed in a wide range of materials, especially ferrous alloys. It has been established that mechanical weakening occurs during phase transformation.

Saveur (41) is quoted to have first observed this phenomenon on iron during the $\alpha - \gamma$ transformation.

Lozinsky and Simeonova (42) exposed iron specimens (with 0.03%c) to a temperature gradient and simultaneously cycled the temperature of the hottest centre part between 800 °C and 1000 °C. Application of a small load resulted in localized deformation in the cooler part of the specimens. This was attributed to the occurrence of the phase transformation at the grain boundaries, where carbon segregation locally reduced the transformation point.

More systematic and quantitative experiments were carried out by De Jong and Rathenau (43) and Clinard and Sherby (44). The ferrous specimens were subjected to tension, torsion and compression tests during a temperature cycle and it was concluded that the type of loading has no special significance for the transformation plasticity. The amount of strain per cycle was found to depend linearly on stress in all experiments. Oelschlagel and Weiss (46) also observed this linear dependence in three plain carbon steels under constant loads during the phase transformation.

De Jong and Rathenau (43) reported a large value of strain during $\gamma - \alpha$ transformation on cooling, whereas Clinard and Sherby (44) found more elongation during heating ($\alpha - \gamma$ transformation). Variation of the heating and cooling rate also provided no clear result. While in (47) a change in the heating and cooling rate had no effect, in (44) a definite decrease in strain resulted from a further increased heating or cooling rate.

Enhanced plasticity was also observed in U, Zr, Fe and Co (46) during phase transformation.

2.4.2 Temperature Cycling

Some materials can be made superplastic by temperature cycling under a small applied load. One of the materials known to exhibit this behaviour is alpha-uranium. The internal stresses that account for its

superplastic behaviour under these conditions derive from the anisotropy of the thermal expansion coefficients of the single crystal. Large elongations (431% after 600 cycles between 400° and 600 °C) have been measured in an alloy known as adjusted uranium (48). Pure zinc has also been caused to exhibit superplasticity by thermal cycling in the experiments of Lobb et al (48). Elongation of up to 158% were recorded after 1664 cycles between 150° and 300 °C.

2.4.3 Irradiation

In 1955 Konobeevsky et al (49) reported that the creep of uranium metal increases under neutron irradiation. Roberts and Cottrell (50) showed that under neutron irradiation at 100°C alpha-uranium exhibits a steady state strain rate of 3×10^{-11} sec^{-1} under a stress of 1% of yield. The corresponding strain rate sensitivity $\hat{}^{(m)}$ was 0.8. However, large elongations have not been demonstrated because of the low strain-rate involved.

2.4.4 Proposed Mechanisms

In the early papers, superplasticity during a phase transformation was attributed to a temporary reduction in strength caused by position changes of the atoms. Roberts and Cottrell (50) argued that superplasticity can be produced by generation of the internal stresses considerably higher than the external stress. This was a satisfactory explanation which was expanded theoretically by Greenwood and Johnson (45), but they argued that the

plastic deformation is restricted to the weaker phase present during thermal cycling. Other theories are as follows:

dislocation motion (51), dislocation climb (44), dislocation pile-up (52), preferred alignment of martensite plates (53), work hardening (54).

II - Mechanical behaviour of superplastic materials

2.5 Tensile Test

Most of the data on the mechanical behaviour of superplastic materials has been obtained from uniaxial tensile tests. It will be shown later that the tensile test is far from being a satisfactory measure of superplasticity in an engineering sense. However, from the review of the results so obtained, conclusions can be drawn that the flow stress of structurally superplastic materials is a sensitive function of strain-rate, temperature and grain size. The details are described in the following sections.

2.5.1 Effect of Strain-Rate

In superplastic materials the flow stress is sensitive to the rate of deformation and a quantitative description is frequently given by an empirical equation of the form

$$\sigma = \kappa(\dot{\varepsilon})^m \qquad (2.1)$$

where σ is flow stress, κ is a constant for any given testing conditions and is a function of grain size and temperature, $\dot{\varepsilon}$ is a strain-rate and m is the strain-rate sensitivity index of the material defined as

$$m = \frac{\delta \ln \sigma}{\delta \ln \dot{\varepsilon}} \qquad (2.2)$$

Conventionally, superplasticity is measured by the strain-rate sensitivity index, and the total ductility observed

in the tensile test is attributed to high values of m (15).

The requirement of a high value of m is often demonstrated by substituting in Eq (2.1) for σ and $\dot{\varepsilon}$ in terms of tensile load L, the cross sectional area A and time T

$$\sigma = \frac{L}{A} \qquad (2.3)$$

$$\dot{\varepsilon} = -\frac{1}{A}\frac{dA}{dT} \qquad (2.4)$$

the rate at which any area decreases can be expressed as

$$-\frac{dA}{dT} = \left(\frac{L}{K}\right)^{1/m} . (A)^{\frac{m-1}{m}} \qquad (2.5)$$

Eq. (2.5) shows that when m approaches unity, $\frac{dA}{dT}$ becomes increasingly independent of A, and when m = 1 (Newtonian flow),

$$-\frac{dA}{dT} = \frac{L}{K} \qquad (2.6)$$

i.e. the rate of reduction in cross-sectional area is dependent only on load and independent of the area of the specimen. For superplastic materials parameter m normally has a value between 0.4 and 0.9 (22), compared with a value of unity for ideal Newtonian fluid behaviour. Eq. (2.5) also shows that any local stress increase, produces only a small change in strain-rate and as a result such regions deform at a rate not significantly different from the rest of the specimen.

Nuttall (79) has shown the relationship between the flow stresses and strain rate as straight lines, plotted on logarithmic scales, Fig. (2.1). It can readily be seen from this figure that m is constant and independent of strain-rate for a given working temperature and grain size, and its magnitude is the slope of the line for any particular temperature.

Except Nuttall (79), all other investigators have reported a characteristic sigmoidal variation of the flow stress with strain-rate for constant temperature. The behaviour may therefore be divided into three regions (see Fig. 2.2). Here regions I and III correspond to $m \leq 0.3$ at very low and high values of the imposed strain-rate respectively, while at intermediate strain rate (10^{-3} - 10^{-1} s^{-1}, region II) m increases to ~ 0.5 and this region is the superplastic regime where very large elongations occur.

Several methods have been established to determine the log σ/log $\dot{\varepsilon}$ relation. In most cases, a series of incremental strain-rate changes are imposed on a single specimen and the flow stress corresponding to each strain-rate measured and plotted as log σ vs. log $\dot{\varepsilon}$. In this case it is assumed that the flow stress is independent of strain and that no necking occurs. However, there is a controversy about the effect of strain on the flow stress. Nicholson (18) found that, for a Zn - Al eutectoid alloy tested at constant strain-rate, the value of the strain

hardening index b in the stress-strain relationship

$$\sigma = \kappa \varepsilon^{b} \qquad (2.7)$$

was ∿0.06 and concluded that this small dependence of stress upon strain does not represent true work hardening in the conventional way but a slight instability in the structure of the superplastic alloy. This conclusion has been supported by other investigators (81 - 82).

The results obtained by Fields and Hubert (80), on the other hand were quite different. They found that the behaviour of Zn - Al eutectoid alloy depends on the processing of the material. Results from a tensile test at constant cross-head speed on the alloy in the quenched condition showed strain softening during superplastic deformation, (see Fig. 2.3), whereas in the quenched and cold rolled condition it tended to strain harden, (Fig.2.4). The evidence obtained by these investigators is not conclusive as the data was obtained from a tensile test performed at constant cross-head speed, rather than at constant strain-rate.

As mentioned earlier, the strain rate sensitivity index (m) is an important parameter in superplasticity, and there are at least five different methods of measurement for the m value, which are fully explained in reference (22).

2.5.2 Effect of Temperature

As mentioned in section 2.3, structural superplasticity is a high-temperature phenomenon, occurring at

about half the homologous melting point. The effect of temperature on superplastic flow is well documented for a wide range of materials in terms of the strain-rate sensitivity index m. Fig. (2.5) shows a plot of temperature against strain-rate sensitivity index for quenched Al - 80% Zn alloy for a constant strain-rate test. As seen in this figure, the highest degree of superplastic behaviour (i.e. maximum m value) in Al - 80% Zn alloy occurs around 260 °C. Furthermore, by increasing the deformation temperature, the overall level of the flow stress can be reduced (see Fig. 2.2 and Fig. 2.6).

2.5.3 Effect of Grain Size

In structural superplasticity, one of the conditions for a material to behave superplastically is having a fine equi-axed grain size of the order 1 to 10 μm. The quantitative relation of flow stress to grain size is not yet clear from the published work. However, the following relations have been frequently used to describe the influence of grain size on the flow stress and strain-rate,

$$\sigma \propto L^{b} \quad \text{and} \quad \dot{\varepsilon} \propto 1/L^{a} \qquad (2.8)$$

where L is the mean grain diameter and the values of a and b depend upon material temperature and thermal history of the material (22). Fig. (2.6) shows the variation of flow stress with temperature at constant strain-rate for Zn - Al entectoid alloy at three different grain sizes. The figure indicates that there should be a direct proportionality between stress and some power of

the grain size.

Eq. (2.1) appears to be simple enough for stress analysis in the uniaxial tensile test. In a metal forming operation, however, strain-rates vary widely in the material at different regions and therefore m cannot be taken as a constant. Furthermore, superplastic sheet metal forming processes involve the biaxial stretching of the material and in this stress system the analysis of the superplastic properties of the sheet are more complex than those of a superplastic rod in uniaxial tension. For these reasons, the bulge test has been used extensively to analyse the mechanical behaviour of superplastic materials.

2.6 Bulge Test

The bulge test is a widely used sheet metal test to examine the ductility of sheet materials under any biaxial stress system. This test provides a means of studying stress-strain relationships and strain-hardening characteristics of the conventional materials.

In superplastic forming, the bulge test is of great importance, as most of the forming operations involve free bulging at one stage or another. Therefore, this simple test enables a quantitative account to be given of the effect of the flow stress, strain-rate and all the other parameters involved.

Several papers have been devoted to experimental and theoretical studies of the hydrostatic bulging of superplastic sheet materials.

2.6.1 Experimental Investigations

Backofen and his colleagues (15) were among the first to examine the possibility of deformation of superplastic sheets by the method of bulging under gas pressure. Their interest grew out of curiosity about the bulging limits of such materials. A dome was formed with the height far greater than had ever been seen in a pure metal or alloy. They did not report any quantitative work on bulging behaviour of superplastic material. However, a few investigators tackled the problem with different objectives using different methods.

Thomsen and his colleagues (57) examined the variation in the mean meridian strain and the distribution of the thickness as a function of strain rate sensitivity (m) and pressure.

A range of m values was developed for Zn - Al eutectoid and Sn - Pb eutectic superplastic alloys at different temperatures, using the strain-rate change technique in the uniaxial tension test described by Backofen et al (15). The mean meridian strain was defined as:

$$\bar{\varepsilon} = (C/D) - 1 \qquad (2.9)$$

where D is the initial diameter of the die hole and C is the length of the meridian line on the bulge.

The fractional thickness reduction was defined as:

$$R = 1 - (S/S_o) \qquad (2.10)$$

where S_o and S are the initial and final sheet thicknesses respectively. A set of graphs were plotted to show the development of non-uniform thickness in the bulge.

These authors concluded that, by increasing m, the height of the pole before tearing can be raised, the overall shape becomes more nearly spherical and the wall thickness becomes more nearly uniform. Similar results were also reported by Hestbech et al (58) for Zn - Al eutectoid alloy. In the former work, no attempt was made to show the effect of the grain size on thickness distribution and flow stress, whereas in the latter, it was shown that the large grained specimens have a higher flow stress than the fine grained specimens and average distribution of the thickness is independent of grain size and strain-rate. They also reported that the value of m is independent of grain size.

There is a certain contradiction between these results and those obtained from tensile tests in the other investigations (55), (59). The approach adopted by Al-Naib (60) was totally different from those mentioned above. A special machine consisting of two chambers was built, a Zn - Al eutectoid sheet specimen was clamped between the chambers and air pressure applied to bulge the specimen. When the bulge radius of curvature reached that of the chamber, the expansion became a combined free

bulge and draw along the chamber wall, therefore the process was not a true free bulge forming. However, he showed that the thickness distribution remained constant along the wall irrespective of the polar height, which indicated that the deformation of the material ceased once it made contact with the wall. This interesting feature was used to develop a technique to form top-hats with nearly uniform wall thickness (60).

Al-Naib assumed that the profile of the bulge is always spherical and the locus of any point on the deforming sheet is a circular arc whose centre of curvature is in the plane of the undeformed sheet. On the basis of these assumptions he attempted to formulize a relationship between forming pressure, time, material constant parameters κ and m and bulge height. His results, however, could not be considered reliable because the process was not a true bulge test.

Cocks and his colleagues (61) examined the bulge forming characteristics of two superplastic copper alloys (Cu-9.5 Al-4Fe, and Cu-0.4Co - 2.8 Al - 1.8Si) and showed that the true thickness strains for these alloys are lower than those predicted by Cornfield and Johnson (64) for titanium alloy and stainless steel. They suggested that this could be accounted for by material being drawn from between the clamped edges of the die which was not considered by Cornfield and Johnson (64).

2.6.2 Theoretical Investigations

In addition to experimental investigations on the bulge test, several attempts have been made to predict the superplastic behaviour of materials for this process (56), (59), (64 - 69). Two types of theoretical predictions can be classified. The first type belongs to the special solution in which the bulge shape is assumed before stresses and strain rates are predicted for successive polar heights (56), (66). The second type of prediction is referred to as a numerical solution in which displacements and shape of the bulge for various polar heights are predicted by iteration techniques on a computer (59), (64), (68).

Whether by special or numerical solution the general line of approach to the prediction is the same. The previous investigations are reviewed in the following sections:-

(a) - main assumptions

(b) - constitutive equations

(c) - stress-strain rate-relationship

(d) - comparison of predicted and actual results

(a) Main assumptions

The problem of the bulge test has unanimously been simplified by the following general assumptions:

1 - The material is isotropic.

2 - The material is incompressible so that the three principal strains add up to zero,

$$\text{i.e.} \quad \varepsilon_\theta + \varepsilon_s + \varepsilon_t = 0 \qquad (2.11)$$

3 - Elastic strains are negligible

4 - The material does not work harden and flows under any load.

5 - The thickness to diameter ratio of the membrane is very small and bending effects are negligible.

6 - At the periphery, the diaphragm is rigidly clamped and deforms as a frictionless hinge.

7 - The flow stress σ is strongly dependent on the strain rate $\dot{\varepsilon}$ in accordance with Eq. (2.1), i.e. $\sigma = \kappa(\dot{\varepsilon})^m$.

In addition to the general assumptions mentioned above, some investigators introduced special assumptions and over-simplified the problem and hence affected the accuracy of the solution to different extents.

These assumptions are as follows:-

1 - At any instant the membrane is equivalent to part of a thin sphere subject to internal pressure (56), (59), (64 - 66), (68).

2 - The thickness of the bulge remains uniform at any stage of the forming operation (56), (66).

(b) Constitutive equations

On the basis of the above assumptions, there are certain relationships and equations which can be divided into two groups:

(1) The kinematic relations between displacement and shapes on the one hand, and strains and strain-rates on the other hand.

(2) The equations which relate the specimen shape and the hydrostatic pressure with the stresses.

For a spherical bulge, the material everywhere along the profile is subjected to balanced biaxial stretching. Therefore, it can easily be deduced that the radius of curvature (ρ) is

$$\rho = \frac{a^2 + H^2}{2H} \qquad (2.12)$$

where a is the radius of the die hole and H is the height of the bulge.

The natural through thickness strain is

$$\varepsilon_t = \ln \frac{t}{t_o} \qquad (2.13)$$

where t and t_o are current and initial thickness respectively.

For a spherical bulge, the incompressibility condition of metals Eq. (2.11) together with Eq. (2.13) are sufficient to determine the state of strain. Thus,

$$\varepsilon_t = -2\varepsilon_s = -2\varepsilon_\theta = \ln \frac{t}{t_o} \qquad (2.14)$$

where ε_s is meridianal tangential strain and ε_θ is circumferential strain.

For the measurement of strain and strain-rate, Belk (66) adopted a different approach. He measured the

average natural strain defined as:

$$\varepsilon = \ln \left(\frac{\text{new surface area}}{\text{original surface area}} \right)$$

For a spherical bulge this becomes

$$\varepsilon = \ln \frac{\pi(a^2 + H^2)}{\pi a^2}$$

$$= \ln \left(1 + \frac{H^2}{a^2}\right) \qquad (2.15)$$

Hence, the average strain rate is

$$\dot{\varepsilon} = \frac{d\varepsilon}{dT} = \frac{2H}{H^2+a^2} \frac{dH}{dT} \qquad (2.16)$$

The balanced biaxial stresses can be calculated from the following equation

$$\sigma = \frac{P}{2t} \rho$$

$$= \frac{P}{2t} \left(\frac{a^2 + H^2}{2H}\right) \qquad (2.17)$$

(c) Stress-strain-rate relationship

In the previous papers (56 - 61), (64), (66 - 69), the mechanical behaviour of structural superplasticity is frequently described by the well-known empirical uniaxial stress-strain-rate relationship

$$\sigma = \kappa(\dot{\varepsilon})^m$$

In this equation, m is assumed to be constant for a given temperature, strain rate and grain size.

Tang and Robbins (65) argued that the range of strain-rates involved in the bulge test is quite wide. There-

fore, m cannot be taken as a constant. In addition to that, the grain size also has no role in this equation. Hence, they adopted the empirical relationship proposed by Avery and Backofen (24)

$$\text{i.e.} \quad \dot{\varepsilon} = \frac{A' \sigma^2}{L^3} + B' \sigma^2 \sinh (\beta' \sigma^{2.5}) \qquad (2.18)$$

where L is the grain size, A', B' and β' are material parameters.

(d) Comparison of predicted and actual results

It is evident that the accuracy of the predicted results depends totally on the number of the assumptions involved together with the corresponding equations. This section is devoted to a summary of the line of approach together with a comparison of the predicted and actual results of different investigators.

Jovane (56) and Belk (66) derived an approximate analysis for the bulge forming of superplastic material by assuming that the bulge is spherical and the thickness remains uniform during forming. However, non-uniformity in sheet thickness is an important practical consideration and the experimental results showed that the difference between mean and actual thickness could be as high as 50%. Holt (59), on the other hand proposed a more detailed solution with particular emphasis on the resulting thickness profile, but another assumption still remained which was that the dome shape is spherical. With this assumption, he used an iterative method of solution, in

which the sheet was divided into ten annuli. During the deformation, the thickness of any annulus is assumed uniform. The profile was found by following the increase in width of the annuli with time. Since the edge of the annulus at the clamp is fixed, this would indicate the position of the other edge of that annulus, which in turn would locate the position of the next annulus and so on. It was shown that the deviation between the experimental and predicted results was not too great.

Cornfield and Johnson's analyses (64) are also based on an iterative solution. These investigators assumed that the hoop strain increased from zero at the clamp to a value equal to the tangential strain at the pole. The sheet was divided into concentric annuli and the change in the surface area was followed over the bulge from which the new radius of curvature and thickness distribution were found. However, in the analysis the way in which the hoop strain changes its value was not given, thus making it difficult to follow the steps taken in the computation. Comparison of theoretical and experimental results was shown to be reasonable.

The approach adopted by Tang and Robbins (65) was totally different from those mentioned above. In their analysis, they rely on the stress-strain rate relationship proposed by Avery and Backofen (24). They assumed that the bulge is spherical and the thickness of the shell is

linearly distributed. However, the results showed that the predicted rupture time for linearly distributed thickness deformation fits the experimental data for a limited range of experimental data only, and that a discrepancy occurs at the high strain rate region. The reasons were given as:

1. the shape of the shell is conical instead of spherical;
2. the thickness variation at very high strain rate may be nonlinear;
3. inaccuracy of experimental measurements in the high strain rate tests.

2.7 Concluding Remarks and Objectives

From the above brief review of the past literature on the bulge forming of superplastic materials, it can easily be observed that the studies on this particular type of process have hitherto been almost exclusively confined to predicting the behaviour of the bulge specimen through assumed or empirical strain rate hardening characteristics of the material as determined in the tension test, as well as through an assumed spherical shell and uniform thickness distribution. However, it would be useful to know whether the strain-rate sensitivity index (m) determined from a tensile test can be applied to the biaxial stress conditions which occur in bulge forming.

The basic assumptions in the uniaxial tension test used are the coaxiality and radiality of the strain paths. Only in axisymmetrical forming are the strain paths

coaxial in which the principal axes do not rotate with respect to the material. A strain path is said to be radial when the strain ratios $\varepsilon_t : \varepsilon_\theta : \varepsilon_s$ remain constant during deformation. In an axisymmetrical bulge test, the strain path at the pole of the shell is always radial having strain ratio $\varepsilon_t : \varepsilon_\theta : \varepsilon_s = -2:1:1$ (stress condition of $\sigma_t : \sigma_\theta : \sigma_s = 1 : 0 : 0$). When there is no draw-in of the flange, the strain ratio at the die edge is always $\varepsilon_t : \varepsilon_\theta : \varepsilon_s = -1 : 0 : 1$. However, every positoin between the pole and the die edge, the strain paths are not radial. Thus, a uniaxial test is equivalent to a balanced-biaxial tension test, and therefore is valid for a spherical bulge. In an actual case, however, the bulge cannot be a sphere (chapter 3) so that the stress-strain-rate relationship of a material in the uniaxial tension test can no longer be applicable to the unbalanced biaxial stretching case in the bulge test. The only condition where the uniaxial tension test result may be applicable to the bulge test is at the pole of the shell. Furthermore, the value of m defined as the slope of the logarithmic σ vs. $\dot{\varepsilon}$ curve, is assumed to be constant for a constant strain-rate. In chapter (8) it will be shown that the strain-rate during bulge forming is far from being constant. These considerations complicate a direct comparison between bulging and tensile m values.

The other assumptions concerning spherical shell and uniform wall thickness are also unrealistic, though mathematically convenient. The membrane stress, on these

assumptions, becomes uniform throughout the bulge profile for a pressure P, and therefore, the fracture must occur at the die edge, whereas in actual fact, fracture usually occurs in the vicinity of the pole. Moreover, if the shell is assumed to be spherical, then the ratio of the principal curvatures defined as $N = \frac{\rho_\theta}{\rho_s}$ should be equal to one. It will be shown in chapter(3)that the actual bulge can never be a surface of constant N value let alone a sphere of N = 1.

In the present study an attempt is made to measure the stresses, strain and strain-rates through the geometry of the bulge. Thus, the bulge test can be used to study the stress-strain and strain-rate relationship in the material under actual conditions in any sheet metal forming process.

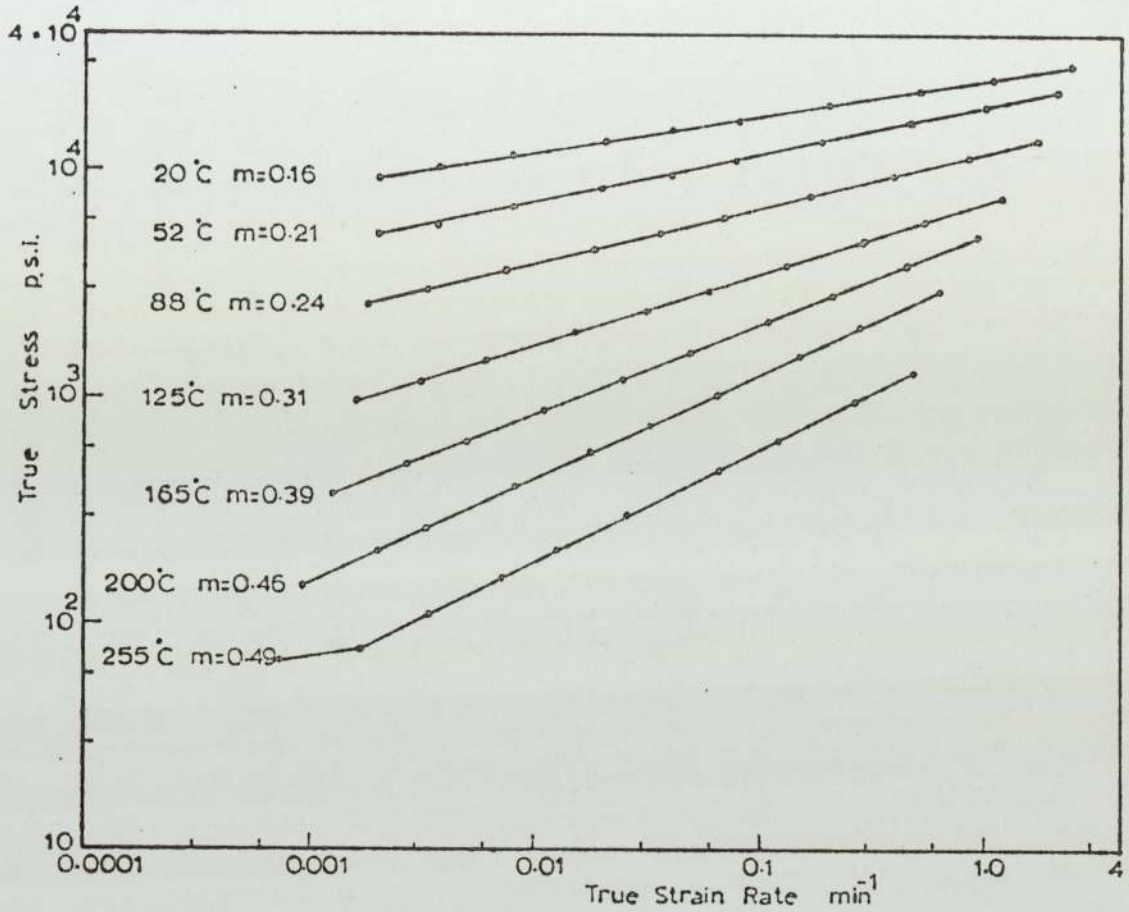

Fig. 2.1 – Log-Log plots of stress against strain-rate for eutectoid Zn-Al at various temperatures, after Nuttal, 79 .

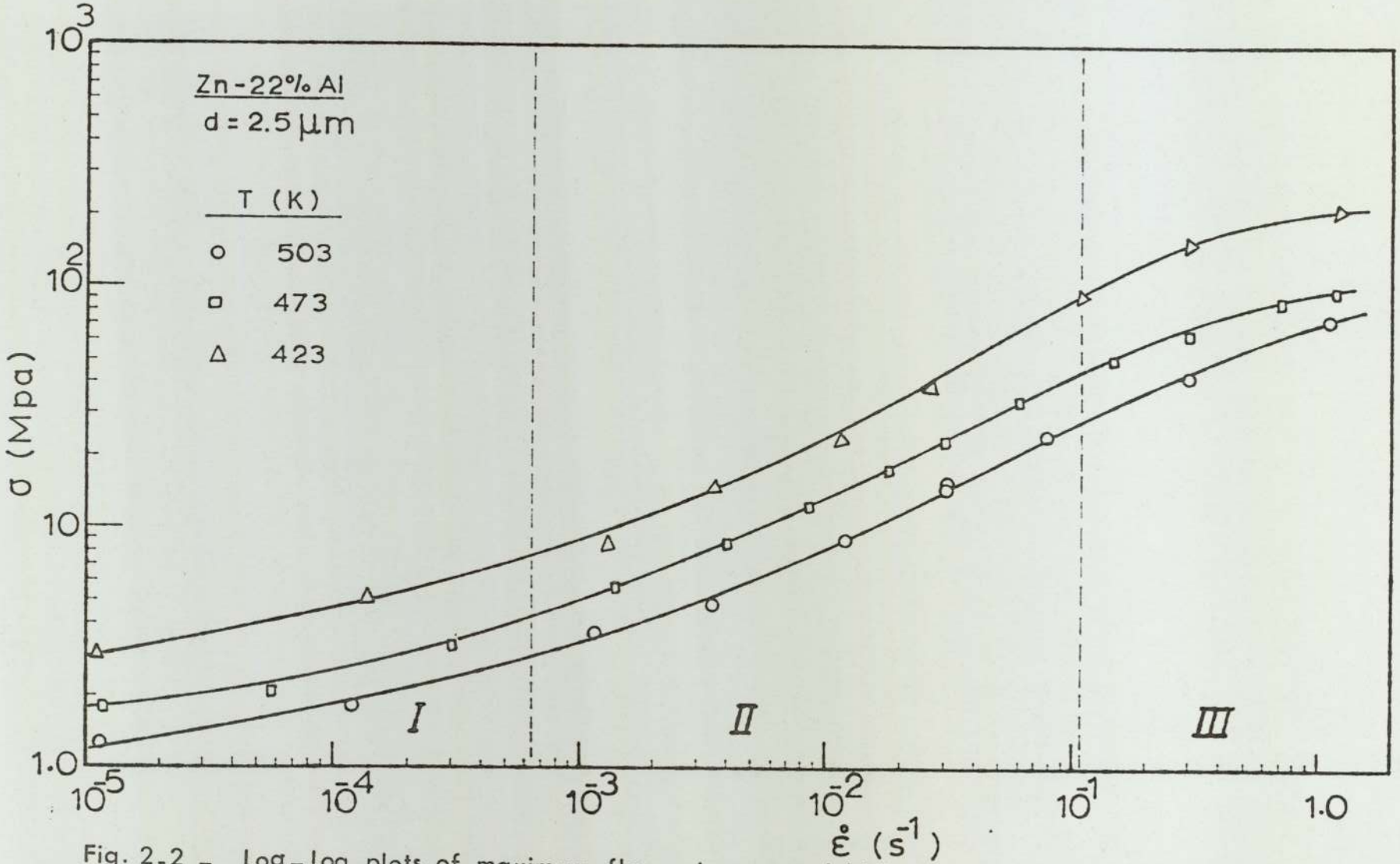

Fig. 2-2 - Log-Log plots of maximum flow stress vs. initial strain-rate for a eutectoid Zn-Al alloy, after F. A. Mohamed et al(55).

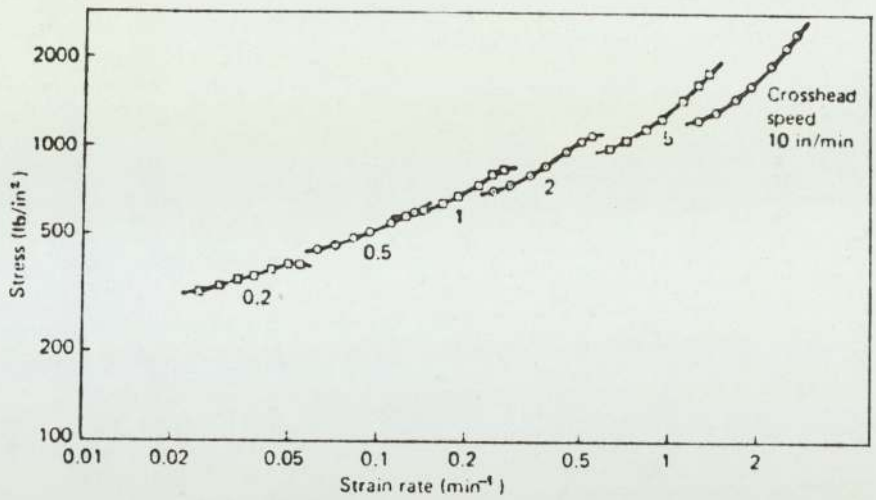

Fig. 2.3 _ Stress vs. strain-rate for Q. material at various constant cross-head speeds, after Fields & Hubert (80).

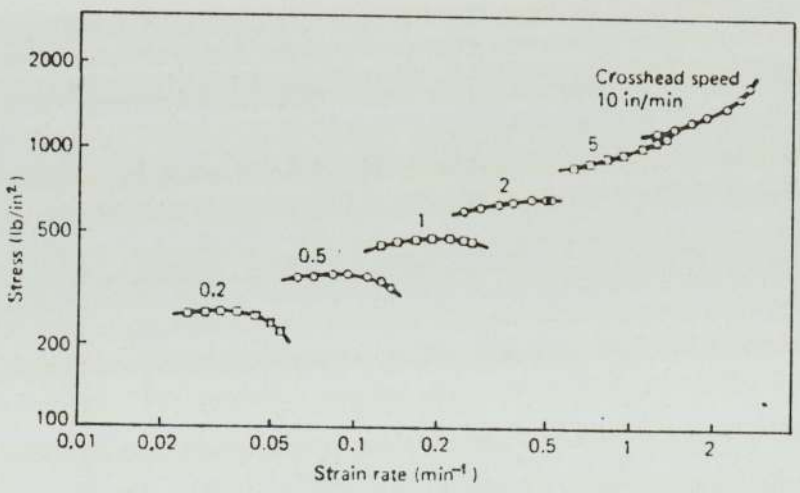

Fig. 2.4 _ Stress vs. strain-rate for Q.C.R. material at various constant cross-head speeds, after Fields & Hubert (80).

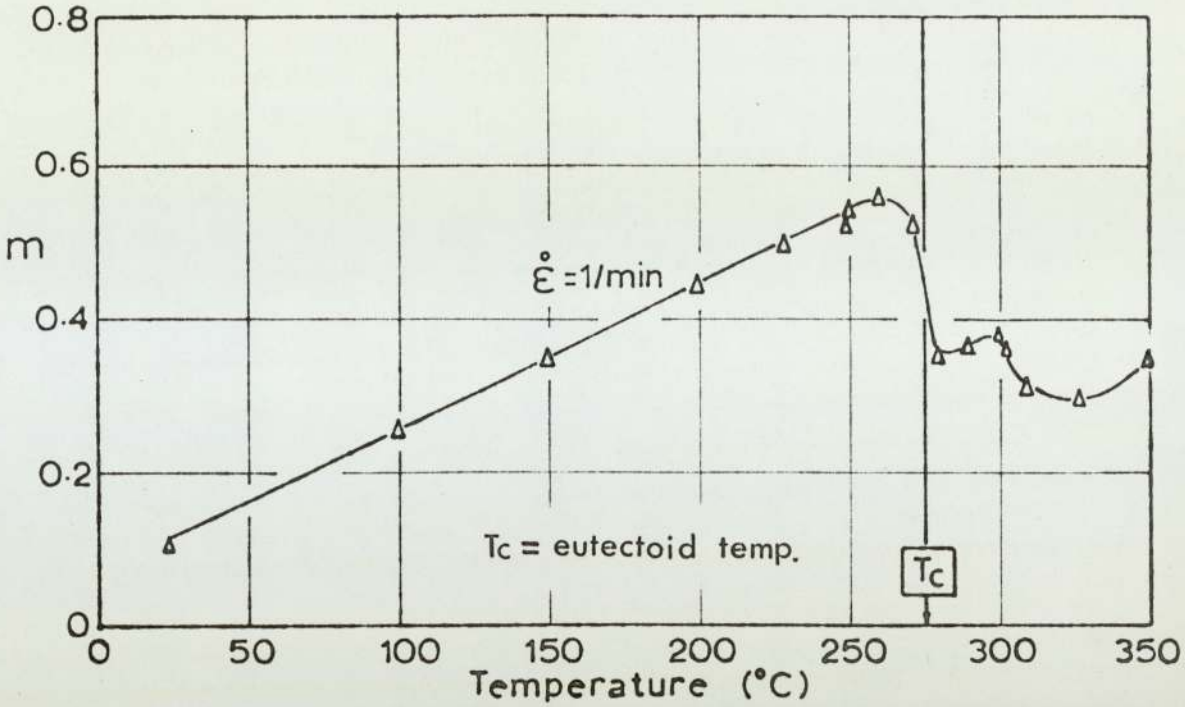

Fig. 2.5 – Temperature dependence of strain-rate sensitivity for quenched Al-80% Zn alloy, after Backofen et al (15).

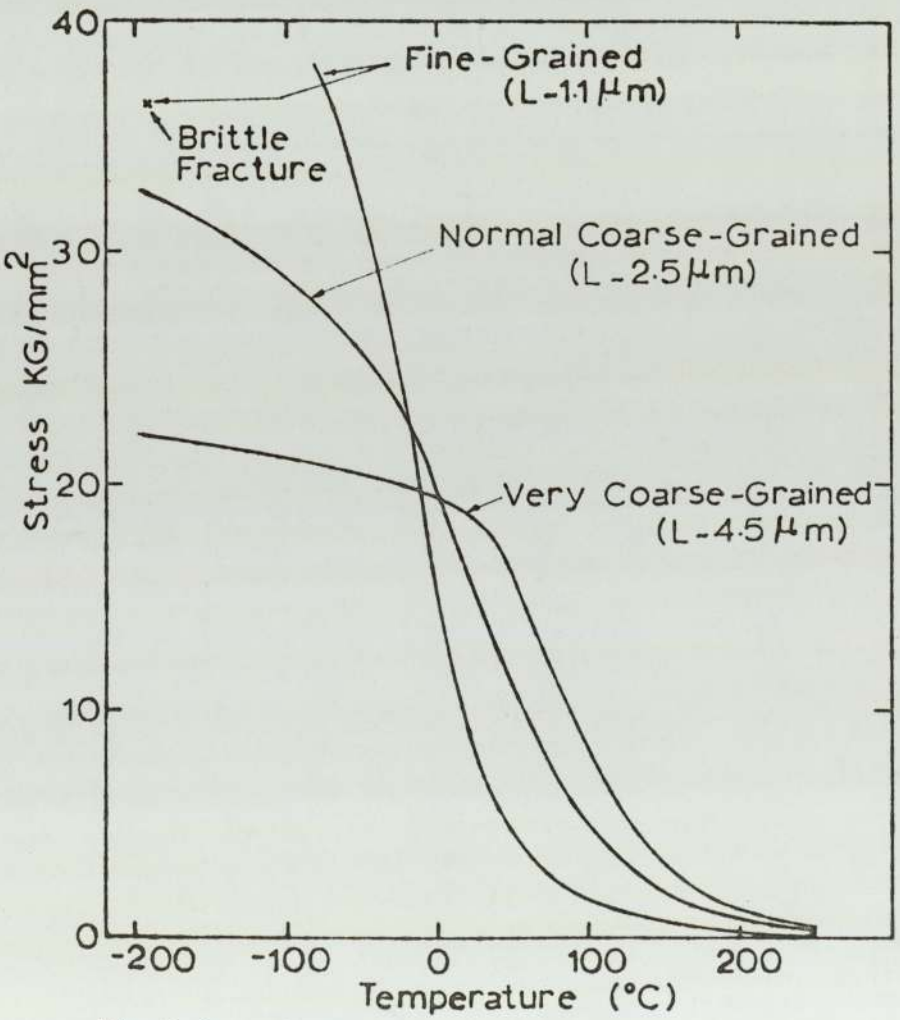

Fig. 2.6 – Stress vs. temperature at constant strain-rate for Zn-Al eutectoid alloy with various grain sizes, after Ball & Hutchinson (35).

PART A

THEORETICAL ANALYSIS OF THE BULGING PROCESS

CHAPTER 3

THE ANALYSIS OF THE BULGING PROCESS

Chapter 3

3.1 Introduction

Superplastic alloys in the form of sheet can be formed by pressure to produce useful components by techniques similar to those employed in the glass and plastics industries. Obviously, these forming operations involve free bulging, at one stage or another.

This chapter is devoted to the theoretical solution of the bulging deformation problem based on the following assumptions:

(i) the material is isotropic and incompressible;

(ii) the dome is a surface of revolution;

(iii) elastic strains are negligible;

(iv) the wall thickness is small compared with radii of curvatures and other dimensions of the bulge, hence, bending and shear stresses are ignored.

3.2 Relation between principal stresses and principal curvatures

In the shell of revolution shown in Fig. (3.1.a), the principal stresses may be determined by consideration of the equilibrium of the shell element cut out by two parallel circles whose planes are normal to the vertical axis of symmetry of the shell and two meridians (generators) of the shell. If the small stress in the through-thickness direction is ignored, then the shell element may be considered to be under biaxial stresses. The circumferential stress (σ_θ) and the meridianal stress (σ_s) thus appears as shown in Fig. (3.1.b). The radius of curvature

of the meridian (ρ_s) is defined by perpendiculars to the shell through points B and D of Fig. (3.1.b). Another radius of curvature (ρ_θ) is defined by perpendiculars to the shell through points A and B of Fig. (3.1.b). By geometry the centre of curvature corresponding to ρ_θ must lie on the axis of symmetry.

The component of the forces acting on the edges of the element normal to the shell element are

$2\ \sigma_\theta\ \rho_s\ d\phi\ t\ \sin(\frac{d\theta}{2})$ in the circumferential direction

and $2\ \sigma_s\ \rho_\theta\ d\theta\ t\ \sin(\frac{d\phi}{2})$ in the meridional direction.

The sum of these normal forces is in equilibrium with the normal pneumatic pressure (P) on the inside surface of the element, thus,

$$2\ \sigma_\theta\ \rho_s\ d\phi t \sin(\frac{d\theta}{2}) + 2\sigma_s \rho_\theta\ d\theta\, t \sin(\frac{d\phi}{2}) = P\rho_\theta\ d\theta\, \rho_s\ d\phi \qquad (3.1)$$

divide by $t\ \rho_\theta\ d\theta\ \rho_s\ d\phi$ and put

$$\sin(\frac{d\theta}{2}) \rightarrow \frac{d\theta}{2} \quad \text{and} \quad \sin(\frac{d\phi}{2}) \rightarrow \frac{d\phi}{2}$$

so that

$$\frac{\sigma_\theta}{\rho_\theta} + \frac{\sigma_s}{\rho_s} = \frac{P}{t} \qquad (3.2)$$

This fundamental equation applies to the axisymmetric deformation of all thin shells of revolution, and it determines the stresses for a particular geometrical configuration of the work piece. At any particular stage of the bulge test and at any point of the shell, these biaxial stresses are, in fact, the flow stresses of the

material at that point. As deformation progresses, the pressure (P) produces incremental stresses throughout the shell and these incremental stresses give rise to incremental strains according to the strain rate sensitivity of the test material. The change in the shape of the bulge is, of course, closely related to these incremental strains. In Eq. (3.2) the meridional tangential stress (σ_s) is always tensile, but the circumferential stress (σ_θ) can be compressive near the rim of the bulge, and it is assumed that both these stresses are uniformly distributed through the thickness. Obviously, the biaxial stretching of the work material involves progressive thinning, which increases from the edge towards the pole due to the clamping effects.

Considering a cap of radius r shown in Fig. (3.2) it can be concluded that the equilibrium of the shell under vertical forces is

$$\sigma_s = \frac{Pr}{2t \sin\theta} \qquad (3.3)$$

also by geometry

$$\rho_\theta = \frac{r}{\sin\theta} \qquad (3.4)$$

hence

$$\sigma_s = \frac{P\rho_\theta}{2t} \qquad (3.5)$$

Combining Eqs. (3.2) and (3.5), we get

$$\sigma_\theta = \frac{P}{t}\rho_\theta - \frac{\rho_\theta}{\rho_s}\sigma_s$$

$$= \sigma_s \left(2 - \frac{\rho_\theta}{\rho_s}\right) \qquad (3.6)$$

The ratio of the local principal curvatures ($\frac{\rho_\theta}{\rho_s}$) is of fundamental importance, since it determines the ratio of the principal stresses at anywhere along the bulge profile. We shall call this ratio N,

$$N = \frac{\rho_\theta}{\rho_s} \qquad (3.7)$$

substituting in Eq. (3.6), we get

$$N = 2 - \frac{\sigma_\theta}{\sigma_s} \qquad (3.8)$$

The equations governing the deformation in the thin shells can now be traced.

3.2.1 Surface of constant N-values

Two cases of stresses in thin shells of revolution with constant N value are usually considered in elementary strength of materials. These are for N = 0 (cylinder), where the hoop stress (σ_θ) is twice the longitudinal stress (σ_s), and for N = 1 (sphere), where the two membrane stresses are equal. As can be seen from Eq. (3.8), in a surface for which N = 2, the hoop stress (σ_θ) disappears. Such surfaces have been used in the design of pressure vessels, like the ends of boiler drums. There are, of course, infinitely many surfaces of revolution with constant N values. T.C. Hsü et al (70) have constructed some of these surfaces by expressing the meridian sections in parametric equations as follows:

$$\rho_s = \frac{1}{\cos\theta} \frac{dr}{d\theta} \qquad (3.9)$$

Combining Eqs. (3.4) and (3.9)

$$N = \frac{\rho_\theta}{\rho_s} = \frac{r \cos\theta}{\sin\theta \frac{dr}{d\theta}} \qquad (3.10)$$

and

therefore $$N \frac{dr}{r} = \frac{d(\sin\theta)}{\sin\theta} \qquad (3.11)$$

When N is constant, equation (3.11) can be integrated as

$$r^N = A \sin\theta \qquad (3.12)$$

where A is the constant of integration. For exploring the shapes of these surfaces, it is convenient to assume

$$(r)_{\theta=\pi/2} = 1 \qquad (3.13)$$

So that Eq. (3.12) takes the following simpler form

$$\sin\theta = r^N \qquad (3.14)$$

The curves relating r and $\sin\theta$ for constant N values given by Eq. (3.14) are non-linear and they can be linearised by the use of (log - log) scales so that the curves become radial lines emerging from the origin, each having a shape of N. See Fig. (3.3).

For the other coordinate, l, combination of Eq. (3.4) and (3.14) and definition of N gives

$$\rho_s = \frac{(\sin\theta)^{\frac{1-N}{N}}}{N} \qquad (3.15)$$

However, $$dl = -\rho_s \sin\theta \, d\theta \qquad (3.16)$$

the negative sign is due to the increase in l with decrease

in θ, hence,

$$1 = -\frac{1}{N}\int_{\pi/2}^{\theta} (\sin\theta)^{1/N}\, d\theta \qquad (3.17)$$

Eq. (3.17) cannot be expressed in terms of elementary functions except for values of N equal to zero, ± 1 and reciprocal of integers; but it can be easily evaluated by graphical or mechanical means. These meridian sections are shown in Fig. (3.4). This figure shows that only when N is positive, the surfaces are closed, otherwise they are bollard-shaped and open at the top and the bottom. As positive N increases indefinitely the surface becomes like the outside surface of flatter and flatter pancakes; and as N approaches negative infinity, the surface becomes like two flat sheets of paper each with a hole and the two sheets are joined at the edges of the holes.

The variation of the radius of curvature in the circumferential direction (ρ_θ) for constant N values can be explored by elimination of θ from Eq. (3.4) and (3.14), hence,

$$\rho_\theta = r^{(1-N)} \qquad (3.18)$$

These variations are shown in Fig. (3.5). The variations of the radius of curvature in the meridian direction (ρ_s) follows the same pattern as Fig. (3.5), but in different scales, of course. The line for constant ρ_θ, (N = 1) is self-explanatory; but the linear variation for N = 0 requires some elucidation. When N = 0 the surface may

either be a cone or a cylinder. When it is a cylinder, only the point $(\rho_\theta)_{r=1} = 1$ is operative; and when it is a cone, ρ_θ is, of course, proportional to r. For surfaces of constant N-value, at the pole (r = 0), the stress and the radius of curvature, is either zero (N < 1), or infinity (N > 1), except for the sphere (N = 1). When N is less than unity, the meridional tangential tension rises gradually or rapidly towards $\frac{P}{2t}$ as the equator is approached, and when N is greater than unity, this tension starts at $\frac{P}{2t}$ at the equator and rises gradually or rapidly towards infinity as the pole is approached.

In surfaces of constant N value, the circumferential stress is, of course, proportional to the meridional one, hence, Fig. (3.5) also represents the variations of the circumferential stress. The ratio between the meridional tangential and the circumferential stress is not, however, simply N, but is related to N as in Eq. (3.8). For exploring the variation of the circumferential, or hoop stress, it is desirable to divide the N values into four ranges, as in table (3.1)

Ranges	$N = \frac{\rho_\theta}{\rho_s}$	Shape of Surfaces	σ_θ/σ_s
1	>2	pancake shaped	< 0 (σ_θ compressive)
	=2	tangerine shaped	$\sigma_\theta = 0$ (uniaxial tension test)
2	$1 < N < 2$	oblate spheroid	$0 < \frac{\sigma\theta}{\sigma_s} < 1$ (tensile σ_θ less than σ_s)
	=1	sphere	$\sigma_\theta = \sigma_s$ (balanced biaxial stretch)
3	$0 < N < 1$	prolate spheroid	$1 < \frac{\sigma_\theta}{\sigma_s} < 2$
	=0	cone or cylinder	$\sigma_\theta = 2\sigma_s$
4	< o	bollard-shaped	$\sigma_\theta > 2\sigma_s$

Table (3.1) - Summary of surfaces of constant N values

3.2.2 Prolateness of the real-shell

Any real specimen of sheet material formed by hydrostatic pressure can never be a surface of constant N value, owing to the constraints on the deformations in the material. Thus, at the pole the strains and stresses are, by symmetry, balanced biaxial stretching and there N must be equal to unity; but at the edge of the bulge, the circumferential strain is either zero, or slightly compressive (if there is draw-in), hence the meridional tangential stress must be at least twice the circumferen-

tial stress, and the N value must therefore, be greater than one but smaller than two.

In most of the papers on the bulge test, the workpiece has been assumed to be a spherical surface in the predictive or interpretative theories, (56), (59), (64 - 66), (68). It has just been shown that a real specimen cannot be any surface of constant N value, let alone a sphere, the simplest of constant N surfaces. Even just for describing an actual bulged specimen, therefore, it is necessary first to define accurately the characteristics of an actual surface from point to point. Also, stresses are related to curvatures, not directly to the l and r coordinates. Hence, a bulge may be nearly a sphere, but its stresses very different from those in a sphere.

At any point in a continuous surface of revolution, there is an N value, which applies to a vanishingly narrow ribbon of surface at the same latitude. If this (positive) value of N is less than one, then the surface at that latitude may be said to be more pointed than a sphere (prolate); and, if it is greater than one, to be more flattened than a sphere (or oblate), because, if a surface of that constant N value is constructed to pass through that point, that surface will be prolate or oblate, respectively, as compared with a perfect sphere. In fact, $(1 - N)$ may be defined as prolateness, $\bar{P}$, and the negative of prolateness, when $N > 1$, is oblateness. Prolateness and curvatures are two distinct concepts, and a surface can

have either large curvature and large prolateness, or small curvature and large prolateness. As the bulging action progresses, the curvature generally increases, but, in theory, the prolateness does not necessarily decrease. As has been shown, a sheet metal bulged specimen is always spherical (zero prolateness) at the pole, and theoretically, it is oblate at the edge, because, if there are no bending (only membrane stresses present) and no draw-in, then the circumferential strain disappears at the edge, and both the stress ratio $\frac{\sigma_\theta}{\sigma_s}$ and the prolateness $(1 - N)$ are equal to $\frac{1}{2}$ there; though in practice, there are, in metal shells being formed, always bending and friction at the rim so that the theoretical ratios of the curvatures and stresses are obscured. Between the pole and the rim, the surface may be prolate, spherical or oblate, as the plastic properties of the work material dictate. Indeed, they are all three, as will be shown in chapter 6.

3.3 Relation Between Strains and Shape of the Bulge

The bulged specimen is illustrated in Fig. (3.2) in the cylindrical coordinate axes OL and OR. In such an axisymmetrical case, the geometrical transformation is completely determined by the two parametric equations as follows:

$$\begin{aligned} l &= l(r_o\ ,\ T) \\ r &= r(r_o\ ,\ T) \end{aligned} \qquad (3.19)$$

where l and r are the current longitudinal and radial coordinates, respectively, and r_o and T are the initial radial distance and time, respectively. The elimination of the parameter r_o for a particular value of T in Eq. (3.19) yields a relationship between l and r which represents a meridian contour of the partly formed shell; and the elimination of the parameter T for a particular value of r_o yields the path of a particle in the work-piece.

In order to derive the mechanical behaviour of the work material from the bulge test, it is necessary to determine the strains from the basic equation in Eq. (3.19). By symmetry, the principal strains are the meridional tangential (ε_s), the circumferential (ε_θ) and the through thickness (ε_t) strains and they are by definition,

$$\varepsilon_s = \log_e \left(\frac{ds}{dr_o}\right) \qquad (3.20)$$

$$\varepsilon_\theta = \log_e \left(\frac{r}{r_o}\right) \qquad (3.21)$$

$$\varepsilon_t = \log_e \left(\frac{t}{t_o}\right) \qquad (3.22)$$

where s is the arc length of the meridian section in Fig. (3.2), t and t_o are the current and original through thickness, respectively. In experimental investigations, however, the principal strains are determined by marking suitable grids onto the face of the specimen and measuring their geometrical transformations.

As the material is assumed to be incompressible,

therefore, three principal (natural) strains add up to zero, Eq. (2.11). With triaxial strains having only two degrees of freedom, any two of them are sufficient to define the state of strain of the material particle concerned under a given applied stress condition.

Investigators have unanimously measured the circumferential strains because they can be obtained easily and accurately with a travelling microscope. For the remaining two strains, there is an alternative choice. Some workers prefer through-thickness strains because they can be read directly from a dial gauge installed on a rig with a fixed anvil at the base and with the specimen placed between the fixed and the measuring anvils of the dial gauge. It is evident that this Method requires the anvils to be normal to the specimen. Some investigators, however, have measured the meridional tangential strain (ε_s) instead. There are two different methods of measuring ε_s. The first method involves arc length measurement of the deformed bulge, Eq. (3.20), by a tape provided with squares identical to those on the undeformed grid. The second method is modification of ε_s Term in Eq. (3.20).

Suppose θ is the angle of inclination of the meridian section with the OR axis, Fig. (3.2), then

$$\sec \theta = \frac{ds}{dr} \qquad (3.23)$$

so that ε_s in Eq. (3.20) becomes

$$\varepsilon_s = \log_e \left(\frac{dr}{dr_o} \frac{1}{\cos\theta}\right) \qquad (3.24)$$

The angle θ can be measured easily with a workshop protractor.

3.4 Principal Strain Rates in Terms of Rate of Change of r and l

It was explained in the previous chapter that superplastic materials exhibit an unusually high level of strain-rate hardening; and in the bulge test the change of shape for subsequent deformation is closely related to the principal strain rates.

Since the geometrical transformation of the specimen is completely determined by the parameters r and l for any stage of deformation, Eq. (3.19), the principal strain-rates can sufficiently be defined by the rate of change of r and l. The rate of any variable can be expressed in terms of time (T), and this is usually shown by a dot above the parameter considered.

The principal strain rates can easily be derived through the definition of principal strains, Eqs. (3.20) - (3.22),

$$\dot{\varepsilon}_\theta = \frac{\partial \varepsilon_\theta}{\partial T} = \frac{\partial}{\partial T} \left(\log_e \frac{r}{r_o}\right) = \frac{\dot{r}}{r} \qquad (3.25)$$

$$\dot{\varepsilon}_t = \frac{\partial \varepsilon_t}{\partial T} = \frac{\partial}{\partial T} \left(\log_e \frac{t}{t_o}\right) = \frac{\dot{t}}{t} \qquad (3.26)$$

$$\dot{\varepsilon}_s = \frac{\partial \varepsilon_s}{\partial T} = \frac{\partial}{\partial T} \left(\log_e \frac{ds}{dr_o} \right)$$

$$= \frac{\partial}{\partial T} \log_e \left(\frac{dr}{dr_o} \sqrt{1 + \left(\frac{dr}{dl} \right)^2} \right) \qquad (3.27)$$

The three principal strain rates also should add up to zero (incompressibility condition), hence,

$$\dot{\varepsilon}_\theta + \dot{\varepsilon}_t + \dot{\varepsilon}_s = 0 \qquad (3.28)$$

3.5 Principal Strain Rates in Terms of Rate of Change of r, l, and θ

It is frequently more convenient to express the principal strain rates in terms of the bulge profile inclination (θ) as a variable, specially for $\dot{\varepsilon}_s$. The variable θ is in fact related to r and l by the function

$$\theta = \tan^{-1} \left(\frac{dl}{dr} \right) \qquad (3.29)$$

Thus, the meridional tangential strain rate in Eq. (3.27) can be obtained by differentiating Eq. (3.24) with respect to T,

$$\dot{\varepsilon}_s = \frac{\partial}{\partial T} \left(\log_e \left(\frac{dr}{dr_o} \frac{1}{\cos\theta} \right) \right)$$

$$= \frac{\dot{dr}}{dr} + \dot{\theta} \tan \theta \qquad (3.30)$$

The rate of change of current radius in the bulge test can be expressed by the time rates of circumferential curvature and profile inclination so that

$$\dot{r} = \frac{\partial}{\partial T} (\rho_\theta \sin\theta)$$

$$= \dot{\rho}_\theta \sin\theta + \rho_\theta \dot{\theta} \cos\theta \qquad (3.31)$$

The circumferential strain rate then becomes,

$$\dot{\varepsilon}_\theta = \frac{\dot{r}}{r} = \frac{\dot{\rho}_\theta}{\rho_\theta} + \dot{\theta} \cot\theta \qquad (3.32)$$

and the corresponding through-thickness strain-rate can be calculated through the incompressibility equation, Eq. (3.28).

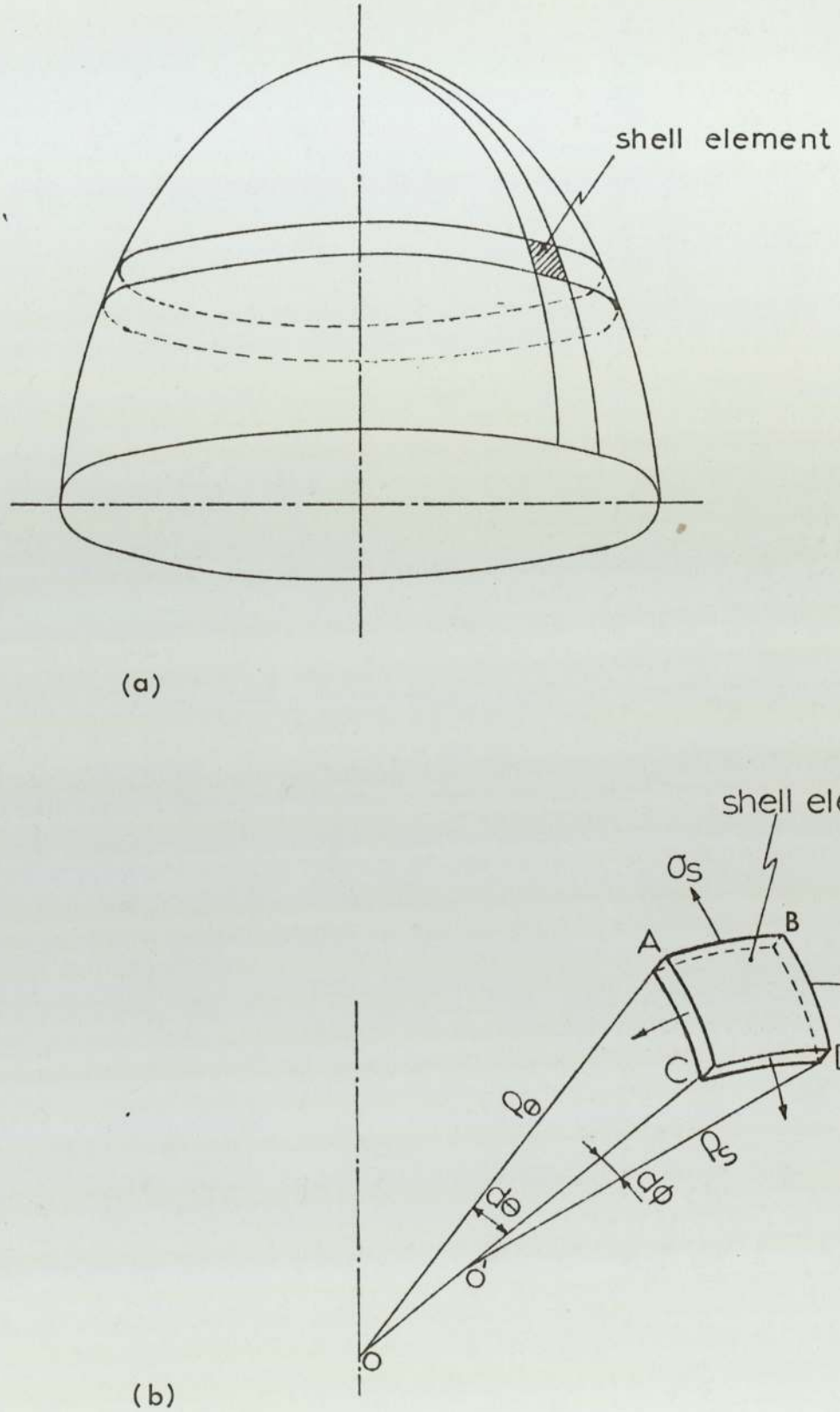

Fig. 3-1 – Thin shell of revolution subjected to internal pressure.

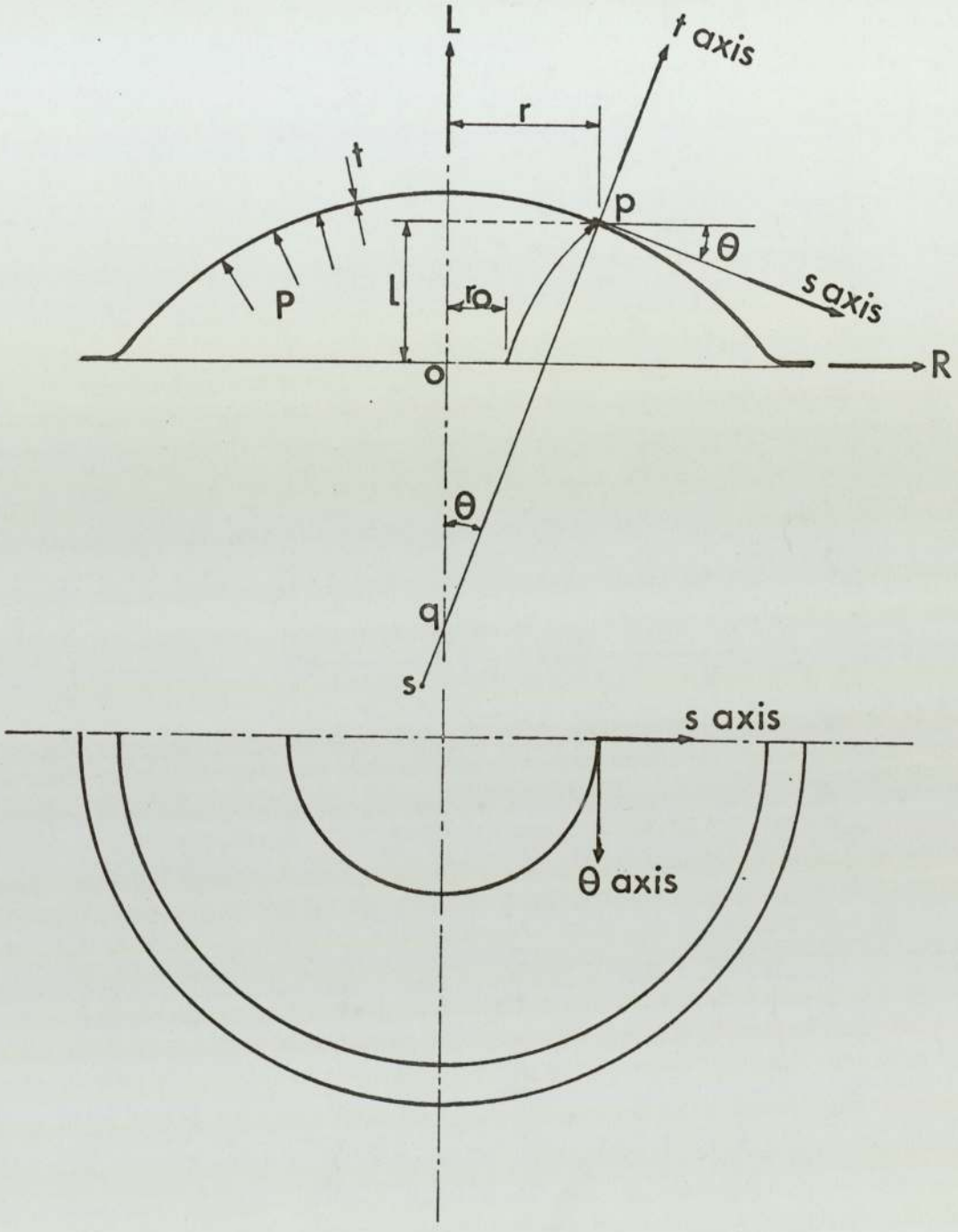

Fig. 3-2 - An axisymmetrical deformed bulge.

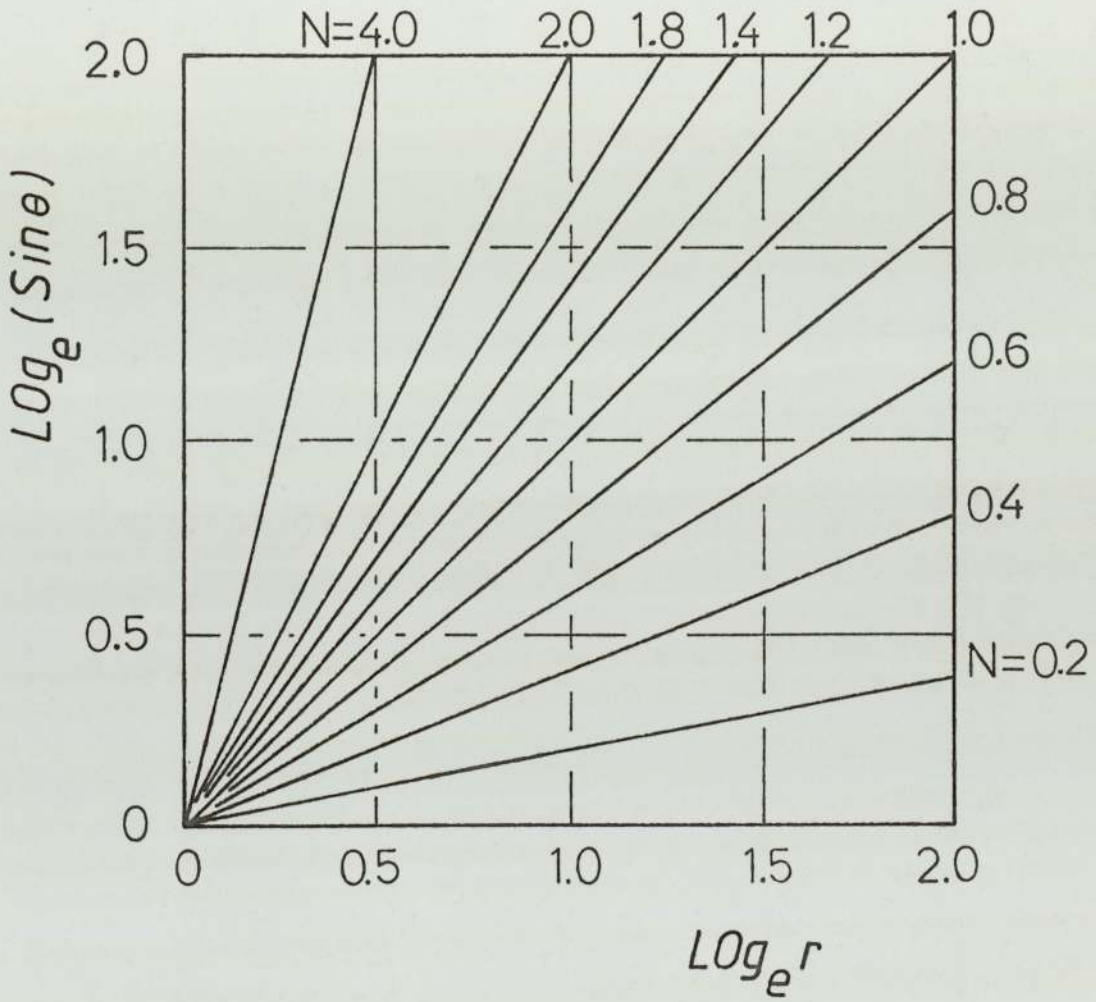

Fig. 3-3- Log-Log plots of profile slope vs. radial distance for constant N surfaces in the circumferential direction, after Hsü et al (70).

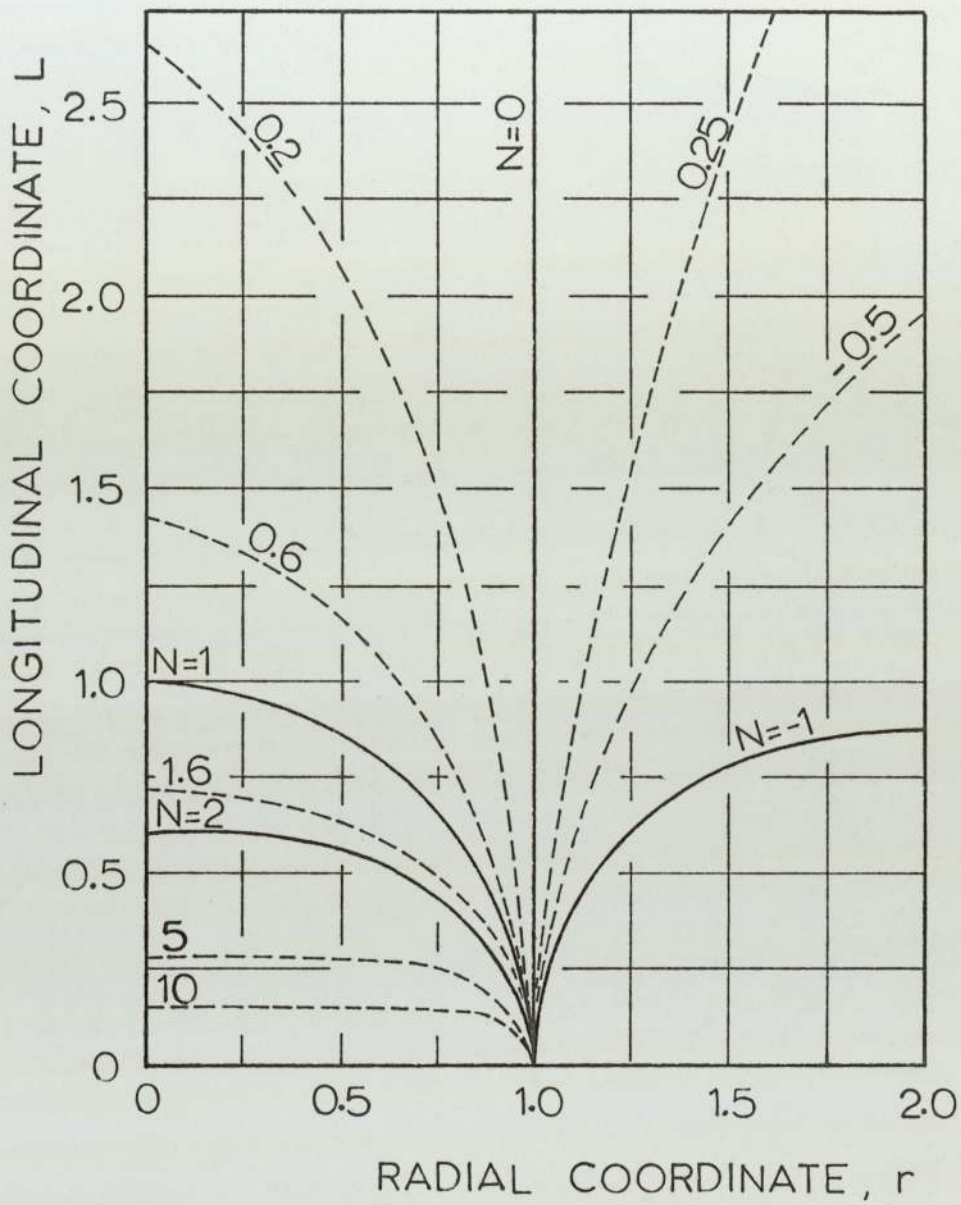

Fig. 3.4– Meridian sections of surfaces of constant N values, after T.C. Hsü et al (70).

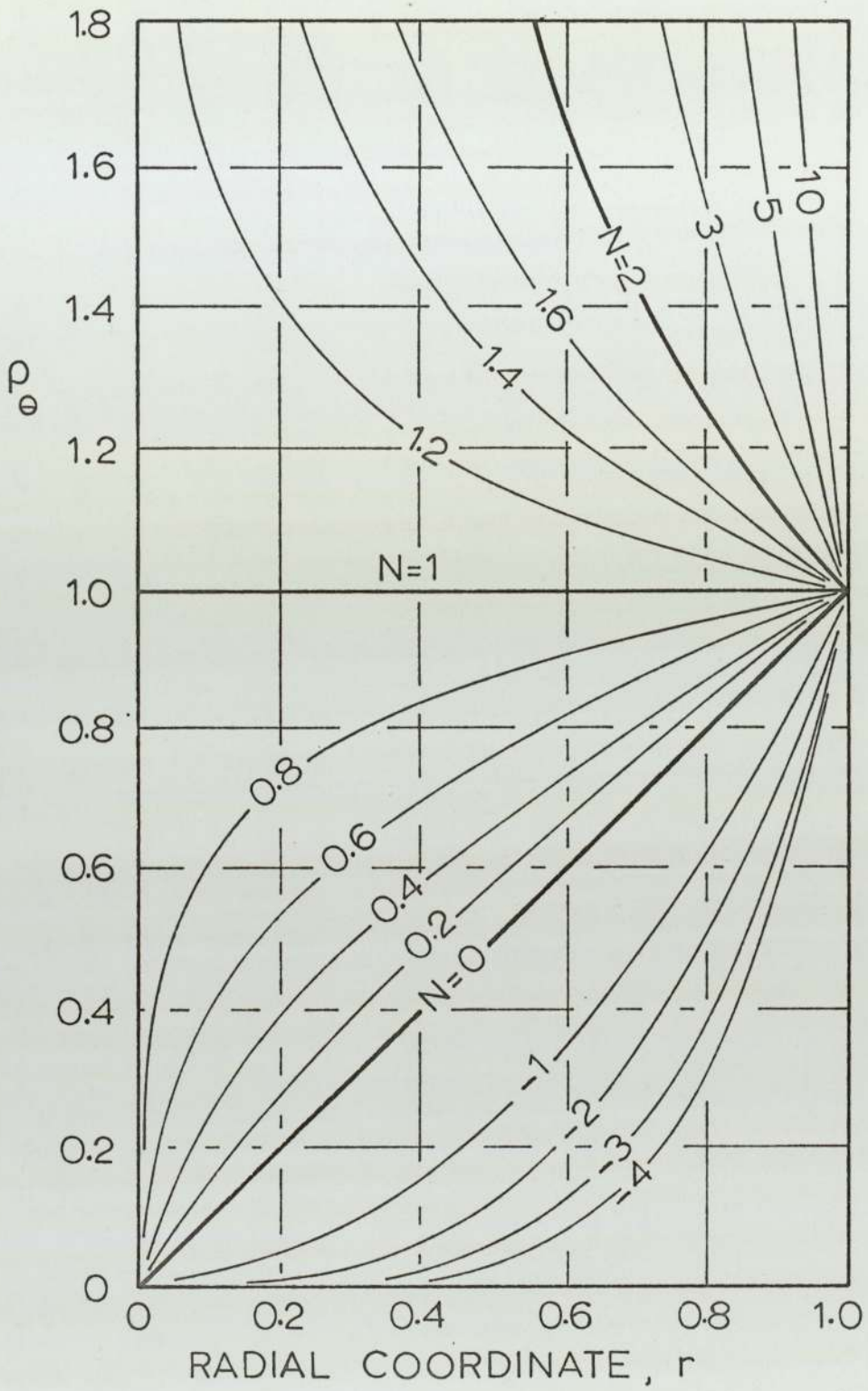

Fig. 3-5 – Variations of ρ_θ with r for surfaces of constant N values, after Hsü et al (70).

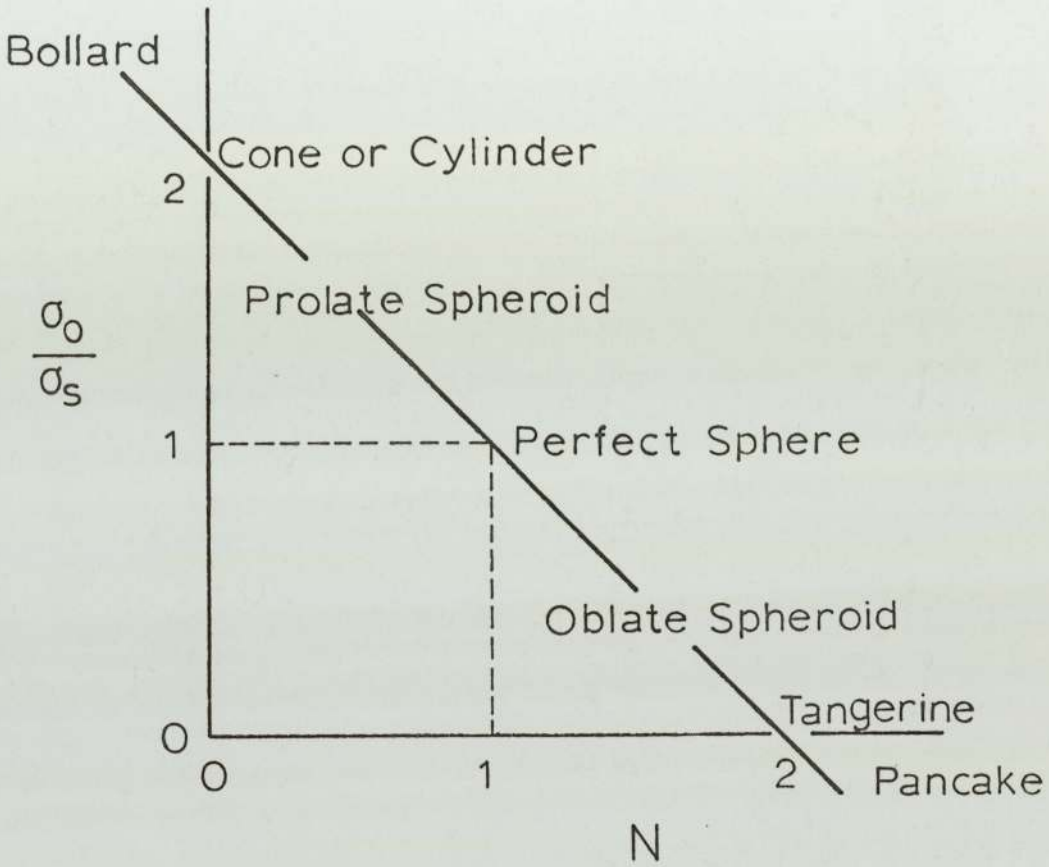

Fig. 3-6 – Variation of the stress ratio with N value .

CHAPTER 4

GRAPHICAL REPRESENTATION OF MECHANICAL BEHAVIOUR OF SHEET MATERIALS DURING DEFORMATION

Chapter 4

4.1 Introduction

Metal forming processes are always three-dimensional, even in the tension or the compression test. Although only the stress and the strain in the loading direction are normally considered significant, the deformation is still three-dimensional. In such a process, the stress and the strain in the loading direction are determined and plotted against each other in the stress-strain curve which is usually considered to represent the mechanical behaviour of the material.

Sheet metal forming processes are more complex than those of uniaxial tension or compression test, and in such a complex deformation, states of stress rather than single stress and states of strain rather than single strain are involved, and, when measured, they can no longer be plotted against each other in a single curve.

Many investigators have used the generalised stresses and strains in order to show the mechanical behaviour of metals by a single curve. This generalised stress-strain relationship is expressed as:-

$$\bar{\sigma} = F(\bar{\varepsilon}) \qquad (4.1)$$

where $$\bar{\sigma} = \sqrt{\frac{1}{2}} \left[(\sigma_1 - \sigma_2)^2 + (\sigma_2 - \sigma_3)^2 + (\sigma_3 - \sigma_1)^2 \right]^{\frac{1}{2}} \qquad (4.2)$$

and $$\bar{\varepsilon} = \sqrt{\frac{2}{9}} \left[(\varepsilon_1 - \varepsilon_2)^2 + (\varepsilon_2 - \varepsilon_3)^2 + (\varepsilon_3 - \varepsilon_1)^2 \right]^{\frac{1}{2}} \qquad (4.3)$$

In Eq. (4.1), the basic assumptions are the coaxiality and radiality of the strain paths. In sheet metal forming, neither of the two assumptions for the generalised stress-strain relationship is true. Therefore, this relationship is only an approximation. In an axisymmetrical bulge test, the strain path at the pole of the shell is always radial having a strain ratio $\varepsilon_t : \varepsilon_\theta : \varepsilon_s = -2 : 1 : 1$. When there is no draw-in of the flange, the strain ratio at the die edge is always $\varepsilon_t : \varepsilon_\theta : \varepsilon_s = -1 : 0 : 1$. However, everywhere between the pole and die edge, the strain paths are not radial. Thus, the stress-strain relationship in the bulge test must be of the form:

$$\bar{\sigma} = F\left(\int d\bar{\varepsilon}\right) \qquad (4.4)$$

where $\int d\bar{\varepsilon}$ represents the length of the strain path.

In this thesis, a totally different type of graphical method is used to represent the states of stress, strain and strain rate in axisymmetrical forming. This particular co-ordinate system is called the triangular coordinate system, and has been proposed independently by Marciniak (71) and Hsü (72), (73). Hsü has extensively applied this system to sheet metal forming processes (74) - (77) and details are available in the appropriate references. Therefore, only the fundamentals will be discussed in this section.

4.2 Triangular Co-ordinate System for Strains

The triangular co-ordinates for strain are based on the fact that the metals are incompressible, and, the sum of three principal (natural) strains is zero, if the elastic strains, which are comparatively very small in metal forming problems, are ignored.

In the triangular co-ordinate system shown in Fig. (4.1), the origin represents the undeformed state. Three axes spaced 120° to one another in a plane are the co-ordinate axes for the three principal strains. Every point in this co-ordinate system represents a state of strain with a set of values for the three principal strains. For instance, a typical point p (Fig. 4.1) such that the line OP makes an angle α with the ε_I axis represents a state of strain with

$$\begin{aligned} \varepsilon_I &= \overline{OP} \cos\alpha \\ \varepsilon_{II} &= \overline{OP} \cos\left(\frac{4\pi}{3} - \alpha\right) \\ \varepsilon_{III} &= \overline{OP} \cos\left(\frac{2\pi}{3} - \alpha\right) \end{aligned} \qquad (4.5)$$

and $$\varepsilon_I + \varepsilon_{II} + \varepsilon_{III} = \overline{OP}\left[\cos\alpha + \cos\left(\frac{4\pi}{3} - \alpha\right) + \cos\left(\frac{2\pi}{3} - \alpha\right)\right] = 0 \qquad (4.6)$$

which satisfies the condition of incompressibility of metals.

Assignment of each axis to a particular strain is arbitrary so that it becomes advantageous to adopt a standard choice of coordinates. Of the six different ways

of assigning them, HSÜ (72), (73) suggests the vertical axis to denote the through-thickness strain since sheet metal engineers are often interested in the thickness of materials during deformation; and psychologically, the vertical axis is the most prominent of the three. In most axisymmetrical sheet metal forming, the meridional tangential strain is always tensile whilst the circumferential strain falls on both the positive and negative region of the ε_θ axis depending on the condition of draw-in of the flange. Thus, in order to suit right-handed people by having most of the strain paths falling on the right hand side of the ε_t axis, HSÜ further suggests the ε_θ and ε_s axes to be on the left and right hand side of ε_t axis respectively. The choice of the coordinate axis in this thesis will follow that proposed by HSÜ and is shown in Fig. (4.2).

Using the sign conventions shown in Fig. (4.2), it is obvious that the points on the three axes, together with their backward extensions, represent state of strain given by

$$\varepsilon_i = \varepsilon_j = -\frac{\varepsilon_k}{2} \quad (i, j, k = t, \theta, s) \quad (4.7)$$

These are the states of strain involved in both uniaxial tension and compression tests for isotropic materials. Thus, the strain paths for uniaxial tension tests will follow the positive axes and those for compression tests

will follow the negative axes. By introducing 6 more lines through the origin and perpendicular to the axes, these lines then represent pure shears whose states of strain are given by

$$\varepsilon_i = -\varepsilon_j \quad , \quad \varepsilon_k = 0 \quad (i,j,k = t, \theta, s) \quad (4.8)$$

By numbering these 12 lines from 0 to 12 clockwise, like the face of a clock, each number has a specific physical meaning, and is called the characteristic index for strain (η). As can be seen in Eq. (4.5), the ratios between the principal strains are dependent on the angle α through the equation

$$\eta = \frac{6}{\pi}\alpha \qquad (4.9)$$

Thus, odd numbers are for pure shear and the even numbers for cylindrical strains. With the co-ordinate axes for ε_s, ε_θ and ε_t chosen as shown in Fig. (4.2), the zones of thickening and thinning, circumferential expansion and contraction, and tangential stretching and compression are clearly divided. All the typical modes of deformation are shown in Fig. (4.3). It has been shown (74) that under the usual axisymmetrical sheet metal forming processes, the strain paths fall between 2 to 8 o'clock, and processes corresponding to strain paths beyond this range, though possible, rarely exist. In the bulge test, however, geometrical and mechanical constraints require that the state of strain

at the pole of the bulge is along 6 o'clock where balanced biaxial stretching occurs. The state of strain at the die edge, for the case of draw-in, is along 5 o'clock.

A strain path of constant ratio is called a radial (or proportional) strain path. This particular type of strain path occurs at the pole of the bulge for obvious reasons. If the material particles in the work-piece is designated by a single parameter (r_o), the distance from the centre in the blank, then for every constant value of r_o, the state of strain varies for every stage of deformation. Therefore, the strain paths plotted in the triangular co-ordinate system become curved and they are known as curved strain paths.

In sheet metal forming processes, it is obvious that the strain paths plotted on the triangular co-ordinate system do not fall exactly along the 12 lines representing typical modes of deformation; that is the values of η are not integers. In this case the deformation is neither a pure tension or compression nor a pure shear but is something in between. Since any point in the co-ordinate system shows a state of strain, it is possible to perform vector addition and resolution on the triangular co-ordinate diagram into a combination of plane strains; or cylindrical strains; or a cylindrical and a plane strain depending on the convenience at the time of analysis.

The magnitude of any position vector in the triangular co-ordinate system can be found from the following analysis. In Fig. (4.4), let vector $\underset{\sim}{OP}$ be resolved into two perpendicular components along $\eta = 12$ and $\eta = 3$, then

$$x = \varepsilon_t$$

$$y = \frac{\varepsilon_s}{\cos 30^\circ} + \frac{\varepsilon_t}{\tan 60^\circ}$$

$$= \sqrt{\frac{1}{3}} (2\varepsilon_s + \varepsilon_t)$$

then, $$|\underset{\sim}{OP}|^2 = x^2 + y^2 = \varepsilon_t^2 + 1/3 \ (2\varepsilon_s + \varepsilon_t)^2 \qquad (4.10)$$

Using the incompressibility equation, Eq. (2.11), Eq. (4.10) becomes

$$3 |\underset{\sim}{OP}|^2 = 2\varepsilon_t^2 + 2\varepsilon_s^2 + 4\varepsilon_s\varepsilon_t + 2(-\varepsilon_s - \varepsilon_\theta)^2 + 2(-\varepsilon_t - \varepsilon_\theta)^2$$

$$= 4 (\varepsilon_t^2 + \varepsilon_s^2 + \varepsilon_\theta^2) + 4 (\varepsilon_s \varepsilon_t + \varepsilon_\theta \varepsilon_t + \varepsilon_\theta \varepsilon_s) \qquad (4.11)$$

The incompressibility equation can also be expressed as

$$\varepsilon_s^2 + \varepsilon_t^2 + \varepsilon_\theta^2 = -2(\varepsilon_s \varepsilon_t + \varepsilon_t \varepsilon_\theta + \varepsilon_s \varepsilon_\theta) \qquad (4.12)$$

so that Eq. (4.11) is further reduced to

$$3 |\underset{\sim}{OP}|^2 = 2 (\varepsilon_t^2 + \varepsilon_s^2 + \varepsilon_\theta^2)$$

which gives the magnitude of vector OP as

$$|\underset{\sim}{OP}| = \sqrt{\frac{2}{3}} (\varepsilon_t^2 + \varepsilon_s^2 + \varepsilon_\theta^2)^{1/2} \qquad (4.13)$$

and inclination

$$\alpha = \tan^{-1} \left(\frac{Y}{X}\right) = \frac{\varepsilon_\theta - \varepsilon_s}{\sqrt{3} \ (\varepsilon_\theta + \varepsilon_s)} \qquad (4.14)$$

4.3 Triangular Co-ordinates for Strain Rates

Having obtained the states of strain involved in the bulge test, it is possible to pursue towards the strain rates. Just like strains, the principal strain rates have only two degrees of freedom as shown in Eq. (3.28), so that the triangular co-ordinate system may be used in the analysis of strain rates also.

In order to comply with the use of this co-ordinate system for strains, the vertical axis denotes the through-thickness strain-rate; and the left and the right hand axes represent the circumferential and meridional-tangential strain-rates, respectively. Therefore, the axis in Fig. (4.4) now represent the three principal strain rates. Referring to this figure, the point p shows the state of strain rates $(\dot{\varepsilon}_t, \dot{\varepsilon}_\theta, \dot{\varepsilon}_s)$ and is obtained by differentiating the strain path at that point $(\varepsilon_t, \varepsilon_\theta, \varepsilon_s)$ also in the triangular co-ordinate system. The direction of the radial line passing through the origin and $(\dot{\varepsilon}_t, \dot{\varepsilon}_\theta, \dot{\varepsilon}_s)$ is also that of the tangent at that point $(\varepsilon_t, \varepsilon_\theta, \varepsilon_s)$ on the strain path. The position vector $\underset{\sim}{OP}$ in the triangular co-ordinates for strain rates is also shown to be

$$|OP| = \sqrt{\frac{2}{9}} \left[(\dot{\varepsilon}_t - \dot{\varepsilon}_\theta)^2 + (\dot{\varepsilon}_\theta - \dot{\varepsilon}_s)^2 + (\dot{\varepsilon}_s - \dot{\varepsilon}_\theta)^2 \right]^{\frac{1}{2}} \qquad (4.15)$$

4.4 Triangular Co-ordinate System for Stresses

It has been indicated in the previous section that the triangular co-ordinates for strain are based on the fact that the sum of the three principal strains is zero. But unlike the strains, states of stress can not be plotted directly in the triangular co-ordinates because the three principal stresses, in general, do not add up to zero. However, the triangular co-ordinate system may be used for graphical representation of the stresses, if the following definitions are considered.

4.4.1 Hydrostatic and deviatoric stresses

The general three dimensional state of stress can be specified in terms of nine Cartesian components acting at a point by the following stress matrix

$$\begin{vmatrix} \sigma_{11} & \sigma_{12} & \sigma_{13} \\ \sigma_{21} & \sigma_{22} & \sigma_{23} \\ \sigma_{31} & \sigma_{32} & \sigma_{33} \end{vmatrix} \qquad (4.16)$$

In this stress matrix, the diagonal elements are the normal stresses and the non diagonal elements represent shear stresses. If the triaxial co-ordinate axes for the stress matrix in Eq. (4.16) are chosen so that the shear stresses vanish, then these three orthogonal axes represent the principal directions of the triaxial stresses.

Simultaneously, any triaxial state of stress can readily be denoted by a point in this stress space with $\sigma_1 \underset{\sim}{i}$, $\sigma_2 \underset{\sim}{j}$, $\sigma_3 \underset{\sim}{k}$ as three mutually perpendicular axes representing the scalar principal stresses as shown in Fig. (4.5). Thus, the stress matrix (4.16) becomes

$$\begin{vmatrix} \sigma_1 & o & o \\ o & \sigma_2 & o \\ o & o & \sigma_3 \end{vmatrix}$$

and the position vector $\underset{\sim}{OP}$ in this space is the stress vector written mathematically as

$$\underset{\sim}{OP} = \sigma_1 \underset{\sim}{i} + \sigma_2 \underset{\sim}{j} + \sigma_3 \underset{\sim}{k}$$

or in the matrix form

$$\begin{vmatrix} \sigma_1 \\ \sigma_2 \\ \sigma_3 \end{vmatrix} = \begin{vmatrix} \sigma_1 & o & o \\ o & \sigma_2 & o \\ o & o & \sigma_3 \end{vmatrix} \times \begin{vmatrix} \underset{\sim}{i} \\ \underset{\sim}{j} \\ \underset{\sim}{k} \end{vmatrix} \qquad (4.17)$$

It is often desirable to split the stresses $(\sigma_1, \sigma_2, \sigma_3)$ into two components of which one is the mean stress, that is

$$\begin{vmatrix} \sigma_1 \\ \sigma_2 \\ \sigma_3 \end{vmatrix} = \left[\begin{vmatrix} \frac{\sigma_1 + \sigma_2 + \sigma_3}{3} & o & o \\ o & \frac{\sigma_1 + \sigma_2 + \sigma_3}{3} & o \\ o & o & \frac{\sigma_1 + \sigma_2 + \sigma_3}{3} \end{vmatrix} + \begin{vmatrix} \frac{2\sigma_1 - \sigma_2 - \sigma_3}{3} & o & o \\ o & \frac{-\sigma_1 + 2\sigma_2 - \sigma_3}{3} & o \\ o & o & \frac{-\sigma_1 - \sigma_2 + 2\sigma_3}{3} \end{vmatrix} \right] \times \begin{vmatrix} \underset{\sim}{i} \\ \underset{\sim}{j} \\ \underset{\sim}{k} \end{vmatrix}$$

or $\sigma_{ij} = \sigma_m + \sigma'_{ij}$ (4.18)

where $\sigma_m = 1/3\ (\sigma_1 + \sigma_2 + \sigma_3)$

The mean stress σ_m given by the first invariant I_1, is also termed the hydrostatic component of stress. The combination of the second and third invariants I_2 and I_3, is called deviatoric or reduced component of stress σ'_{ij}. The equation (4.18) may be written in matrix form as

$$\begin{vmatrix} \sigma_1 \\ \sigma_2 \\ \sigma_3 \end{vmatrix} = \left[\begin{vmatrix} \sigma_m & o & o \\ o & \sigma_m & o \\ o & o & \sigma_m \end{vmatrix} + \begin{vmatrix} \sigma'_1 & o & o \\ o & \sigma'_2 & o \\ o & o & \sigma'_3 \end{vmatrix} \right] \times \begin{vmatrix} \underset{\sim}{i} \\ \underset{\sim}{j} \\ \underset{\sim}{k} \end{vmatrix} \qquad (4.19)$$

or $\underset{\sim}{OP} = \sigma_m (\underset{\sim}{i} + \underset{\sim}{j} + \underset{\sim}{k}) + (\sigma'_1 \underset{\sim}{i} + \sigma'_2 \underset{\sim}{j} + \sigma'_3 \underset{\sim}{k})$ (4.20)

and $\sigma'_1 + \sigma'_2 + \sigma'_3 = o$ (4.21)

In Fig. (4.5), the hydrostatic axis can be viewed geometrically as along an axis passing through the origin of the vector space and making equal angles with axes $\sigma_1 \underset{\sim}{i}$, $\sigma_2 \underset{\sim}{j}$, $\sigma_3 \underset{\sim}{k}$ and, the hydrostatic stress (line $\overline{pp'}$) has direction cosines $(\frac{1}{\sqrt{3}} \cdot \frac{1}{\sqrt{3}} \cdot \frac{1}{\sqrt{3}})$ with the three principal axes. The deviatoric stress (line $\overline{OP'}$) is also

shown to lie in the deviatoric or π plane of equation $\sigma_1 + \sigma_2 + \sigma_3 = o$. It is well known that a moderate hydrostatic pressure either applied alone or superposed on some state of combined stress does not affect yielding of metals to the first approximation (78). This means that hydrostatic stresses produce only elastic dilatation which is recoverable on removal of the stresses. Consequently, it can be said that plastic deformation can only occur by the action of deviatoric stresses. The Mohr circles for stress (σ_1, σ_2, σ_3) shown in Fig. (4.6) can also be used to find the deviatoric stresses.

4.4.2 Triangular co-ordinates for deviatoric stresses

It has been shown in the previous section that the sum of the three deviatoric stresses is zero (Eq. 4.21). This property enables us to use the triangular co-ordinate system for representation of states of deviatoric stress. Like states of strain, states of deviatoric stress components are readily shown as points in the triangular co-ordinate system described earlier, just by knowing any two of the three deviatoric stresses. In order to obtain the stress-strain and stress-strain rate relationships, it is necessary that the assignment for the axes for deviatoric stresses corresponds to that for strains and strain rates. It means that in the triangular co-ordinate system for deviatoric stresses, the vertical axis represents σ'_t and the right and left hand side of σ'_t axis denote σ'_s and σ'_θ axes respectively. It can be

seen from Fig. (4.7) that with this system of graphical representation, recovery of states of stress (in space) is not possible, because the magnitude of the hydrostatic components are not shown. The position vector $|\underset{\sim}{OP}|$ is readily shown to be

$$|\underset{\sim}{OP}| = \sqrt{\frac{2}{9}} \left[(\sigma_t - \sigma_\theta)^2 + (\sigma_\theta - \sigma_s)^2 + (\sigma_s - \sigma_t)^2\right]^{\frac{1}{2}} \qquad (4.22)$$

The method of arriving at this equation is similar to that for strains, in Eq. (4.13), together with the following property,

$$\begin{aligned} \sigma'_t - \sigma'_\theta &= \sigma_t - \sigma_\theta \\ \sigma'_\theta - \sigma'_s &= \sigma_\theta - \sigma_s \\ \sigma'_s - \sigma'_t &= \sigma_s - \sigma_t \end{aligned} \qquad (4.23)$$

The magnitude of the deviatoric component $\underset{\sim}{\sigma'}$ given by part of Eq. (4.20) can be shown to be

$$\begin{aligned} \sigma' &= (\sigma'^2_t + \sigma'^2_s + \sigma'^2_\theta)^{\frac{1}{2}} \\ &= \sqrt{\frac{1}{3}} \left[(\sigma_t - \sigma_s)^2 + (\sigma_s - \sigma_\theta)^2 + (\sigma_\theta - \sigma_t)^2\right]^{\frac{1}{2}} \end{aligned} \qquad (4.24)$$

Therefore, any position vector in such a co-ordinate system has a magnitude proportional to the deviatoric stress component through the equation

$$|\underset{\sim}{OP}| = \sqrt{\frac{2}{3}}\ \sigma' \qquad (4.25)$$

The position vector $|\underset{\sim}{OP}|$ is also proportional to the effective stress shown by the equation

$$|\underset{\sim}{OP}| = \frac{2}{3}\bar{\sigma} \qquad (4.26)$$

The mode of the deviatoric stress system can be defined by a characteristic index (ζ), similar to that for the triangular co-ordinates for strain. Therefore, the deviatoric stress ratios ($\sigma_t' : \sigma_s' : \sigma_\theta'$) can be related to a particular line of the 12, emerging from the origin of the axes (ζ = 4, 8, 12) represent uniaxial tension and the negative branches (ζ = 2, 6, 10) denote uniaxial compression through the following equation:-

$$\sigma_i' = \sigma_j' = -\frac{\sigma_k'}{2} \qquad (i, j, k = t, s, \theta) \qquad (4.27)$$

Similarly, odd values of ζ represent pure shears whose states of deviatoric stress are given by

$$\sigma_i' = 0 \quad \sigma_j' = -\sigma_k' \qquad (i, j, k = t, s, \theta) \qquad (4.28)$$

showing pure shear systems of

$$\sigma_i = 0 \quad \sigma_j = -\sigma_k$$

Therefore, any position vector in this co-ordinate system is sufficient to determine the characteristic index for deviatoric stresses (ζ), as well as the effective stress ($\bar{\sigma}$). Unfortunately the principal stresses, or the applied stress state cannot be recovered because of the absence of the hydrostatic component.

An alternative method may be used to represent the states of stress in the triangular co-ordinate system. This is best demonstrated by considering the projection of the stress states, such as vector $|\underset{\sim}{OP}|$ in Fig. (4.5) on to the π -plane by looking along the hydrostatic axis. This means that hydrostatic stresses are neglected. The positive principal axes $o\sigma_1$, $o\sigma_2$, $o\sigma_3$ appear in the π-plane, Fig. (4.8), inclined at 120° to each other. The co-ordinates of vector $|\underset{\sim}{OP}|$ in Fig. (4.5) appear in Fig. (4.8) as the projected lengths

$$OM = \sqrt{\frac{2}{3}}\,\sigma_1 \,, \quad MN = \sqrt{\frac{2}{3}}\,\sigma_2 \,, \quad NP' = \sqrt{\frac{2}{3}}\,\sigma_3 \,.$$

By resolving vector OP' along σ_2 ($\zeta = 12$) and the line perpendicular to it ($\zeta = 3$), then,

$$X = \sqrt{\frac{2}{3}}\,\sigma_2 - \sqrt{\frac{2}{3}}\,\sigma_3 \cos 60^\circ - \sqrt{\frac{2}{3}}\,\sigma_1 \cos 60^\circ$$

$$= \sqrt{\frac{1}{6}}\,(2\sigma_2 - \sigma_3 - \sigma_1)$$

and

$$Y = \sqrt{\frac{2}{3}}\,\sigma_1 \cos 30^\circ - \sqrt{\frac{2}{3}}\,\sigma_3 \sin 60^\circ$$

$$= \sqrt{\frac{1}{2}}\,(\sigma_1 - \sigma_3)$$

so that

$$OP' = \sqrt{(X^2 + Y^2)} = \left[\frac{1}{6}\,(2\sigma_2 - \sigma_3 - \sigma_1)^2 + \tfrac{1}{2}(\sigma_3 - \sigma_1)^2\right]^{\frac{1}{2}}$$

$$OP' = \sqrt{\frac{1}{3}}\,\left[(\sigma_1 - \sigma_2)^2 + (\sigma_2 - \sigma_3)^2 + (\sigma_3 - \sigma_1)^2\right]^{\frac{1}{2}} \qquad (4.29)$$

and

$$\alpha = \tan^{-1}\left(\frac{\sqrt{3}\,(\sigma_1 - \sigma_3)}{2\sigma_2 - \sigma_3 - \sigma_1}\right) \qquad (4.30)$$

With this method, the length of any position vector reads the deviatoric component of a stress state (σ_t, σ_θ, σ_s,) and is consequently proportional to the effective stress given by the following equation:-

$$OP = \sigma' = \sqrt{\frac{2}{3}}\ \bar{\sigma} \qquad (4.31)$$

Fig. (4.9) represents the Mohr stress circles for some typical stress systems.

4.5 Stress-Strain and Stress-Strain Rate Relationships in the Triangular Co-ordinate System

The stress, strain and strain-rate relationships of the material during deformation can be derived by superposing the three sets of triangular coordinates for stress, strain and strain-rate one on to the other; and study the relationships in vectorial form. For each point on the specimen there are three vectors for $\bar{\sigma}$, $\bar{\varepsilon}$ and $\dot{\bar{\varepsilon}}$.

In the simplest case of a radial strain path, symmetry requires that these three vectors are collinear and the relations are as in the uniaxial case. In such a case it is impossible to separate the strain-dependent and the strain-rate-dependent parts of the stress in a single test. In the case where the vector for stress is always parallel to the corresponding vector for strain, the material is not strain rate sensitive (e.g. ordinary

ductile material). It is very unlikely, though theoretically possible, that the strain-rate may influence the magnitudes of, but not the ratio between the stresses. In the case where the vector for stress is always parallel to the corresponding vector for strain-rate, the material is a liquid.

In general, the vectors for stress, strain and strain-rate are all in separate directions. Then, it is possible to find, at any point on the stress path, a strain-proportional and a strain-rate-proportional component. Thus, let $\bar{op}$ in Fig. (4.10a) be the vector for stress and the associate vectors for strain ($\bar{\varepsilon}$) and strain-rate ($\bar{\dot{\varepsilon}}$) are as shown. By resolving the vector $\bar{op}$ in the two components along $\bar{\varepsilon}$ and $\bar{\dot{\varepsilon}}$ we get om as the strain-proportional component and on as the strain-rate-proportional component of the stress.

The vector for stress can not lie outside the acute angle formed by $\bar{\varepsilon}$ and $\bar{\dot{\varepsilon}}$. Suppose it does lie outside the angle on the side of the strain-rate vector (Fig. 4.10b), then the strain-proportional component of the stress must be in the opposite direction to the strain vector. In an ordinary ductile material, such stresses occur only when the strain path is abruptly reversed, as when observing the Bauschinger effect. If, on the other hand, the vector for stress lies outside the angle on the side of the strain vector (Fig. 4.10c), then the strain-rate-proportional component of the stress is opposite to

the strain-rate vector, resulting in a reversed energy flow from the material to the testing apparatus. Thus, the vector for stress must normally lie between the strain and the strain-rate vector. In the case under consideration; the strain path is nearly radial and there are no sudden turns, let alone reversals.

The two components of the stress vector are shown in Fig. (4.10a). The resultant stress is

$$\bar{\sigma} = \bar{\sigma}_{\varepsilon} + \bar{\sigma}_{\dot{\varepsilon}} \qquad (4.32)$$

By Sine Law

$$\frac{\bar{\sigma}_{\varepsilon}}{\sin \alpha} = \frac{\bar{\sigma}_{\dot{\varepsilon}}}{\sin \beta} \qquad (4.33)$$

or

$$\frac{\bar{\sigma}_{\varepsilon}}{\bar{\sigma}_{\dot{\varepsilon}}} = \frac{\sin \alpha}{\sin \beta} = Z \qquad (4.34)$$

Z represents the ratio of the solid to liquid behaviour; and the sum of the two angles $(\alpha + \beta)$ represents, roughly speaking, the curvature of the strain path.

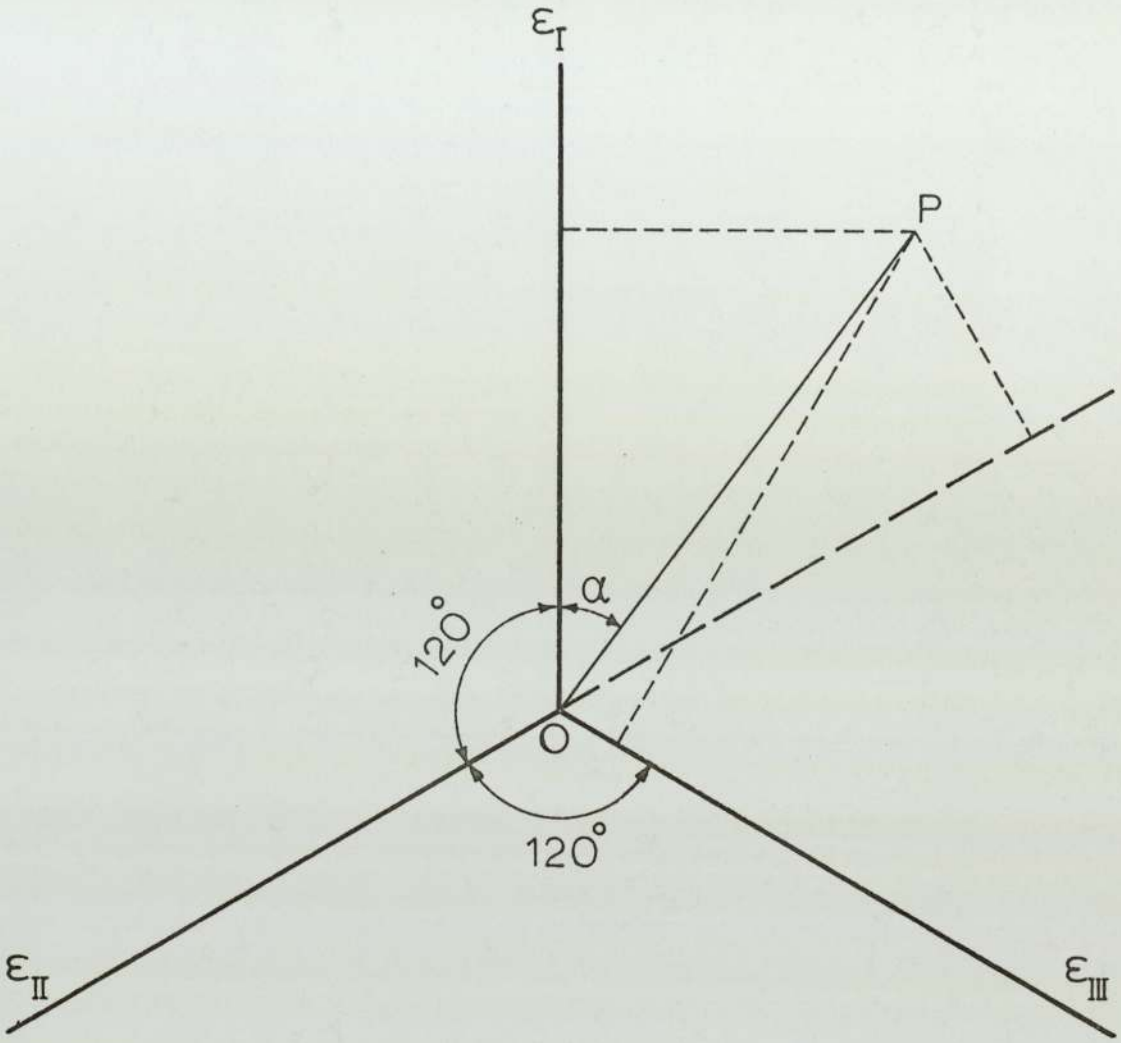

Fig. 4-1 – Triangular coordinate system.

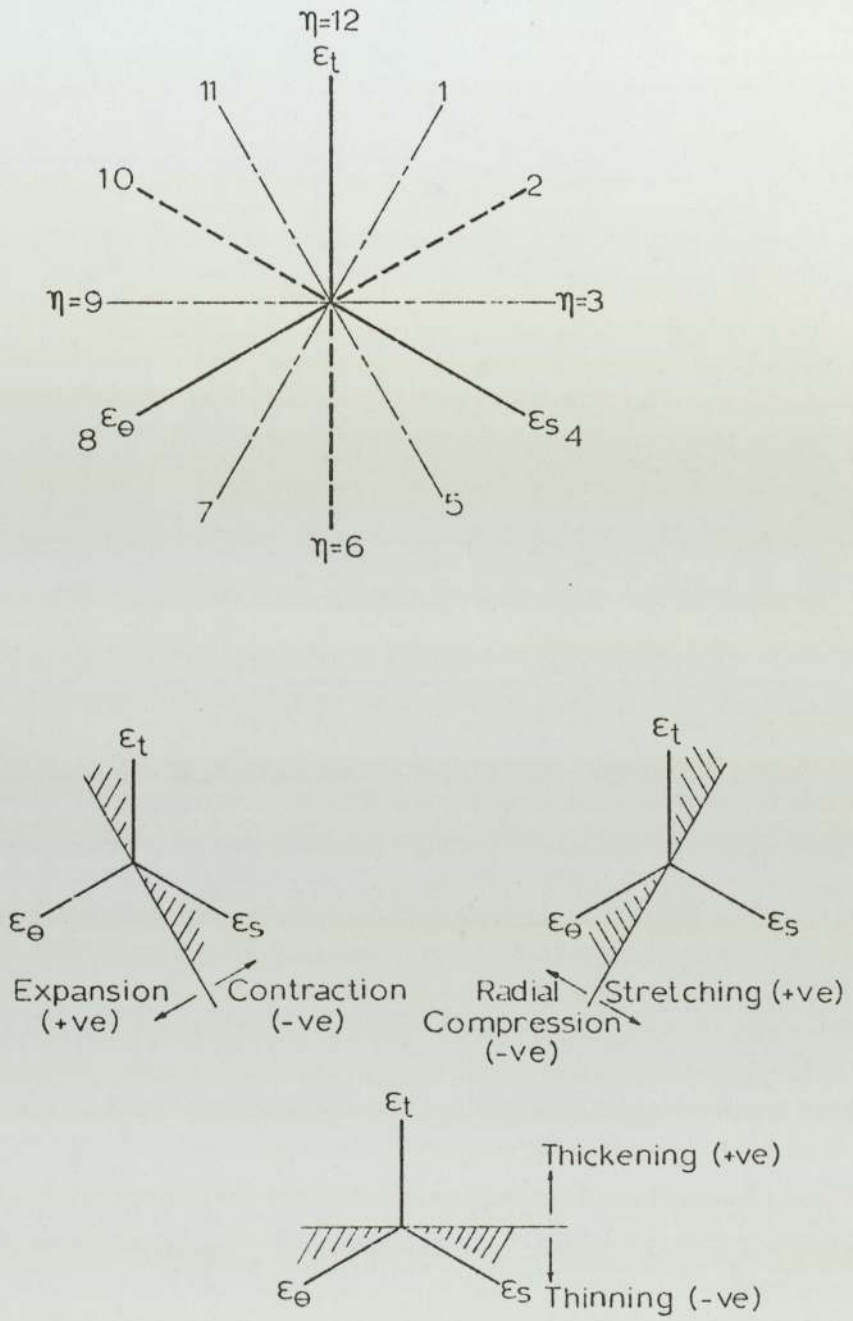

Fig. 4-2 – Regions of tensile and compressive strains in the triangular coordinates, after Hsü (76).

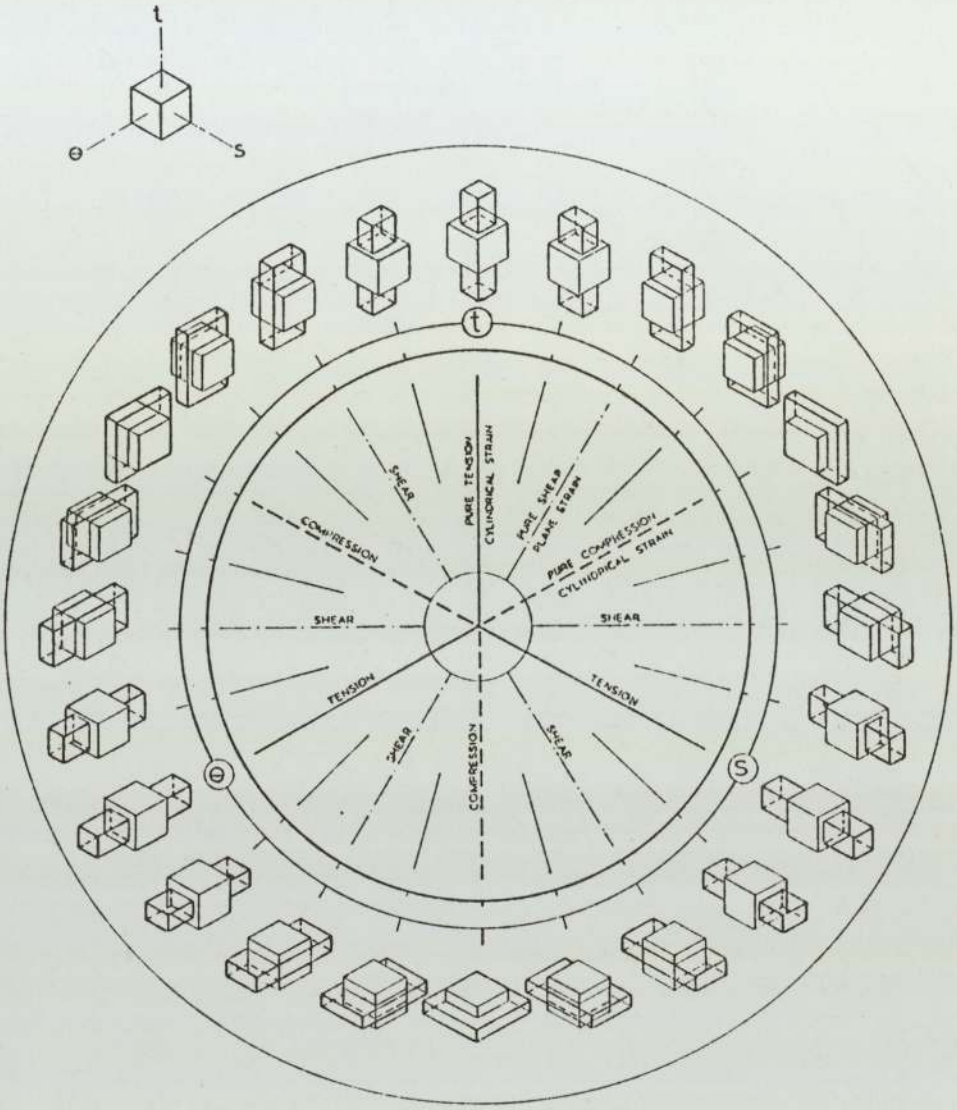

Fig. 4-3 – Deformations of a cube corresponding to different values of the characteristic index , after Hsü (72).

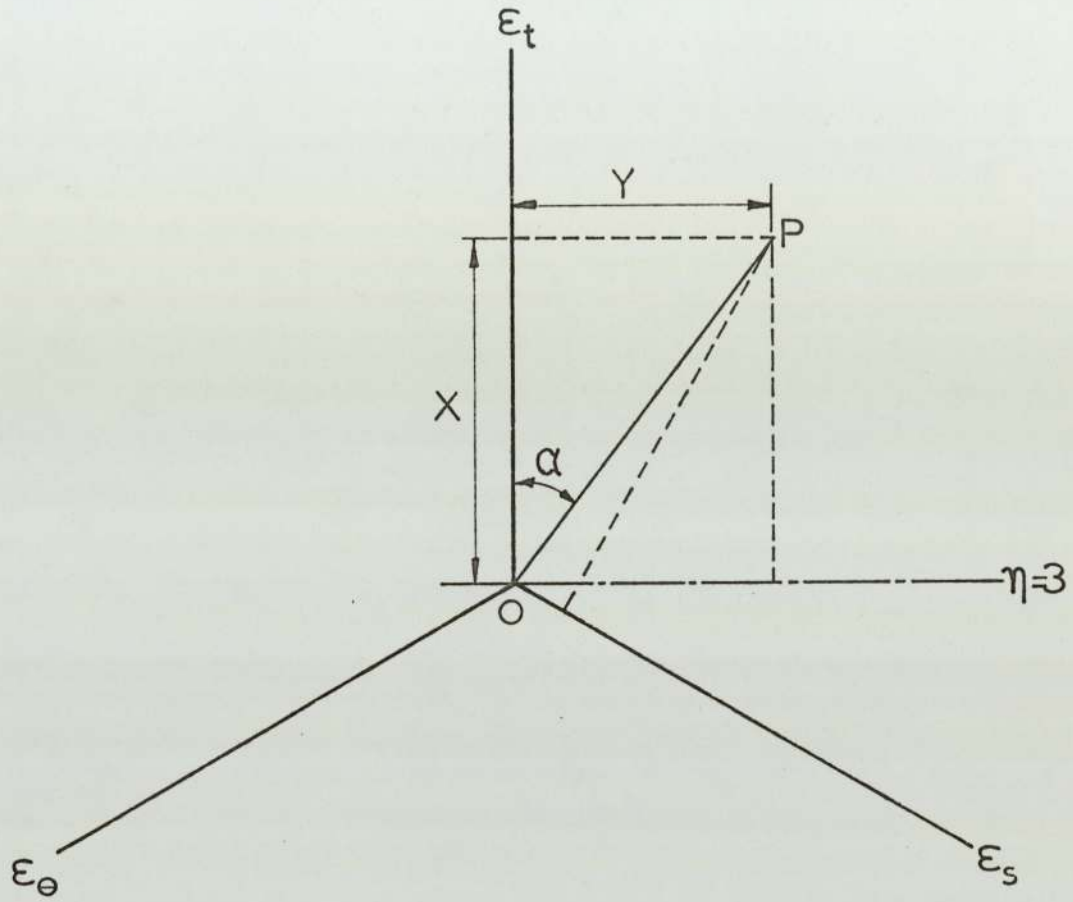

Fig. 4. 4 – The strain vector in triangular coordinates.

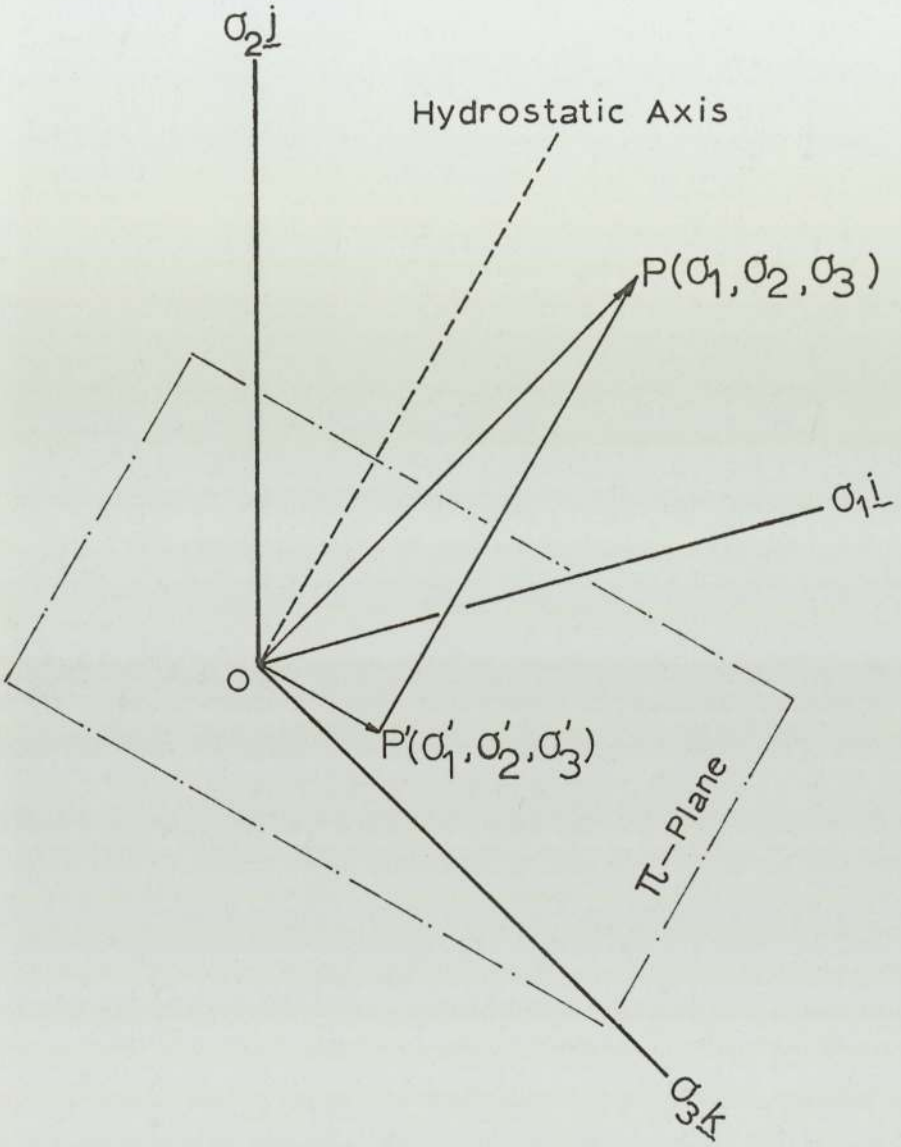

Fig. 4.5 - Hydrostatic and deviatoric stresses.

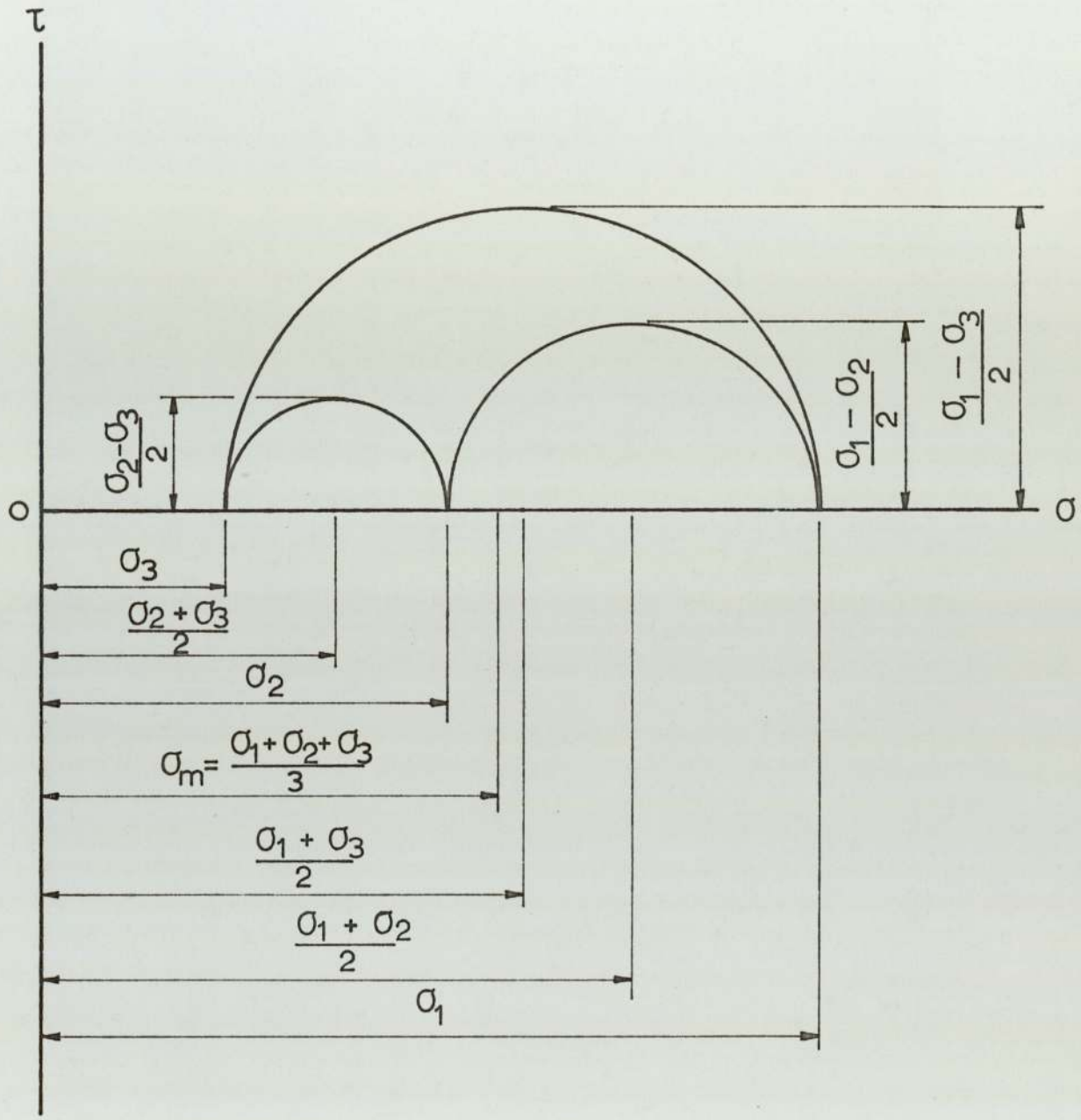

Fig. 4-6 – Mohr stress circles.

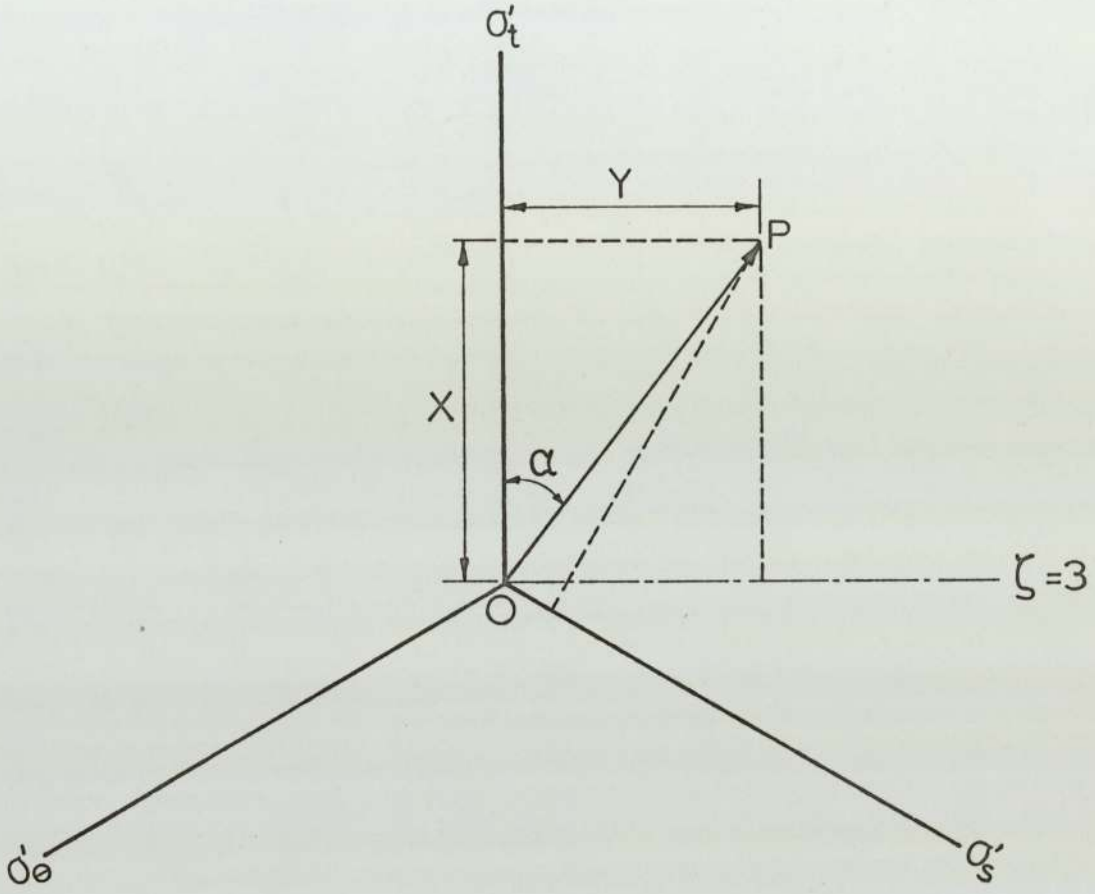

Fig. 4.7 – Deviatoric stress in triangular coordinates.

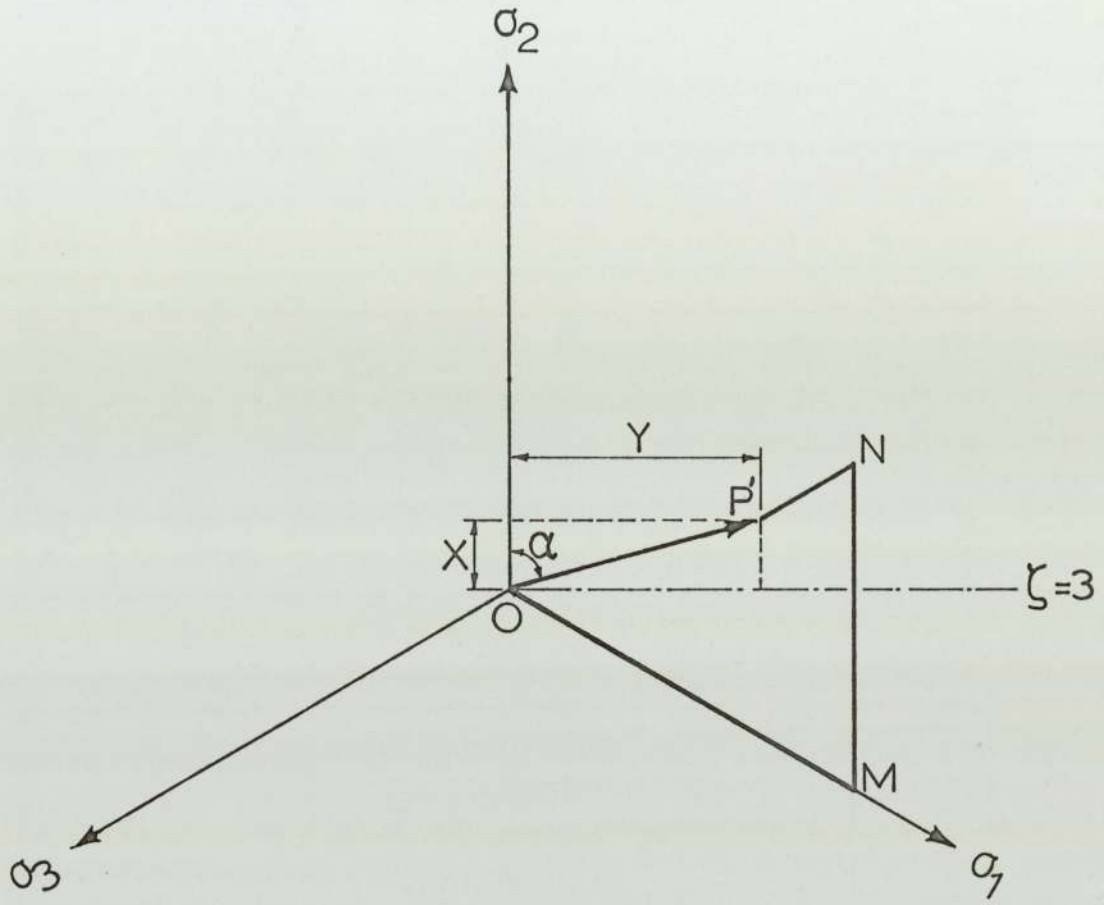

Fig. 4-8 – Projection technique for deviatoric stress.

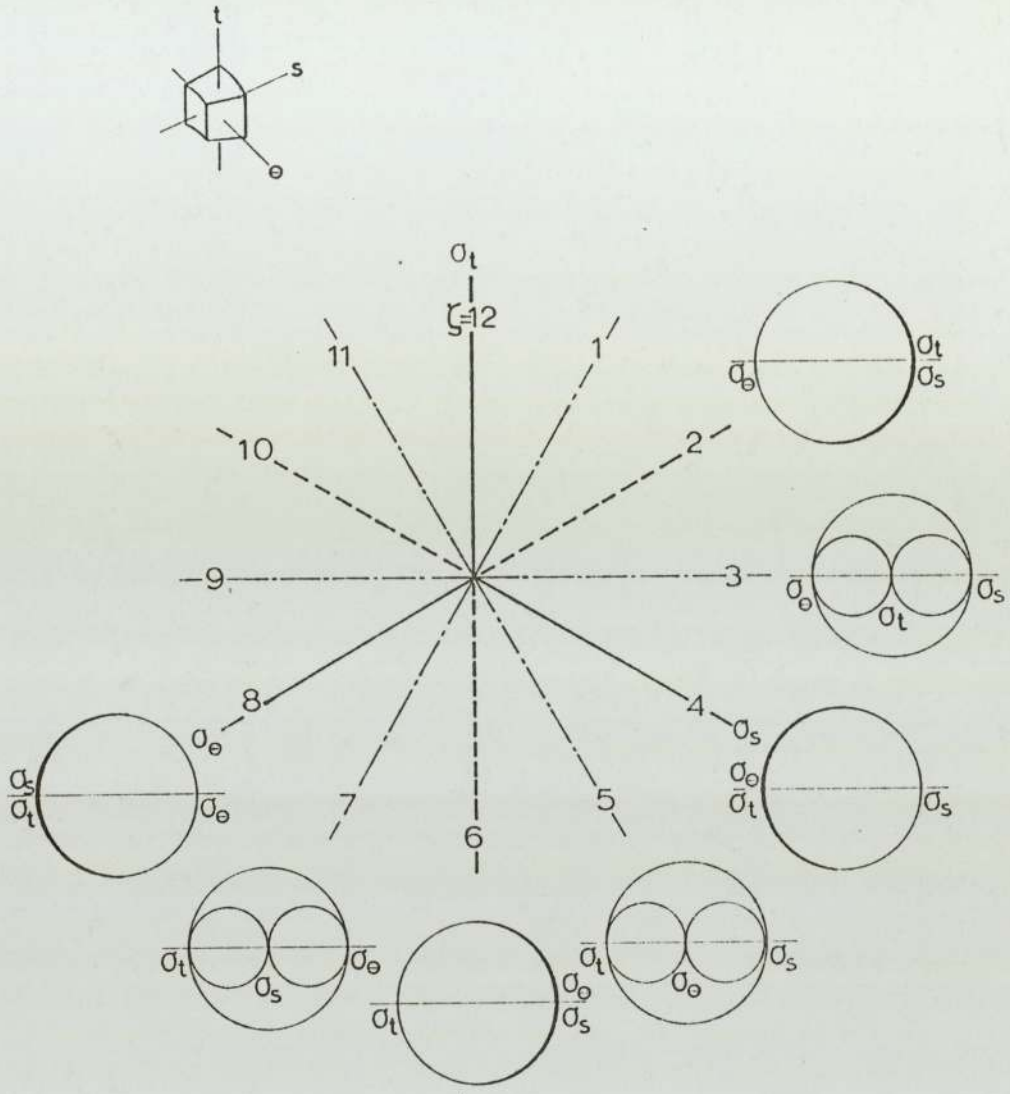

Fig. 4-9 – Triangular coordinates for deviatoric stresses.

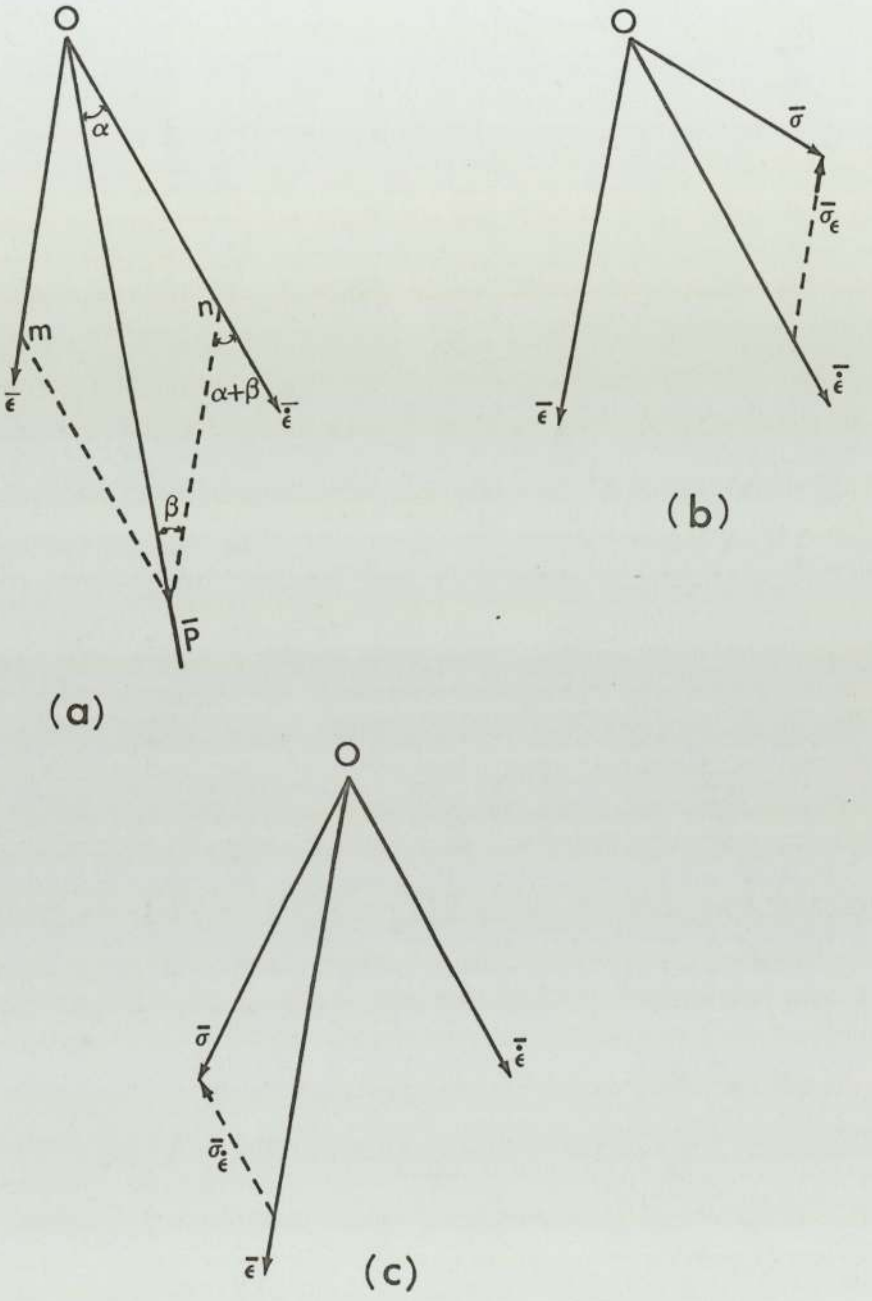

Fig. 4.10 - The strain-proportional and the strain-rate-proportional components of the stress vector.

PART B

EXPERIMENTS & RESULTS

CHAPTER 5

MATERIAL PREPARATION

&

EXPERIMENTAL EQUIPMENT

Chapter 5

Material preparation and Experimental Equipment

5.1 Material Preparation

The mechanical behaviour of superplastic materials can be varied widely by processing. Impurities and alloying additions have a similar effect due to alteration in microstructure and boundary precipitation. The material used for the measurements given in this project was supplied by Imperial Smelting Corporation in the form of sheets 1170 x 640 x 2.54 mm, 1350 x 545 x 1.91 mm and 1500 x 600 x 1.27 mm in the heat treated condition, from which specimens for the bulge test were cut. The alloy was based on the zinc-aluminium eutectoid (77.5% Zn, 22% Al) to which 0.5% copper was added to improve its creep properties.

The forming specimens were sheared in the form of square sheets 172 mm x 172 mm from which circular blanks of 170 mm diameter were machined by sandwiching the blanks between backing plates pressed firmly between the head and tail stock of a lathe. The specimens were checked for thickness uniformity and surface smoothness and those with scratchy surfaces or thickness variations exceeding 0.01 mm within a specimen were rejected. Prior to forming, physical contaminants such as dirt or oxides on the surface of the blanks were removed by using scouring powder. A photographic technique was used to print a grid of concentric circles

and radial lines on each specimen surface for the measurements of the geometrical transformation of the material particles after deformation.

5.2 The grid printing technique

(A)- Equipment

(1) A specially designed rig for producing repeatable grids and for locating the negative accurately in the centre of the specimen.

(2) A turntable rotating at 80 r.p.m. - for spreading and drying the photoresist evenly on the surface of the specimen.

(3) An ultra-violet lamp (wave length 3650 Å) connected to a choke - for exposing the photo-resist.

(B)- Chemicals

(1)- Trichlorethylene - a chemical used for cleaning of organic contaminants such as grease in the form of finger marks or as a film.

(2)- Kodak Photo-Resist Type 3 - a chemical which becomes light sensitive when dried.

(3)- Kodak Ortho Resist Developer and Kodak Photo Resist Dye (black) - a mixture of these two chemicals (ratio of 1 : 1) used for desolving the unexposed area of the photo-resist and colouring the exposed area.

(C)- Printing process

The procedure of printing was as follows:-

(1)- The surface of the specimen was cleaned to

ensure good adhesion of photo-resist using tri-chlorethylene and then washed thoroughly to remove any traces of detergent. Oil-free compressed air was used to dry the specimen.

(2)- The specimen was mounted in the centre of the turntable. Photo-resist was then poured on to the specimen to flood the surface. The turntable was then whirled to spin off the excess resist for a period of about 30 seconds. The table was then stopped and the material removed for drying in air.

(3)- The uniformly coated specimen was located on to the specially designed rig for printing.

(4)- The chosen negative (grid of concentric circles, 2 mm pitch) was placed in the centre of the specimen and was mounted in close contact with the coated surface by using a cylindrical weight.

(5)- The ultra-violet light was then switched on for 3½ minutes.

(6)- The exposed specimen was then immersed in the dye developer for about 2 minutes with agitation of the dye developer.

(7)- After a spray water wash, the specimen was dried by using air knife.

5.3 Apparatus

5.3.1 Die Set

The die set consisted of two parts fabricated from mild steel. The sheet to be bulged was clamped between the hold down ring (clamping ring) and the die (base

plate) by tightening the nuts on the six 12 mm diameter studs extended upward from the clamping ring and spaced uniformly along a pitch of 240 mm diameter, as shown in Fig. (5.1). A torque spanner set at 140 NM was used to ensure the uniformity of the pressure on the clamping ring. The split clamping ring had an aperture diameter of 142 mm, rounded at its inner edge to a radius of 4 mm to prevent the specimen from fracturing at its periphery. The surfaces of the clamping ring and the base plate contacting the specimen were serrated with mating grooves of 3 mm pitch and 1.5 mm deep in an annular area from 145 mm to 163 mm in diameter (see Fig. 5.1). These grooves prevented all movement of the flange during the forming process. The die set was fixed inside the oven by four 12 mm diameter bolts.

5.3.2 Oven

The basic parameters dictating the selection of the oven are as follows:-

(a)- The optimum superplastic behaviour of the material used in this investigation occurs around 270 °C. This temperature should be achieved in a short period of time in order to avoid any possible structural change of the material.

(b)- Maintaining a uniform temperature distribution over the specimen during the forming process is important as the optimum superplasticity occurs over a narrow temperature range.

(c)- The specimen should be observed during the whole forming process for measurement of the bulge rate. Therefore, the door of the oven should be of pyrex or similar heat resisting transparent material.

In the light of the above parameters a medium size oven with a transparent door was chosen and four electric resistance heating elements each of 1000 watts were installed at the bottom of the oven. These heating elements were controlled independently in order to minimise the temperature variations and compensate the heat losses during the clamping of the specimen. Thermostats of bulb type sensor capable of controlling temperature to within $\pm$ 2 °C in the temperature range 200 °C - 350 °C were used to control the heating elements. Ten thermocouples of Chromel/Alumel insuglass insulated wires, were attached to various parts of the oven and the die to ensure the uniformity of temperature. It was found that the variation of temperature could be maintained to within $\pm$ 5 °C.

5.3.3 Pneumatic circuit

The pneumatic circuit consisted of a cylinder of nitrogen gas connected to a set of pressure regulators. Two push button manually-operated valves were used to admit the gas into the forming chamber and release the built-up pressure from the bulged specimen. Pressure regulators were used so that forming pressure could be

selected prior to testing. Pressure at the regulators and at the forming chamber were recorded by two sets of pressure gauges. Prior to testing, nitrogen was passed through a pre-heating coil installed inside the oven.

5.3.4 Bulge rate monitoring device

In the study of the mechanical behaviour of superplastic materials, it is required to measure the strain rates which are expressed in terms of time (T). Thus, time is a very important factor and should be measured accurately. G.J. Cocks et. al. (61) have monitored their bulge rates with a dial gauge connected to a lightweight probe in contact with the specimen. They found that the bulged specimens of copper alloys were not constrained by the probe. However, in our experiments an attempt was made to use the same type of equipment, but the results showed that any direct contact between the bulged specimen and the bulge rate monitoring device would constrain the specimen, especially at the final stage of the process. At this stage the bulged specimen behaves like a toy balloon and even a very small force will prevent the normal geometrical transformation of the material particles. Therefore, a new technique had to be employed. A cylindrical glass of pyrex graduated in 5 mm intervals was placed on the orifice of the die and the bulge rates were monitored by observation. The coincidence of the apex of the bulged specimen with each line on the glass was recorded as height and the corresponding time was measured by a stopwatch. The cylindrical glass and other equipment are shown in Fig.(5.2).

5.3.5 Measuring Instrument

1. A two-dimensional travelling microscope reading to 0.02 mm for measuring the current (projected) radius of the bulge.

2. A workshop protractor reading to 5 min. for measuring the profile slope of the bulge. A magnetic stand placed on the surface plate was used to guide the movement of the protractor so that accurate meridional slope is ensured.

3. A stand vernier reading to 0.02 mm for measuring the axial (longitudinal) displacement of the bulge.

It must be mentioned at this stage that throughout the experiments no measurement was made at the rim of the bulge, since the material in this region is formed not only by the membrane stress but by bending as well. The membrane stress in the material in this region, must, of course, also conform to Eq. (3.2), but the uncertainty of the frictional and normal stress on the die surface makes it unrewarding to analyse them.

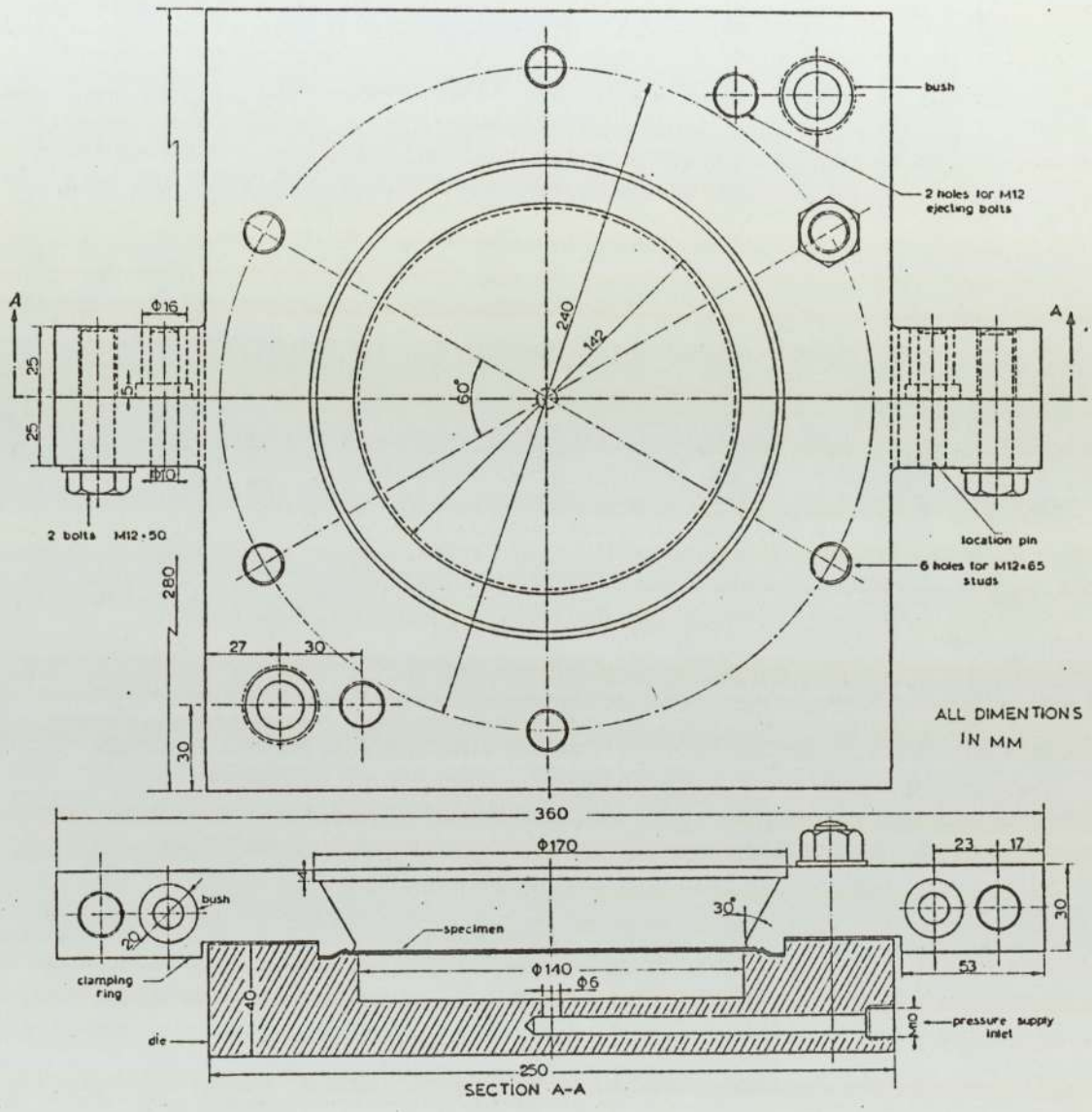

Fig. 5-1_ Detailed diagram of the die set.

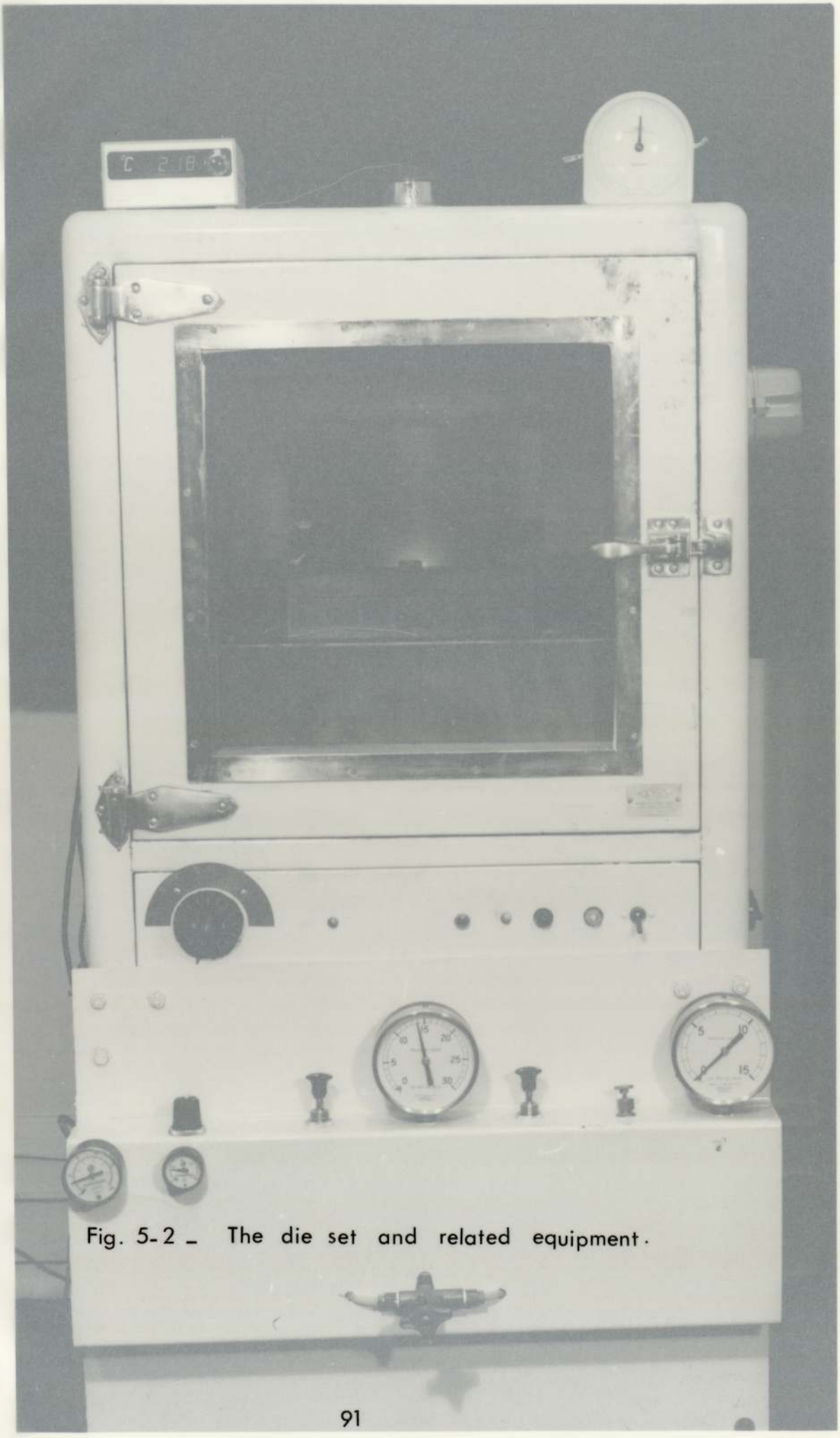

Fig. 5-2 _ The die set and related equipment.

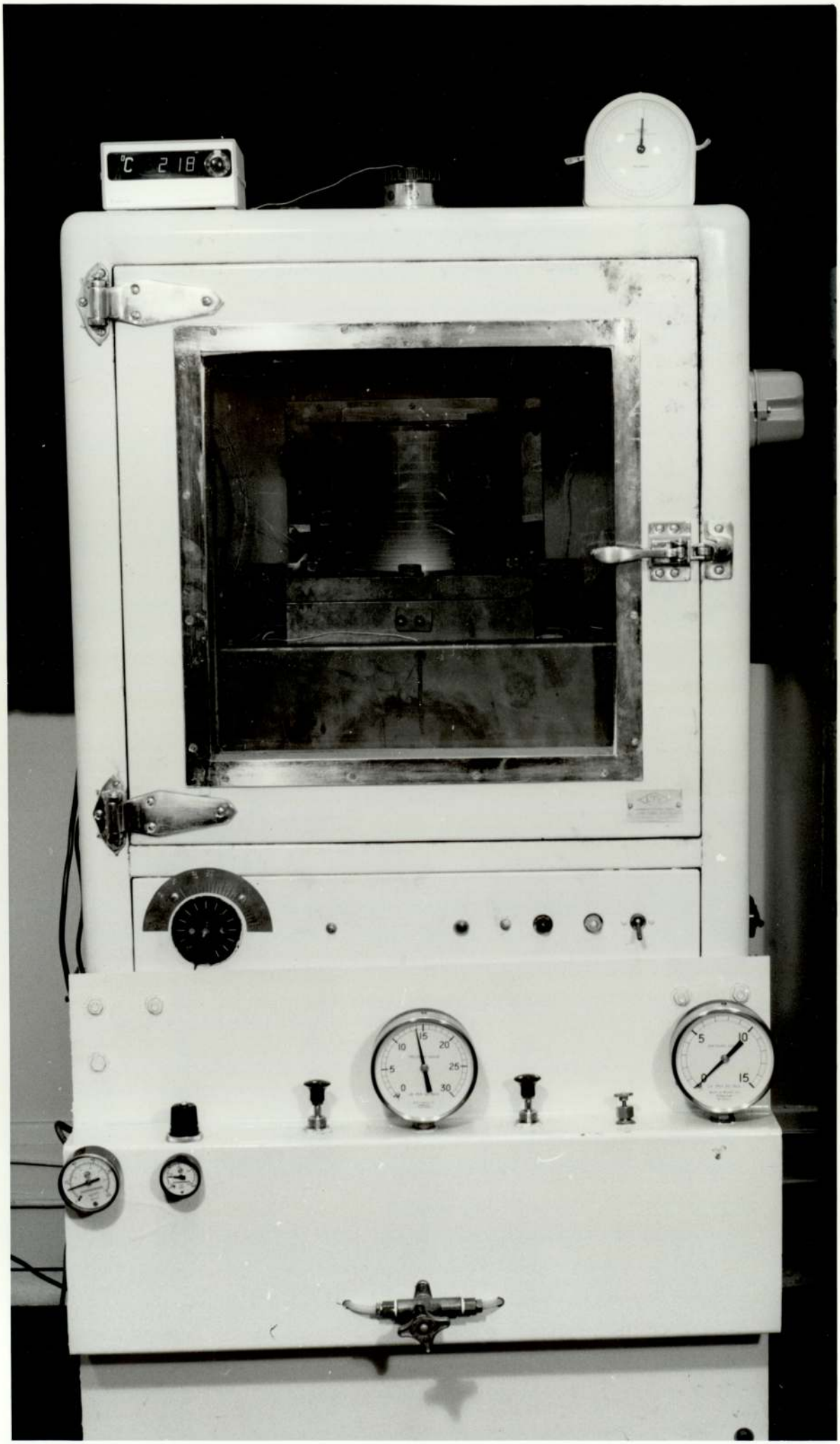
°C 218

CHAPTER 6

BEHAVIOUR OF THE WORK MATERIAL IN THE BULGE TEST

Chapter 6

Behaviour of the work material in the bulge test

It is shown in Chapter 3 that the mechanical properties of the material in the bulge test can be determined through the geometry of the shell. However, it is essential to keep in mind that the geometry of the bulge itself varies widely at different testing conditions. Therefore, it is necessary to investigate the geometry of the bulge under a particular testing condition.

The major factors affecting the forming behaviour of superplastic materials are temperature, strain-rate and grain size. Since the effect of grain size on the bulge behaviour of Zn-Al eutectoid alloy is reported elsewhere (58), and because the material used in this investigation was supplied in one grain size, therefore, this parameter is not considered.

Before discussing the other two factors, it is necessary to consider the effect of grain coarsening during the test and anisotropy of the material.

6.1 Effect of grain growth in the bulge test

It has been said earlier that one of the conditions for a material to behave superplastically is having a fine approximately equi-axed grain size, stable during deformation. In the case of Zn-Al eutectoid alloy,

however, limited grain growth is normally observed during superplastic deformation (55). It is generally agreed that changes in grain size during superplastic deformation depend upon the material, temperature and strain-rate. In the bulge test, in order to determine the stresses, each test must be run several times for the measurements of displacements at various stages. It means that the specimen is subjected to heat for a considerable period of time, and consequently this results in the occurrence of grain growth. Therefore, it is important to measure the rate of grain growth and to check whether this grain coarsening has any effect on the forming behaviour of the material.

In order to measure the rate of grain growth, an undeformed specimen having an initial grain size of less than 1 μm (Fig. 6.1a) was held at a temperature of 270 °C without stress for a period of 48 hr. and the final grain size was found to be less than 3 μm (see Fig. 6.1b). The bulge test was carried out on this specimen in order to check whether this small increase in grain size had any effect on the forming behaviour of the material, but no significant difference was observed between aged and as received specimens.

The microstructure of the specimens was also studied after the bulge test and detailed measurements of grain shape near the fracture of the bulged specimen revealed that the elongated grains of the initial micro-

structure (see Fig. 6.1a) became equi-axed and somewhat larger after deformation (Fig. 6.3).

6.2 Anisotropy effect in the bulge test

Superplastic materials are usually considered to be isotropic due to the absence of grain orientation, being a direct result of the grain structure prerequisite. However, Johnson et. al. (34) have shown that specimens of originally circular cross-section machined from hot rolled superplastic Zn-Al eutectoid alloy became elliptical when strained in the rolling direction which indicates the anisotropy of the material. In the present investigation a bulge of 142 mm diameter and polar height of 82 mm was produced and thickness strains were measured along and perpendicular to the direction of rolling. Fig. (6.4) shows a plot of thickness strain against initial radial position at 0° and 90° to the rolling direction. It can be seen that the thickness strains are distinctly higher at 0° except at the rim (undeformed part) and at the pole. Further analysis revealed that the stresses in the direction of rolling for a given strain rate are almost 10% higher than those in the transverse direction. Therefore, in the following experiments all the measurements are taken at 45° to the direction of rolling in order to obtain the average values.

6.3 Effect of temperature in the bulge test

The influence of temperature on flow stress, strain-rate and strain-rate sensitivity index in the uniaxial tensile test is well documented. The following effects are reported for Zn-Al eutectoid alloy.

1. The maximum attainable ductility increases with increasing temperature, and the highest degree of superplasticity occurs around 250°C, (15).

2. The overall level of the flow stress is reduced by increasing the temperature (55).

3. Under certain conditions superplastic behaviour is observed above the invariant temperature (275°C), but total elongation is considerably less than the value observed after deformation at 250°C, (83).

In the present investigation, similar effects were observed in the bulge test, but it is of value to mention that the bulge tests, at this stage, were performed mainly to elucidate the effect of temperature on the geometry and fracture of the bulge rather than its effect on ductility and level of flow stress.

Fig. (6.5) shows three bulged specimens formed to fracture at different sets of conditions of temperature and strain rate. Specimen A in Fig. (6.5) was formed at the optimum superplastic condition of 250°C and intermediate pressure (0.103 N/mm^2). Under these conditions the bulge grows to a height of about 180 mm (H/a = 2.68),

before it breaks at its pole, and takes the shape of a rugby football. The detailed studies of the fractured specimen under this condition reveals that the material fails due to severe thinning and the thickness of the material is nearly uniform over a relatively large area at the pole.

At temperatures below 250°C, the material still behaves superplastically, but only at higher pressure; and total surface strain is appreciable, though considerably less than the value obtained after bulging at 250°C. Specimen B in Fig. (6.5) which was formed at a temperature of 100°C and pressure of 0.345 N/mm^2, has reached the height of 102 mm, and fractured at the pole in a manner totally different from that observed after failing at 250°C. At low temperatures the material necks down to a very fine point at fracture, and at final stages of deformation, the bulge takes a conical shape. Fig. (6.6) shows the meridional sections (solid curves) and the particle trajectories (dotted curves) of specimen B, for the successive stages of deformation.

Finally, specimen C in Fig. (6.5) was formed at a temperature of 300°C and at a constant pressure of 0.69 N/mm^2. It is of value to mention that even at this temperature, which is well above the invariant temperature of 275°C, the material is strain rate dependent, but fails in an apparently brittle manner at a diffused neck.

The maximum attainable height is 62 mm (H/a = 0.87), which is nearly equal to the maximum height obtained in the bulging of non-superplastic material (84).

The peculiar behaviour of Zn-Al eutectoid alloy above the invariant temperature of 300°C may be explained in terms of microstructural change which is shown in Fig. (6.2). It can readily be seen from the figure that the fine two-phase initial microstructure (shown in Fig. 6.1a) is completely destroyed and has become a lamellar structure.

As seen from the above experiments, one of the interesting features of the bulge process on superplastic Zn-Al eutectoid alloy is the geometry of the instantaneous bulge profile which is closely related to the temperature. In practical application, however, the alloy is usually formed at optimum superplastic conditions of 250°C and intermediate strain rates. Thus, the bulk of the following sections involve the detailed examination of the bulge profile under the above conditions.

6.4 Geometrical transformation of material particles in the bulged specimen

The axial and radial displacements of each material particle are determined by the parametric equations given by Eq. (3.19) which is

$$l = l(r_o, T), \quad r = r(r_o, T).$$

In practice, however, it is easier to show the displacements by tracing out the profile of the product at successive stages than to express Eq. (3.19) analytically.

The radial movements of the material particles can adequately be elucidated by plotting the current radius against the original radius as shown in Fig. (6.7). It can be seen from this figure that the radial displacement is non-uniform along the specimen at every stage of deformation. The longitudinal displacements of the bulge profile at each stage of deformation are obtained through the measured inclination of the profile (θ) as

$$l = H - \int_o^r \tan \theta \, dr \qquad (6.1)$$

where H is the polar height of the bulge and the integral in Eq. (6.1) is obtained by a planimeter. The meridional sections of the deformed bulge on one side of the axis of symmetry for the successive stages of deformation are shown in Fig. (6.8) as solid lines. The dotted lines in Fig. (6.8) are the particle trajectories.

It is interesting to note that in the bulge test for non-superplastic materials the bulge rarely reaches a height equal to the radius of the die hole, whereas in the case of superplastic Zn-Al eutectoid alloy, the

sheets can be formed into a bulge of $H/a > 2.7$ before it breaks. The maximum bulge of a typical non-superplastic material is obtained from ref. (84) and its meridional section is plotted in Fig. (6.8) as a dotted line.

Actually, Fig. (6.8) does not represent all the experimental data that can be obtained in the bulge test of superplastic Zn-Al eutectoid alloy. The bulge grows to a height of 190 mm before it breaks at its pole, but only the data up to a height of 140 mm are shown in Fig. (6.8). Below 140 mm, the forming process is controlled by supplying, or shutting the supply of, the pre-heated nitrogen and the bulge ceases to grow once the gas supply is stopped. However, at some height between 140 and 150 mm, the bulge grows by itself even after the gas supply is turned off, showing that deformation continues with decreasing internal pressure. This unstable regime, which requires cinematographic experimental techniques to study, is not investigated in this project, but a qualitative analysis is given here for this peculiar behaviour. Suppose the bulge is idealised as a spherical shell of radius R, so that the stress σ is

$$\sigma = \frac{PR}{2t} \qquad (6.2)$$

considering that the volume of the shell material (V) remains constant at $(4\pi R^2 t)$ and that during expansion the pressure obeys the gas law

$$(\text{Pressure}) \times (\text{Volume}) = p \frac{4\pi}{3} R^3 = \text{constant } K \quad (6.3)$$

it can readily be seen in Eq. (6.2) that

$$\sigma = \frac{3K}{2V} \quad (6.4)$$

which is constant. In other words, according to Eq. (6.4) a bulge can grow without additional gas supply, with thinning shell and decreasing pressure, only if there is no strain-hardening. Actually, the bulge is not a sphere, but in the theory of membrane stresses (section 3.2), it can be seen that the arguments for a constant or nearly constant flow stress is valid. Hence, the strain-rate is the main factor governing the flow in this case.

6.5 Sphericality of the diaphragm in the bulge test

In the papers published on the bulge test of superplastic materials for most analyses a spherical bulge profile has been the major assumption made. It is shown in section (3.2.2) that this assumption is not true, because the prolateness of the surface ($\bar{P}$) in the bulge test is never constant. In order to study the local sphericality of the bulged specimen, the variation of the principal curvatures must be discussed first, since the sphericality of a shell is defined as the ratio of the principal curvatures.

6.5.1 Distribution of ρ_θ curve in the bulge test

The distribution of the radius of curvature in the circumferential direction may be obtained by considering its definition in conjunction with the definition of the index of sphericality (N),

$$N = \frac{\rho_\theta}{\rho_s} = \frac{r/\sin\theta}{dr/d(\sin\theta)}$$

so that

$$N \frac{dr}{d(\sin\theta)} = \frac{r}{\sin\theta} \qquad (6.5)$$

The ratio $(\frac{r}{\sin\theta})$ in Eq. (6.5) is the average slope of the r against $\sin\theta$ curve at any point, and $dr/d(\sin\theta)$ is the slope of the tangent to this curve. The index of sphericality (N) is always positive in order to have a close surface in the meridional section of the deformed shell (section 3.2.1). The prolateness ($\bar{P} = 1-N$) or oblateness (negative prolateness) of the dome, however, depends upon the relative magnitudes of the slopes in Eq. (6.5); it means that, when

$$\frac{dr}{d(\sin\theta)} > \frac{r}{\sin\theta} \quad \text{then} \quad N < 1$$

$$\frac{dr}{d(\sin\theta)} < \frac{r}{\sin\theta} \quad \text{then} \quad N > 1 \qquad (6.6)$$

$$\frac{dr}{d(\sin\theta)} = \frac{r}{\sin\theta} \quad \text{then} \quad N = 1$$

In order to show the ρ_θ distribution curve in relation to the r against $\sin\theta$ curve, it is necessary to approach from the definition of ρ_θ and its differential coefficient with respect to the current radius. Thus, differentiating Eq. (3.4) and combining the results of the differentiation with Eq. (3.9), we get

$$N = 1 - \sin\theta \frac{d\rho_\theta}{dr} \qquad (6.7)$$

comparison of Eq. (6.6) and (6.7) then yields,

$$\begin{aligned}
&\text{(a) if } \frac{d\rho_\theta}{dr} > o \quad \text{then } N < 1 \quad \text{and } \frac{dr}{d(\sin\theta)} > \frac{r}{\sin\theta} \\
&\text{(b) if } \frac{d\rho_\theta}{dr} < o \quad \text{then } N > 1 \quad \text{and } \frac{dr}{d(\sin\theta)} < \frac{r}{\sin\theta} \qquad (6.8) \\
&\text{(c) if } \frac{d\rho_\theta}{dr} = o \quad \text{then } N = 1 \text{ and } \frac{dr}{d(\sin\theta)} = \frac{r}{\sin\theta}
\end{aligned}$$

These three cases are shown in Fig. (6.9). As seen in this figure, when the r against $\sin\theta$ curve is sagging, ρ_θ is monotonically increasing, and when it becomes hogging, ρ_θ is monotonically decreasing. For a radial r against $\sin\theta$ curve, however, ρ_θ becomes a horizontal line.

As mentioned earlier, a real specimen cannot be any surface of constant N value, and the principal curvatures must have a variation along the bulge profile. Therefore, condition (b) in Fig. (6.9) cannot be valid.

From the set of bulged specimens shown in Fig. (6.10), it can readily be seen that in superplastic material the bulge grows not only in the longitudinal direction, but in the radial direction as well. The effect of this radial expansion on the r against $\sin\theta$ curve is a cusp at the angle of 90° as shown in Fig. (6.11).

To identify the variations in the circumferential radius of curvature, the following technique can be used on the experimental r against $\sin\theta$ curves. Around any curve from Fig. (6.11), say an intermediate stage f of polar height 80.2 mm, draw a radial line from the origin of the co-ordinate axes at a tangent to the curve (Fig. 6.12a). The initial segment (oa) of curve f intersects the radial line in an anticlockwise direction as shown by the arrowhead in Fig. (6.12a). Thus, at any point along the segment (oa), condition (c) of Eq. (6.8) is valid and ρ_θ is monotonically increasing. For the segment (ab) of curve f in Fig. (6.12a) which crosses the radial line in a clockwise direction, condition (a) of Eq. (6.8) holds and the point of tangency between the radial line and the curve f corresponds to a maximum ρ_θ as shown in Fig. (6.12b).

The above analysis is valid for the specimens of polar height in the range of approximately 35 to 85 mm ($0.5 < H/a < 1.2$). Beyond this range, the meridional slopes of the shell vary in a different manner as shown

in Fig. (6.13). This figure suggests at least three different modes of deformation in the bulge test. At small deformations (up to stage b), ρ_θ is always monotonically decreasing and the location of maximum ρ_θ appears to be at the pole of the bulge. For larger deformation (stage b to f), the point of tangency defined in Fig. (6.12a) shifts towards the die edge as the specimen deforms further in general, showing that the ring of maximum ρ_θ expands with deformation. When (H/a) exceeds 1.2 (stage g to l), however, due to the radial expansion there is a turning point on the ρ_θ distribution curve at the angle of 90°. Before the cusp is reached ρ_θ is monotonically increasing; and afterwards, it becomes almost constant (see Fig. 6.13).

It is also interesting to note that from curve g to l, the specimen is formed into a shell of higher curvature, but the deformation is increasingly concentrated near the pole. As explained in section (6.4.3), the deformation of the bulged specimen up to stage l is controlled by supplying or shutting the supply of the nitrogen gas, and the bulge ceases to grown once the gas supply is stopped. Above this region, the forming process is unstable, and the bulge grows by itself even after the gas supply is turned off. The radius of curvature then decreases sharply just near the pole until it fractures.

6.5.2 Determination of ρ_s in the bulge test

The radius of curvature in meridional direction (ρ_s) may be obtained by measuring the slope of the curves in Fig. (6.11). Since

$$\rho_s = \frac{dr}{d(\sin\theta)}$$

In practice, however, it is difficult to determine accurately the slope in Fig. (6.11) for any particular value of r, because the curves are all nearly straight lines passing through the origin. It is more practicable to derive the value of ρ_s from Fig. (6.13). Thus, combining Eq. (6.7) with the definition of the index of sphericality (N), we get

$$\rho_s = \frac{\rho_\theta}{1 - \sin\theta \frac{d\rho_\theta}{dr}} \qquad (6.9)$$

Although the graphical differentiation in Fig. (6.11) and that in Fig. (6.13) both involve finding the slope of curves drawn through experimental points, it is in practice considerably easier to manipulate the adjustable set square in Fig. (6.13) than in Fig. (6.11) to coincide with the tangent at any chosen point on the curve. Neither of these methods, however, can be applied for the final stages of deformation, because of the sharp turning point on the curves near the rim of the bulge.

Since the values of the slopes at these regions cannot be decided from either of the graphs, it is advisable to determine the value of ρ_s from Eq. (3.9) by differentiating the r against θ curve graphically by an adjustable set square in Fig. (6.14).

The ρ_s distribution curve can now be obtained by considering its definition in conjunction with Eq. (6.7). Thus from

$$\rho_s = \frac{dr}{\cos\theta \, d\theta} \quad \text{and} \quad N = 1 - \sin\theta \, \frac{d\rho_\theta}{dr}$$

we have

$$\rho_s = \rho_\theta + \tan\theta \, \frac{d\rho_\theta}{d\theta} \tag{6.10}$$

ρ_s and ρ_θ are always positive quantities, but $\tan\theta$ and $\frac{d\rho_\theta}{d\theta}$ can take both positive and negative values depending on the stage of deformation.

It has been shown in the previous section that there are three different modes of deformation in the bulge test of superplastic materials. The ρ_s distribution curve can be observed as a result of the variation of $\tan\theta$ and $\frac{d\rho_\theta}{d\theta}$ in each mode of deformation.

By referring to Fig. (6.15), it is observed that in the first mode of deformation (up to stage b, $H/a < 0.5$),

$\frac{d\rho_\theta}{d\theta}$ is always negative, and $\tan\theta$ is positive so that $\rho_s < \rho_\theta$ meaning a decreasing function of the ρ_s curve over the entire region θ. For the second mode (stage b to f - $0.5 < {}^{H}/_{a} < 1.2$), $\tan\theta$ is also always positive, and the sign of the term $\frac{d\rho_\theta}{d\theta}$ is the sole factor determining the relative magnitudes of ρ_s and ρ_θ. When $\frac{d\rho_\theta}{d\theta} > o$ over a region θ, Eq. (6.10) suggests that $\rho_s > \rho_\theta$; and by similar argument $\rho_s < \rho_\theta$ over the region θ where $\frac{d\rho_\theta}{d\theta} < o$. For the special case of a local sphere, Eq. (6.10) shows that the ρ_θ and ρ_s curves intersect at the position where $\frac{d\rho_\theta}{d\theta} = o$. Finally, in the third mode of deformation (stage g to 1 - ${}^{H}/_{a} > 1.2$), $\frac{d\rho_\theta}{d\theta}$ is always positive, and $\tan\theta$ determines the relative magnitude of ρ_s and ρ_θ. When $\theta < 90^{o}$, Eq. (6.10) shows that $\rho_s > \rho_\theta$; and similarly, $\rho_s < \rho_\theta$; over the region $\theta > 90^{o}$. When $\theta = 90^{o}$, however, the magnitude of ρ_s must be decided by interpolation of ρ_s distribution curve. The effect of ρ_θ on ρ_s for three modes of deformation is shown in Fig. (6.16).

6.5.3 Prolateness of the bulged specimen

It has been shown earlier that the shape of any surface is defined by an index of sphericality (N). In order to provide a clear picture of the N distribution in the actual test specimen, it is necessary to analyse the variation of N with respect to the curvature ρ_θ.

At the pole of the bulged specimen, the material is subjected to balanced biaxial stretching and N is obviously unity. Then $\frac{d\rho_\theta}{dr}$ can take any value including zero, and the shape of the ρ_θ curve within the neighbourhood of the pole can be anything continuous. At the edge of the bulge, the circumferential strain is either zero, or slightly compressive (if there is draw-in), hence the meridional tangential stress must be at least twice the circumferential stress, and the N value must therefore, be greater than one but smaller than two.

For the general case that ρ_θ is a non-linear function of r, ρ_θ can either have or not have a turning point. When a turning point does not exist and with $\theta > o$, Eq. (6.7) suggest that for monotonically increasing ρ_θ the entire surface is always prolate and for monotonically decreasing ρ_θ it is always oblate.

By virtue of Eq. (6.7), the N value corresponding to the condition $\frac{d\rho_\theta}{dr} = o$ is

$$N = 1 \quad , \quad \theta > o \qquad (6.11)$$

and the turning point of N can be obtained by the differential co-efficient of Eq. (6.7)

$$\frac{dN}{d\theta} = - \frac{d\rho_\theta}{dr} \cos\theta - \sin\theta \frac{d}{d\theta} \left(\frac{d\rho_\theta}{dr}\right) \qquad (6.12)$$

and on equating Eq. (6.12) to zero yields the condition

$$\frac{d\rho_\theta}{dr} = - \tan\theta \ \frac{d}{d\theta} \ (\frac{d\rho_\theta}{dr}) \qquad (6.13)$$

and, the magnitude of N at the turning point θ is

$$N_{(T)} = 1 + \sin\theta_{(T)} \ \tan\theta_{(T)} \ \frac{d}{d\theta} \ (\frac{d\rho_\theta}{dr})_{(T)}$$

The shape of the N distribution curve can now be predicted for a given ρ_θ distribution curve in conjunction with the mechanical constraints at the pole and die edge. Two simple cases of monotonically increasing and monotonically decreasing functions of ρ_θ have already been discussed in the previous paragraph. Since N = 1 at $\theta > o$ corresponds to $\frac{d\rho_\theta}{dr} = o$ (Eq. 6.11), the N curve must cross the line of N = 1 for a non-linear ρ_θ curve with turning point(s). Obviously, for a ρ_θ curve with one turning point, the N curve must cross the N = 1 line only once, and it must have either a minimum with $N_{(T)} < 1$ at maximum ρ_θ, or maximum with $N_{(T)} > 1$ at minimum ρ_θ. On the other hand, for two crossings, the simplest N curve is maximum $N_{(T)}$ ($N_{(T)} > 1$) initially and becomes a minimum ($N_{(T)} < 1$) towards the die edge and the corresponding ρ_θ curve has a minimum initially, followed by a maximum value towards the die edge. Similar deductions may be made for the multiple intersection of N with the line of N = 1. Fig. (6.17) is an attempt to summarise the

possible N and ρ_θ curves in their simplest forms.

From the above analysis, it can be seen that the bulge along the entire meridian section can either be oblate or a combination of prolate, oblate and spherical shapes. The prolateness of a deformed bulge can also be visualised from the basic curves shown in Fig. (6.11). The method of analysis is similar to that for circumferential curvature variations shown in Figs. (6.12a and b). By virtue of Eqs. (6.6) and (6.8), the surface is oblate over the region where the basic curve intersects the radial lines in the clockwise direction. A prolate surface will be revealed over the region where the basic curve crosses the radial lines in the anti-clockwise direction. Similarly, it can easily be shown that the point of tangency represents a spherical shape. This method of analysis shows that the deformed bulge consists of a sphere at the pole and a spherical ring whose diameter keeps expanding with deformation between the pole and die edge. Between the pole and ring , the bulge is everywhere prolate, and becomes oblate in the region between the ring and the die edge.

The complex variation of prolateness and stress conditions within a real bulged specimen and throughout the forming process can be seen in Fig. (6.18). As seen in this figure, in the first mode of

deformation, the shell is always oblate; and a study of the polar heights for the second mode of deformation (stages b to f) suggests that the bulge has only one particular shape regardless of further deformation indicating the stability of the process. Thus, between curves b and f, near the rim, the prolateness actually increases (shell becomes more pointed) with the general decrease in curvature showing that curvature and prolateness are two distinct geometrical properties. During the stable deformation, the shell is divided into two zones by an annular ring of perfect spherical surface (N = 1), prolate inside and oblate outside it. In the third mode of deformation, however, a minute change in polar height will result in a large variation of shape, and as the forming progresses, the prolate expands outwards. This prolate region except near the pole, becomes more pointed; and the oblate region diminishes in size till near the end of the forming process. Consequently, the whole shell at this stage becomes prolate and the N value falls below unity (curve 1 in Fig. 6.18).

It is worth mentioning here that the same general variation of prolateness with respect to r has been found in non-superplastic bulged specimens (70, 84). In this section, an attempt is made to compare the results in Fig. (6.18) with those obtained by T.C. Hsu et. al. (70) in the bulge test for copper

specimens. These are shown in Fig. (6.19) for various values of the effective strain at the pole (ε_o) As seen in this figure, the similarity in the general shapes of the curves between two sets is remarkable. However, some differences between theirs and the present results are noticeable. At the initial stages (e.g. for $\varepsilon_o = 0.15$), the bulge is entirely oblate for superplastic material whereas they have found that the bulge is partly prolate ($N < 1$) even at the very beginning. For $\varepsilon_o > 0.8$, the non-superplastic bulge is in the unstable regime whereas the superplastic shell reaches to this stage when $\varepsilon_o > 3.2$.

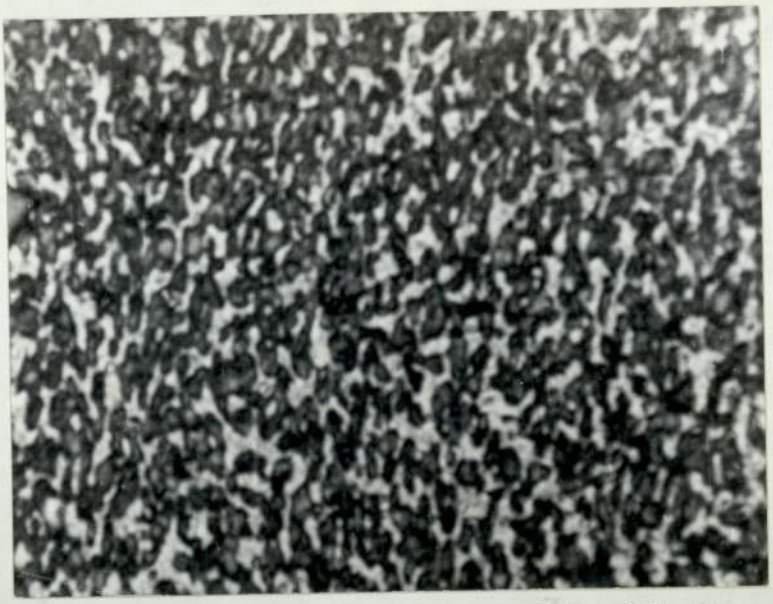

Fig.6-1-a- Optical micrograph of Zn-22 % Al eutectoid alloy showing microstructure Prior to testing ; average grain size $L < 1\,\mu m$; magnification 2650 times .

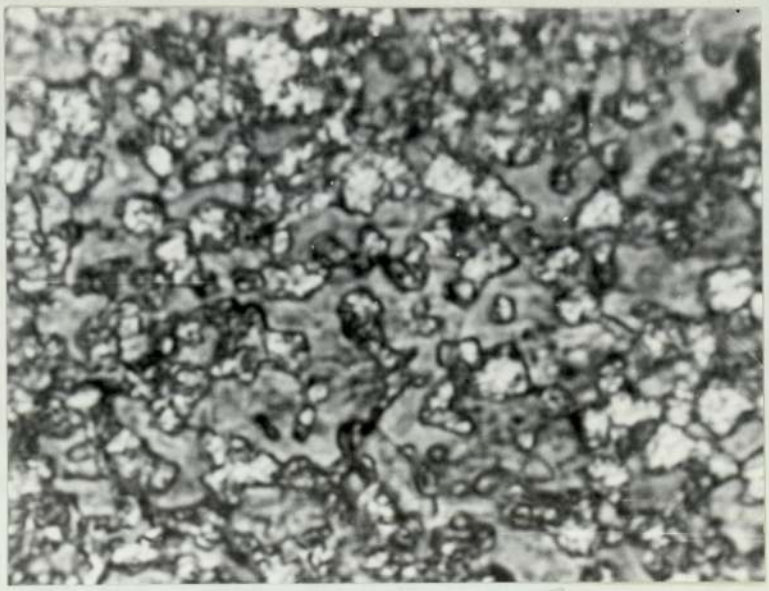

Fig.6-1-b- Optical micrograph of Zn-22 % Al eutectoid alloy showing microstructure after aging for 48 hr at 270°C; average grain size $L < 3\,\mu m$; magnification 2650 times.

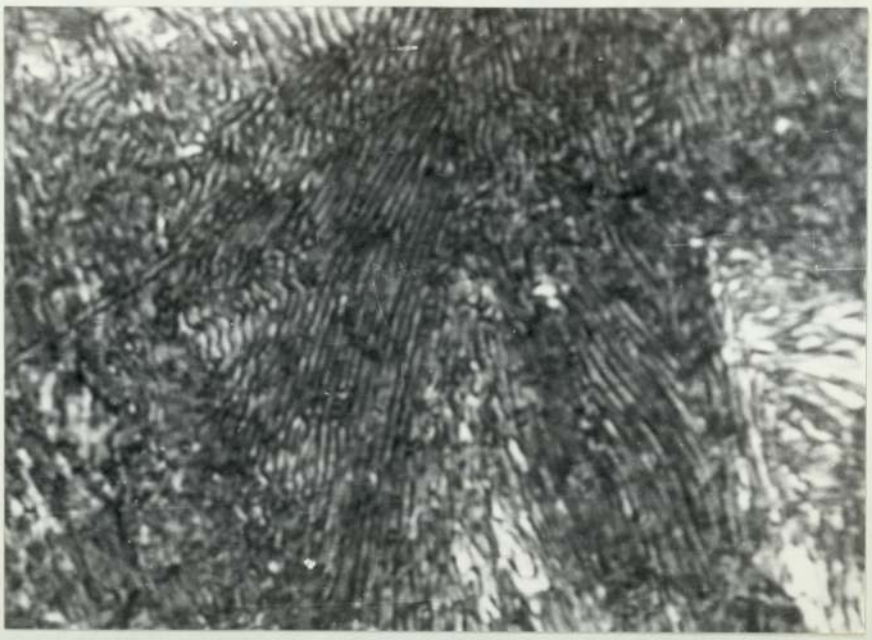

Fig. 6.2 – Optical micrograph showing a typical lamellar structure of Zn–Al eutectoid alloy ; the specimen was held at 300°C for 1 hr and furnace cooled ; magnification 2650 times .

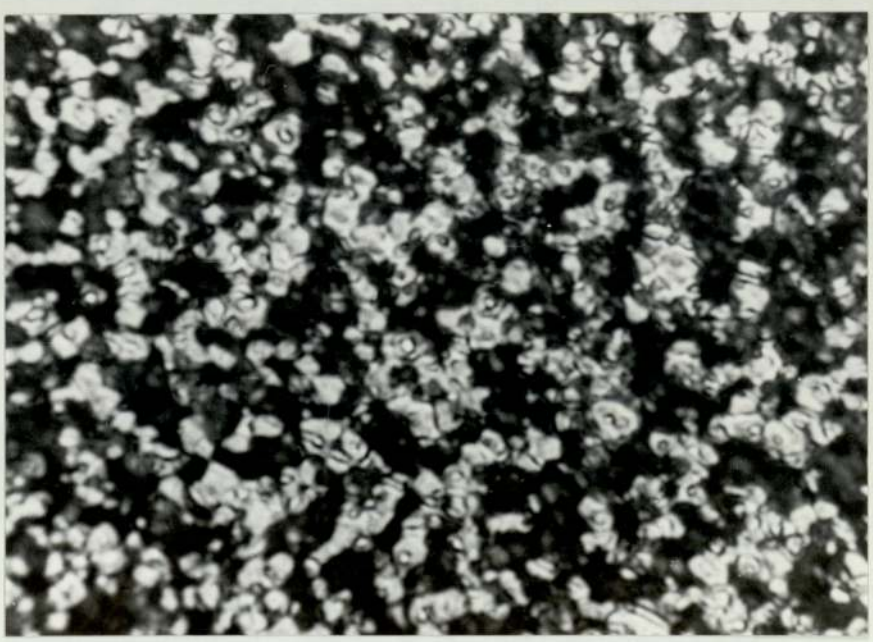

Fig. 6.3 – Optical micrograph showing the structure of the bulged specimen near fractured region at 270°C; magnification 2650 times .

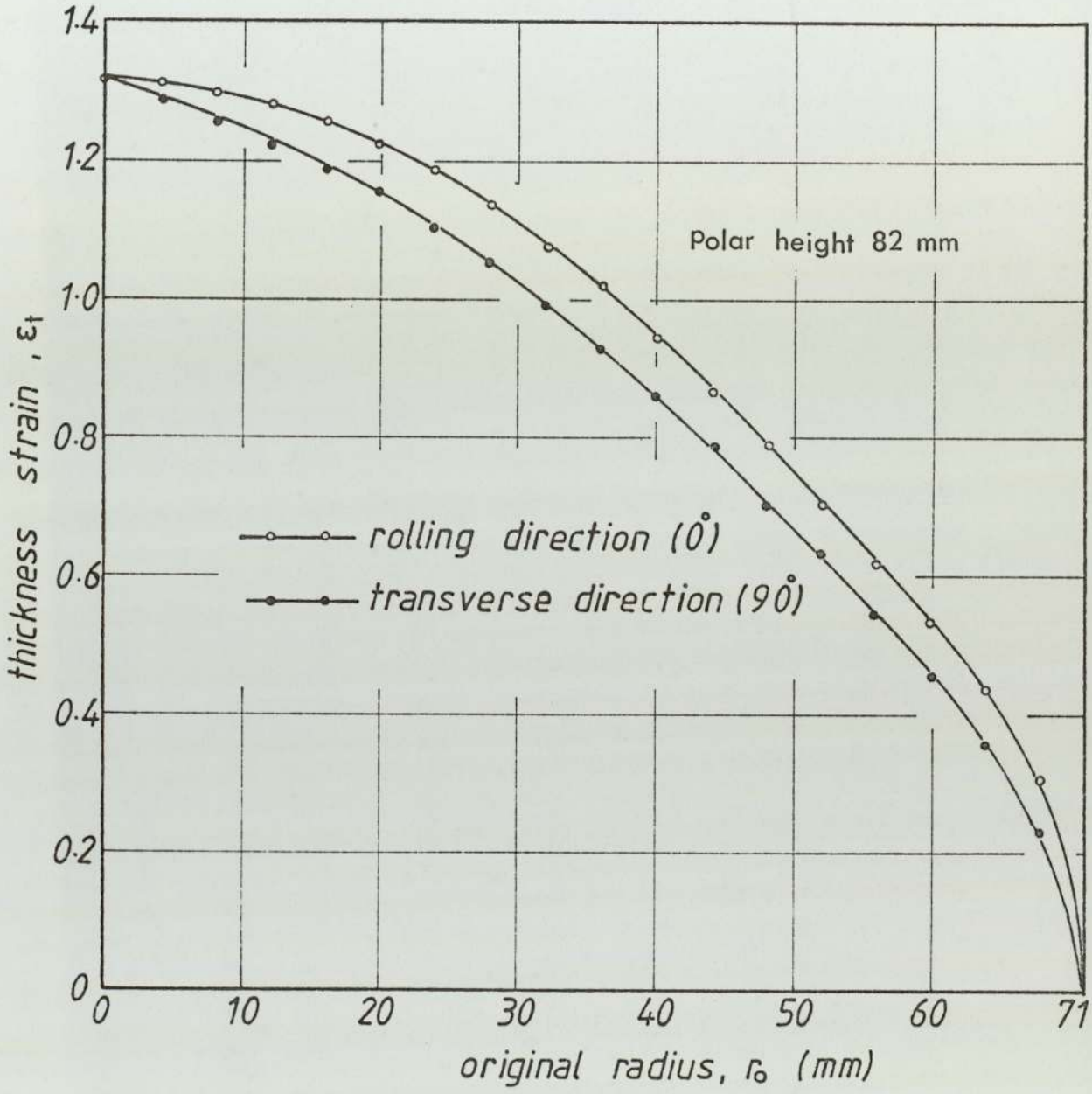

Fig. 6-4 – Anisotropy effect in the bulge test .

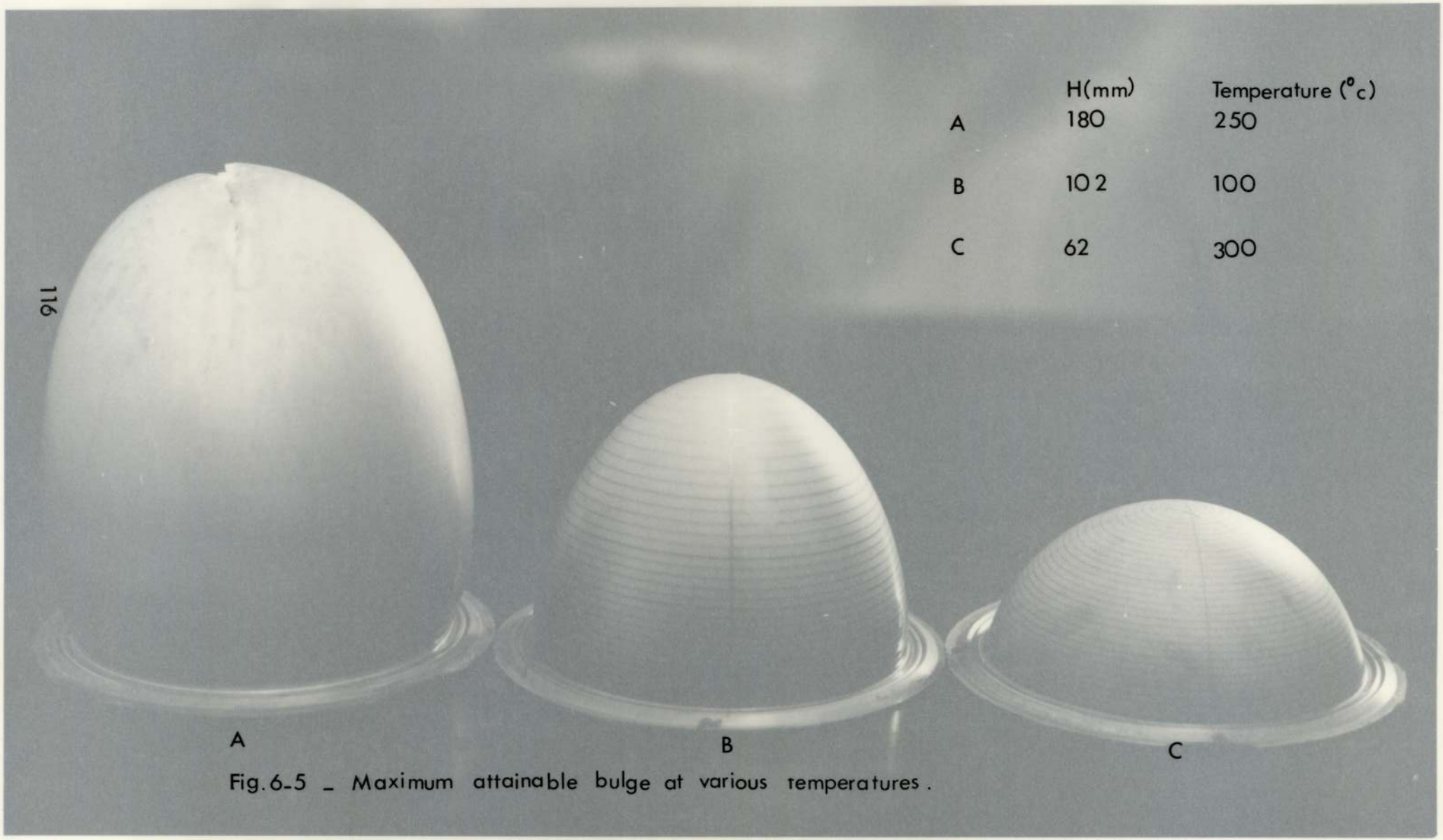

Fig. 6-5 _ Maximum attainable bulge at various temperatures.

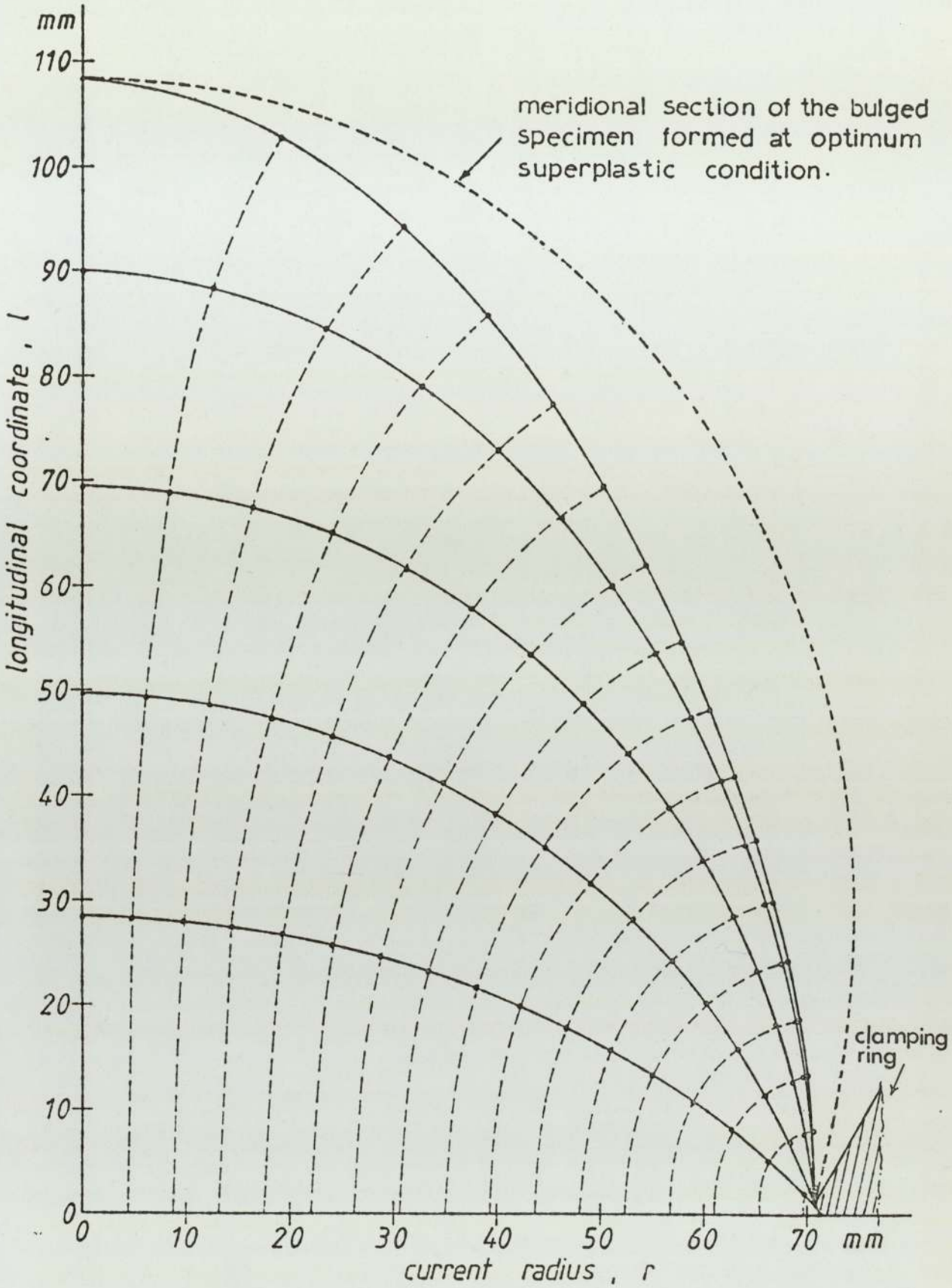

Fig. 6.6 – The meridional sections and particle trajectories of the specimen formed at low temperature, (100°c).

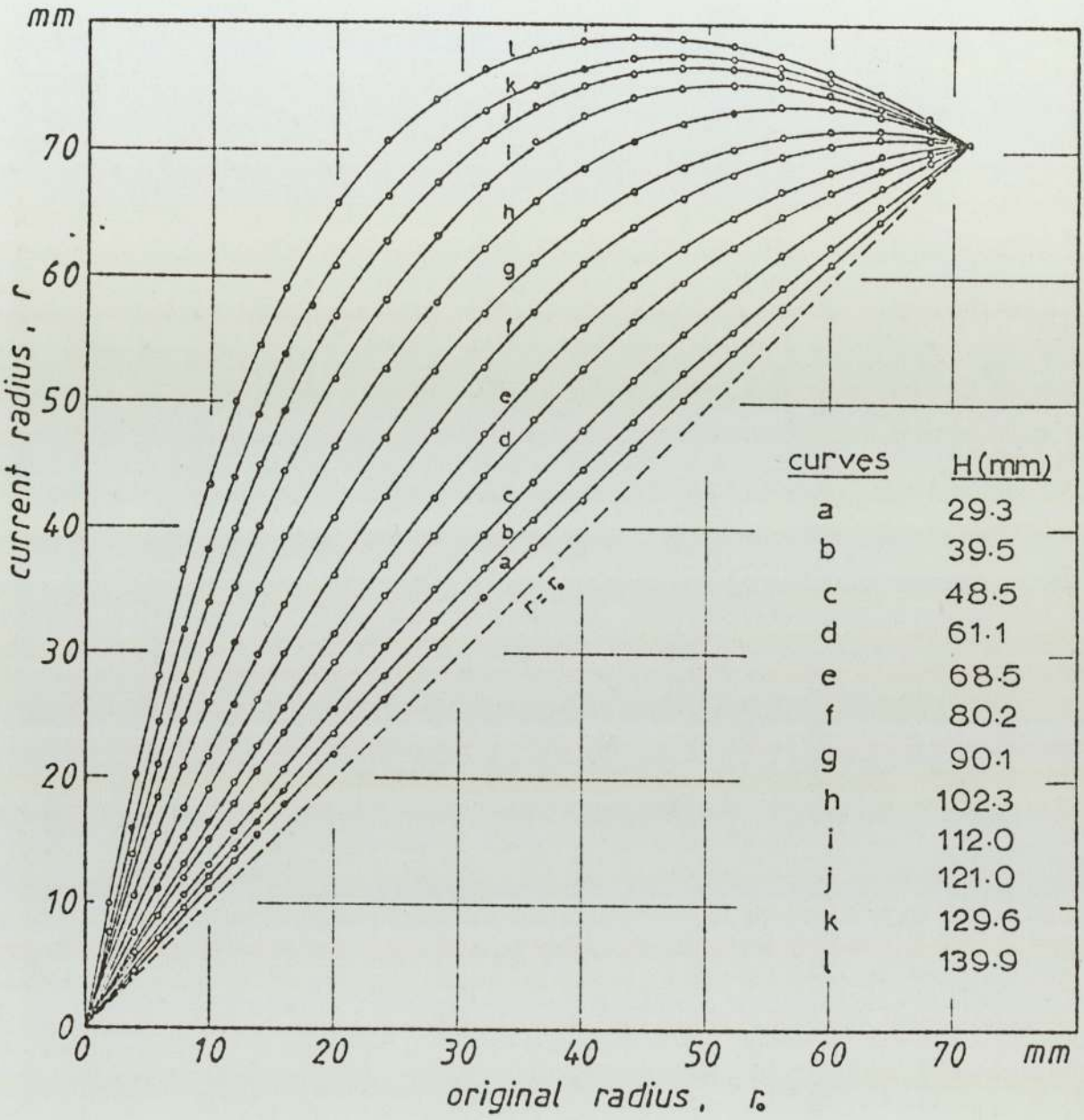

Fig. 6-7 - Radial movements of the material particles during successive stages of deformation.

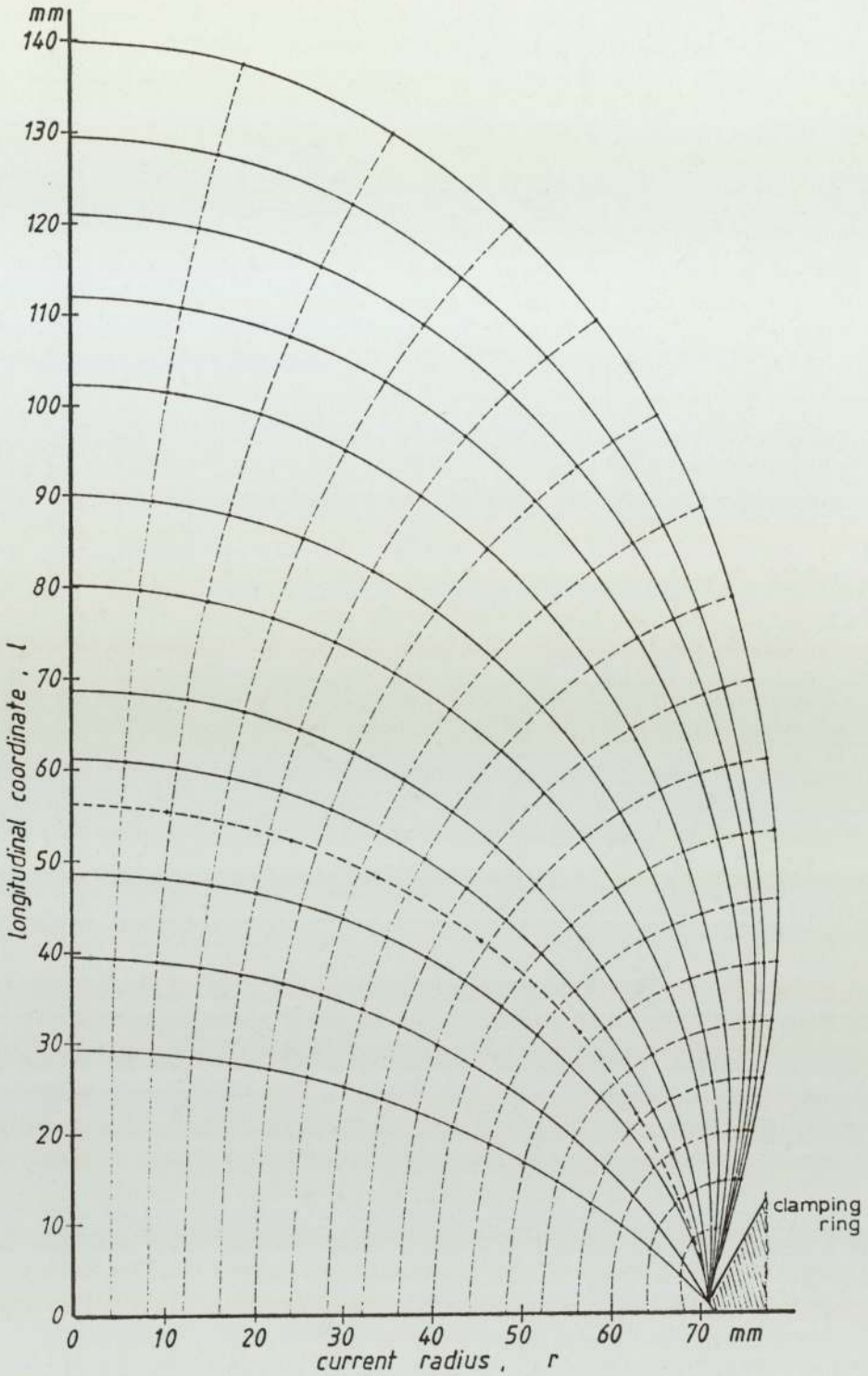

Fig. 6-8 – Meridional sections and particle paths at optimum superplastic conditions.

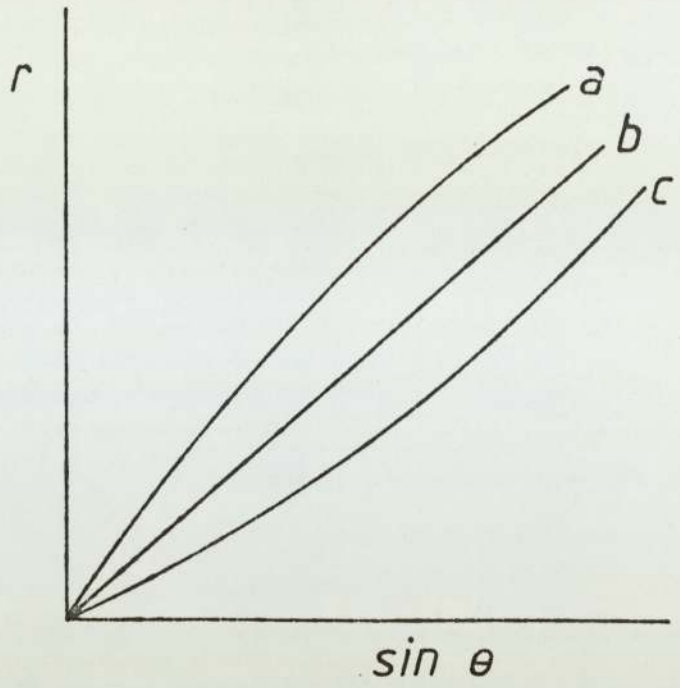

a : oblate

b : spherical

c : prolate

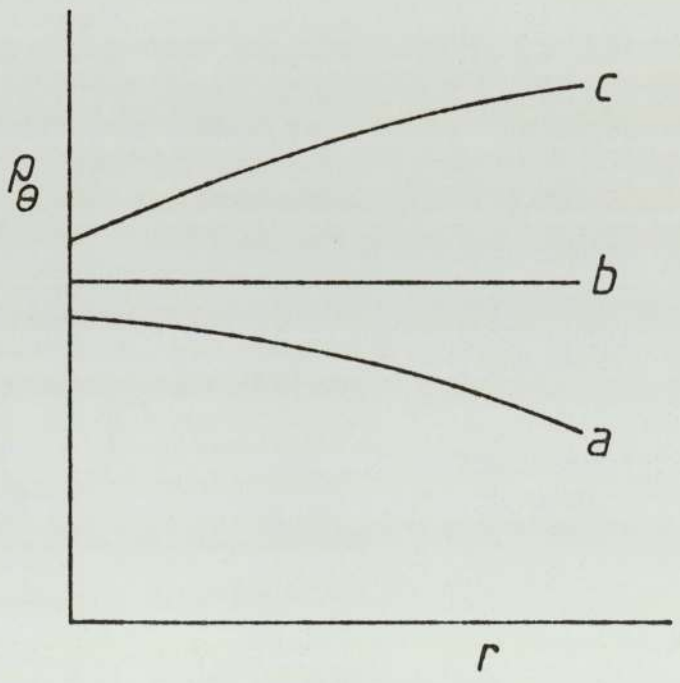

Fig. 6-9 – Relationship of profile slope with curvature in the circumferential direction.

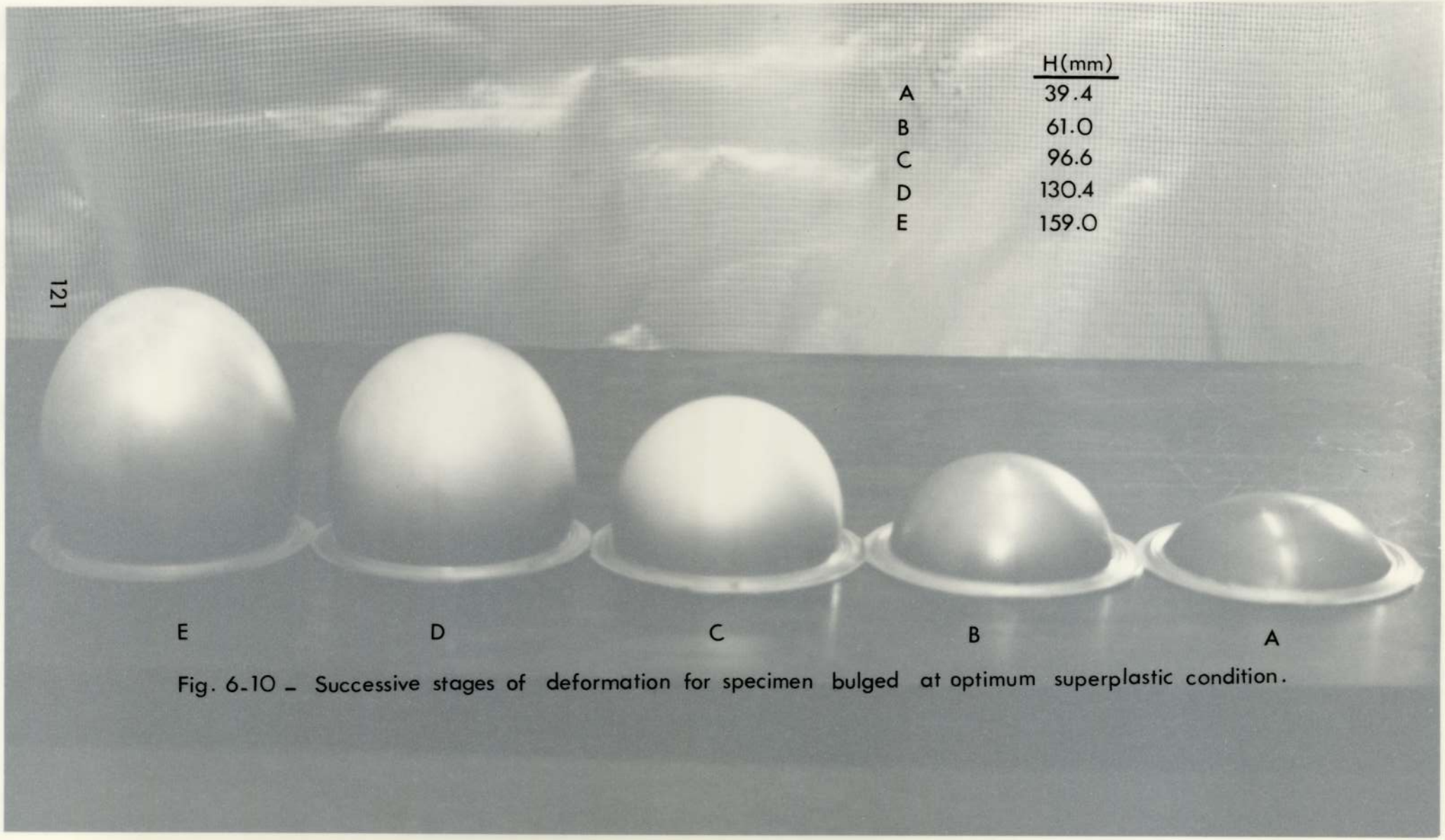

Fig. 6-10 – Successive stages of deformation for specimen bulged at optimum superplastic condition.

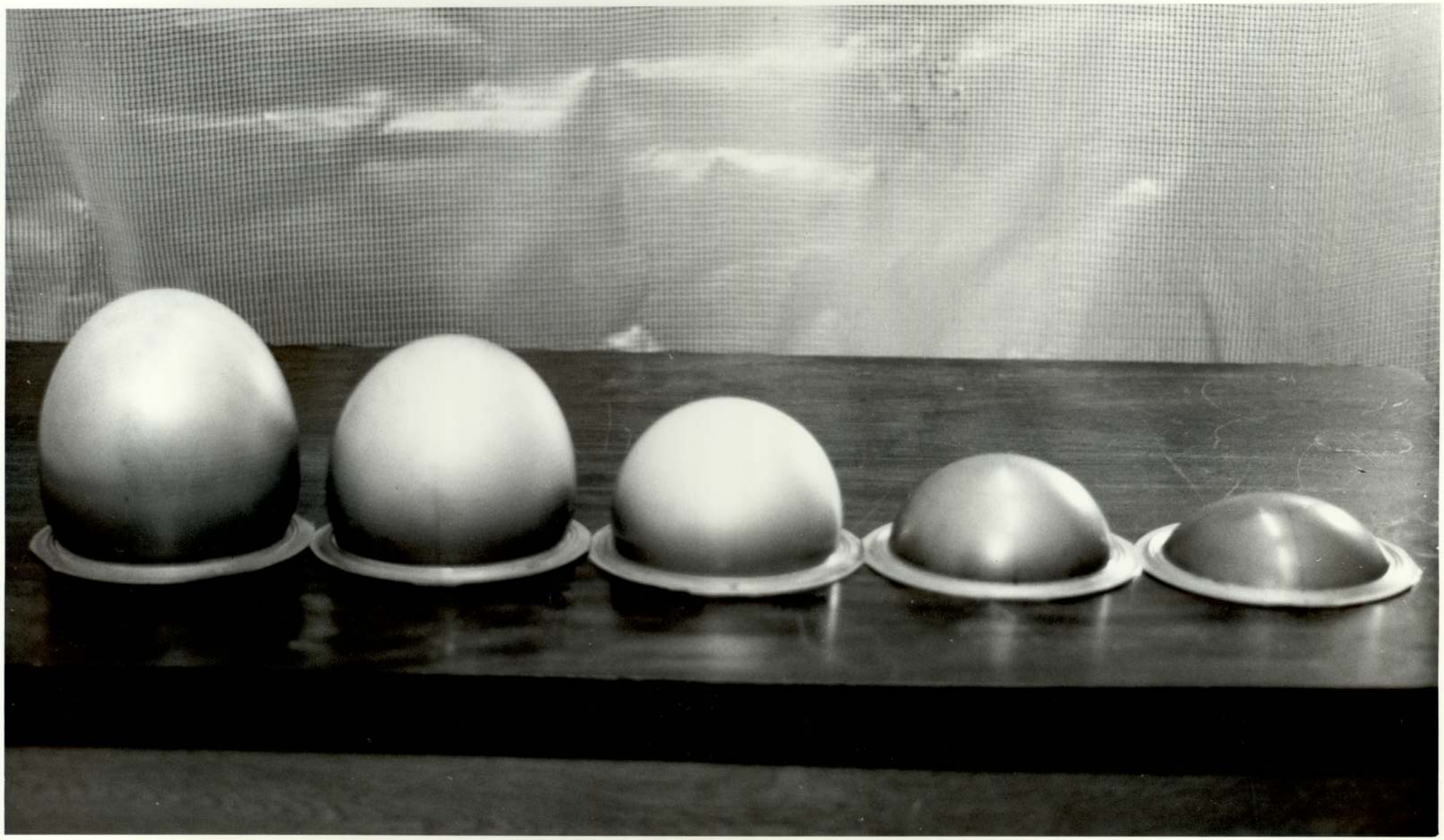

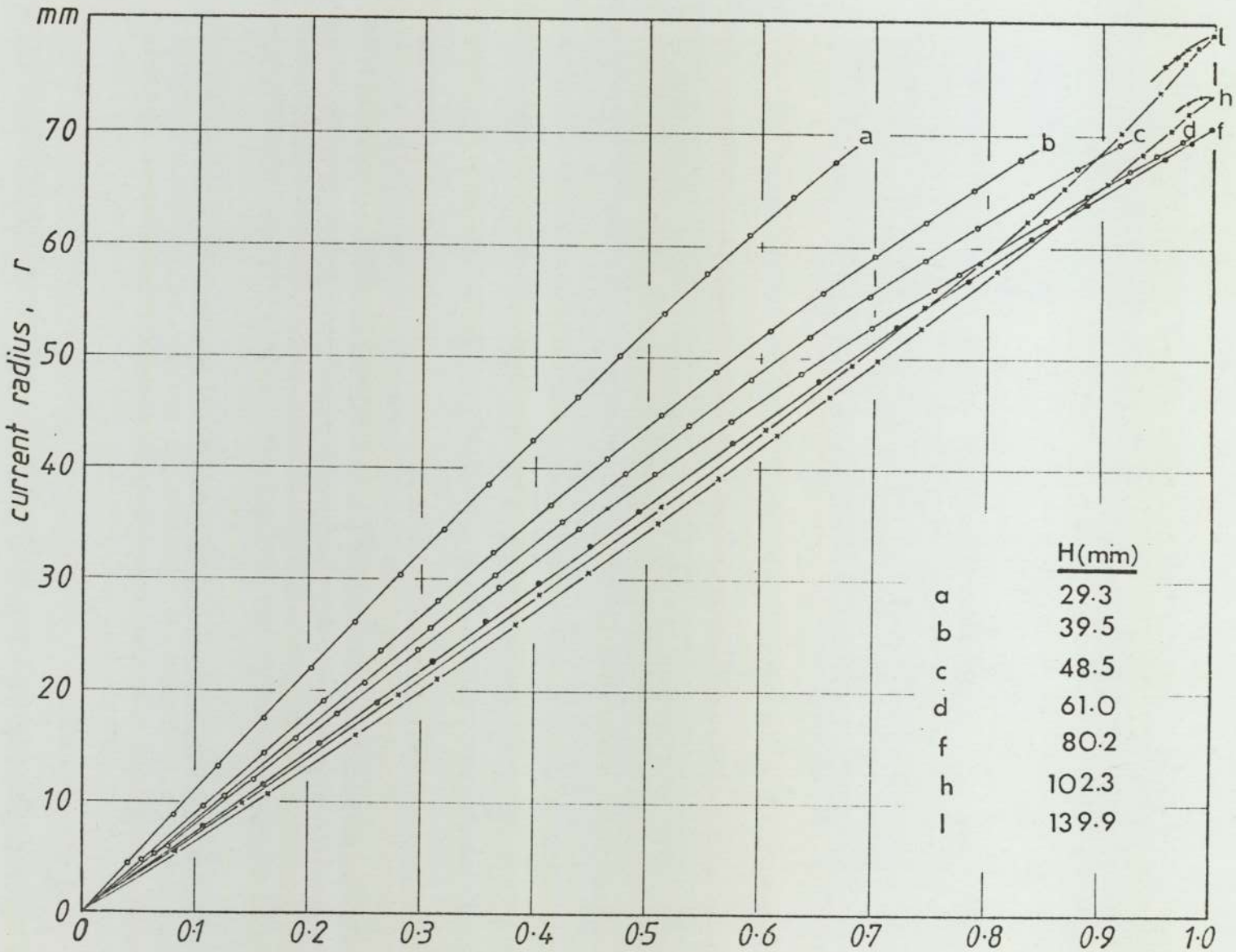

Fig. 6-11 – Radial distance vs. meridional slope.

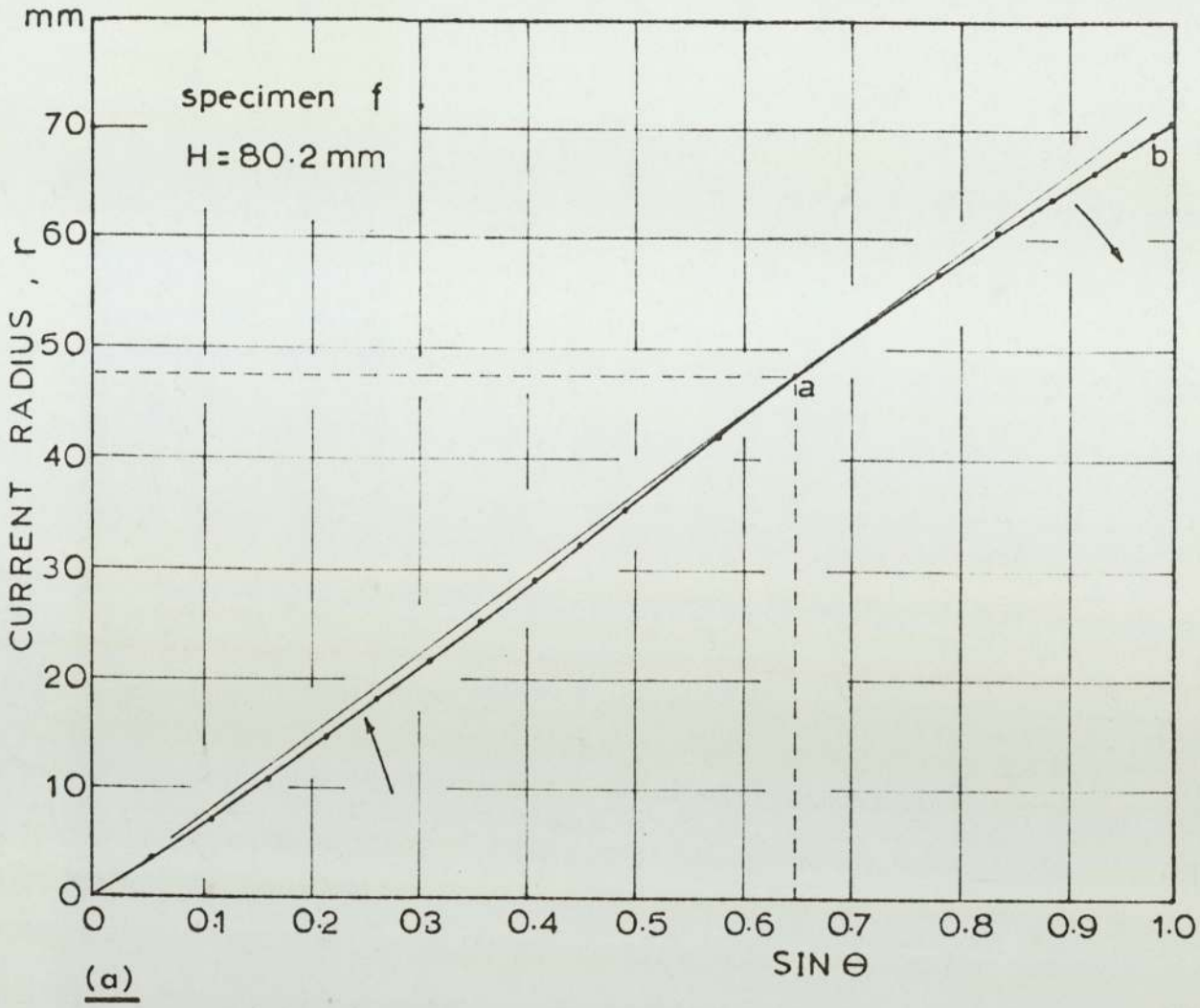

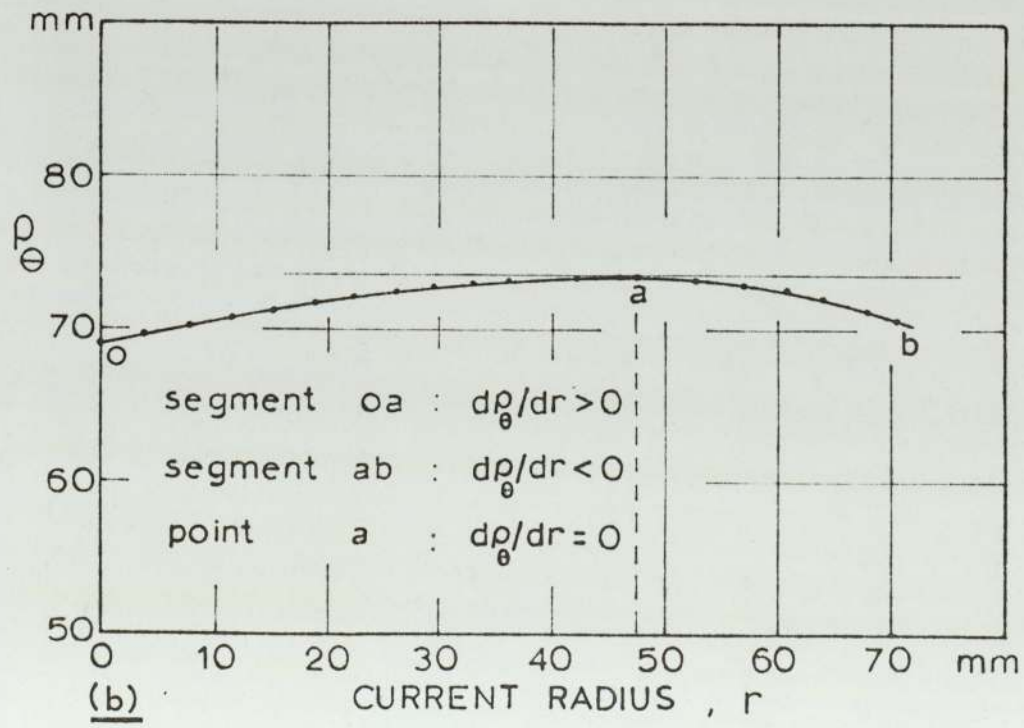

Fig. 6_12 _ Identification of circumferential curvature variations.

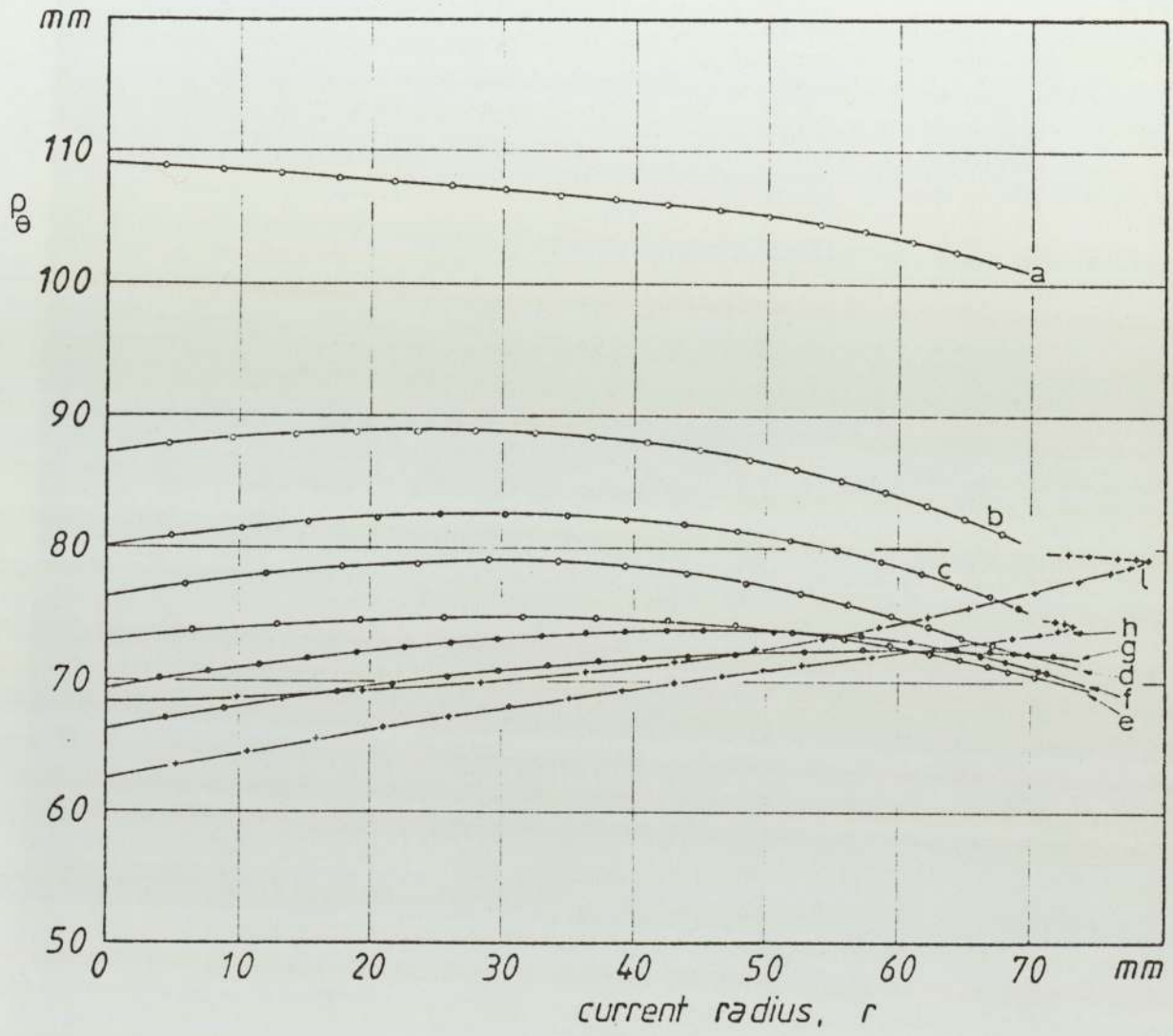

Fig. 6-13 - Radial distance vs. circumferentail radius of curvature.

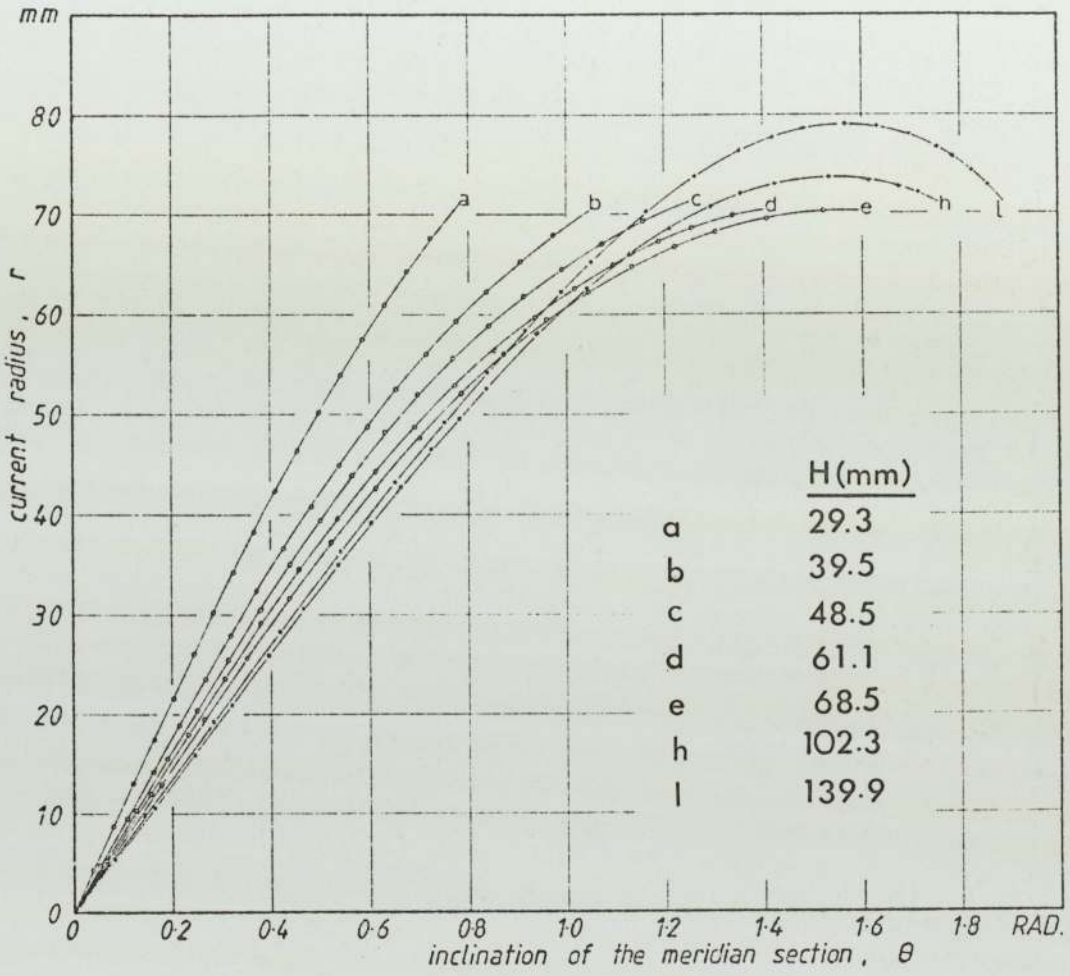

Fig. 6_14 – Radial distance vs. inclination of the meridian section.

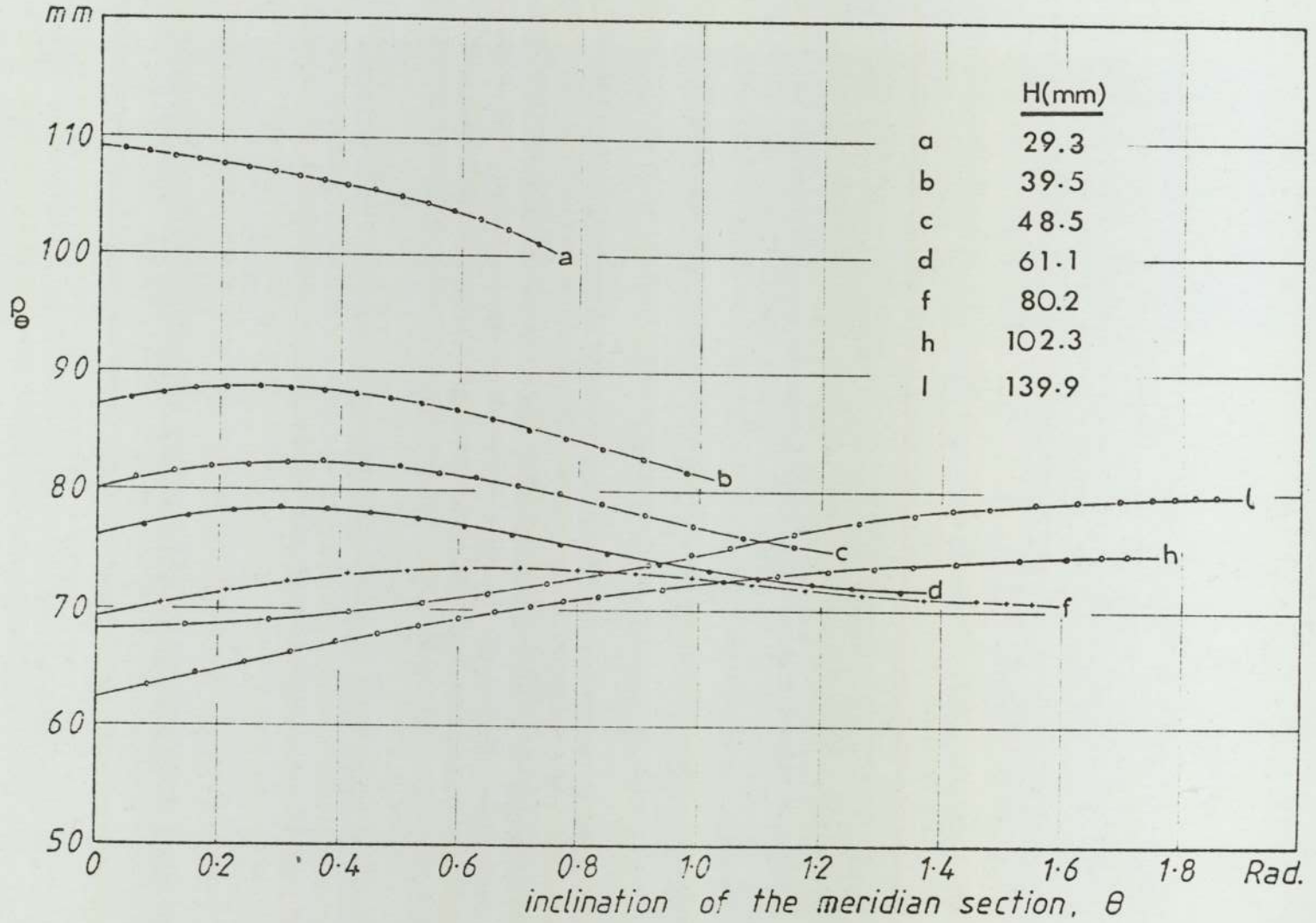

Fig. 6_15_ Circumferential radius of curvature vs. inclination of the meridian section.

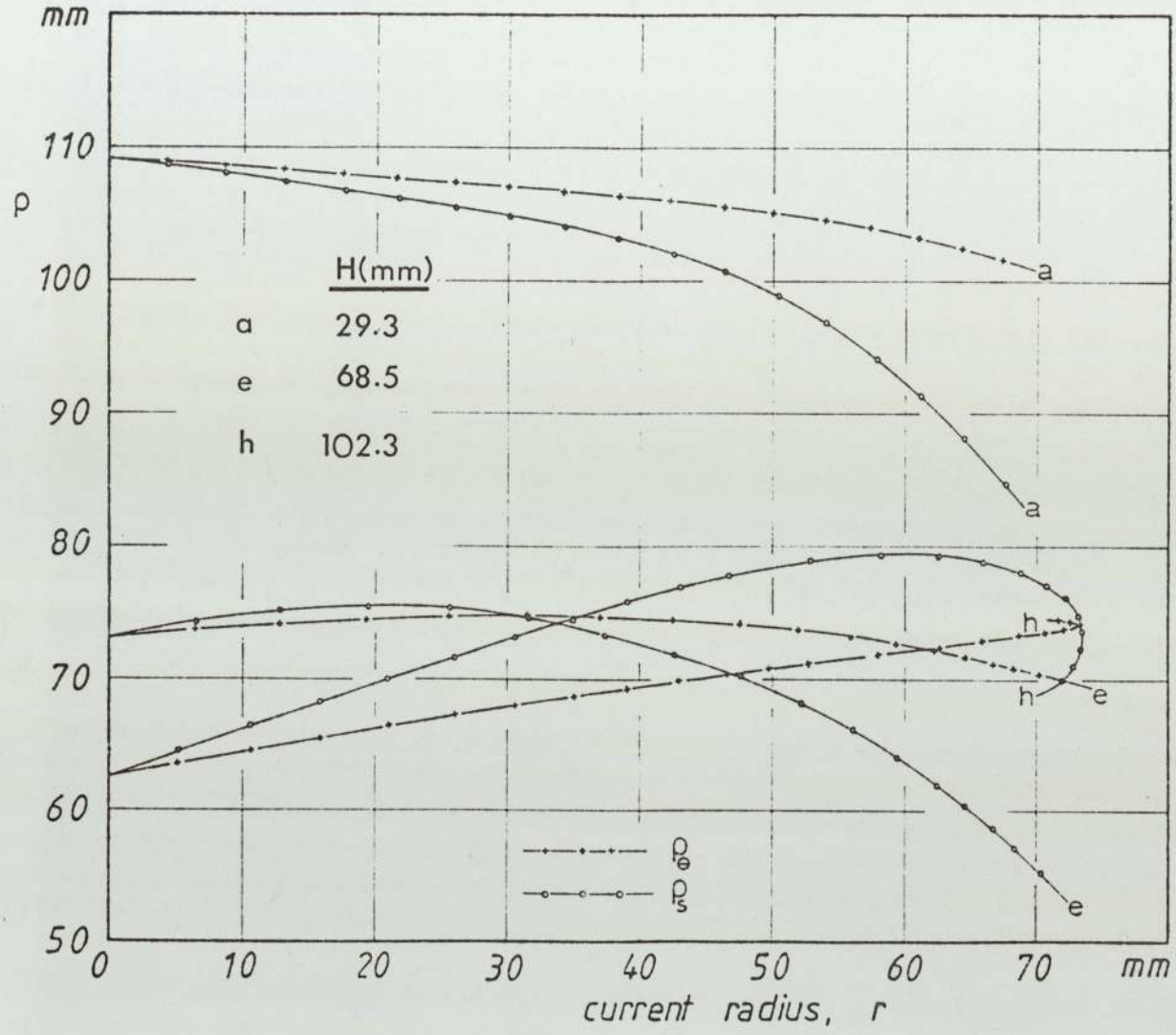

Fig. 6-16 - Effect of circumferential radius of curvature on the meridional radius of curvature.

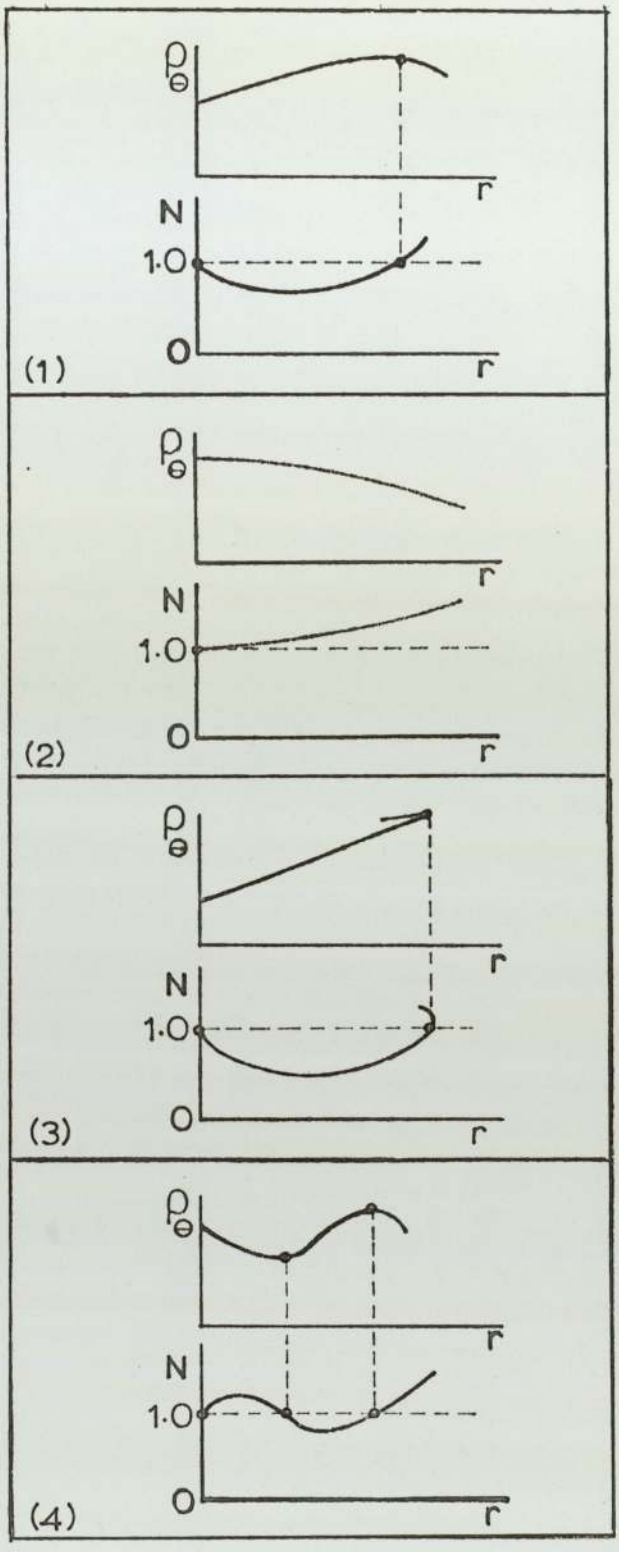

Fig. 6-17 – Theoretical investigation of N-value in a workpiece.

1– maximum ρ_θ

2– monotonic decreasing ρ_θ

3– maximum ρ_θ with a cusp

4– minimum & maximum ρ_θ

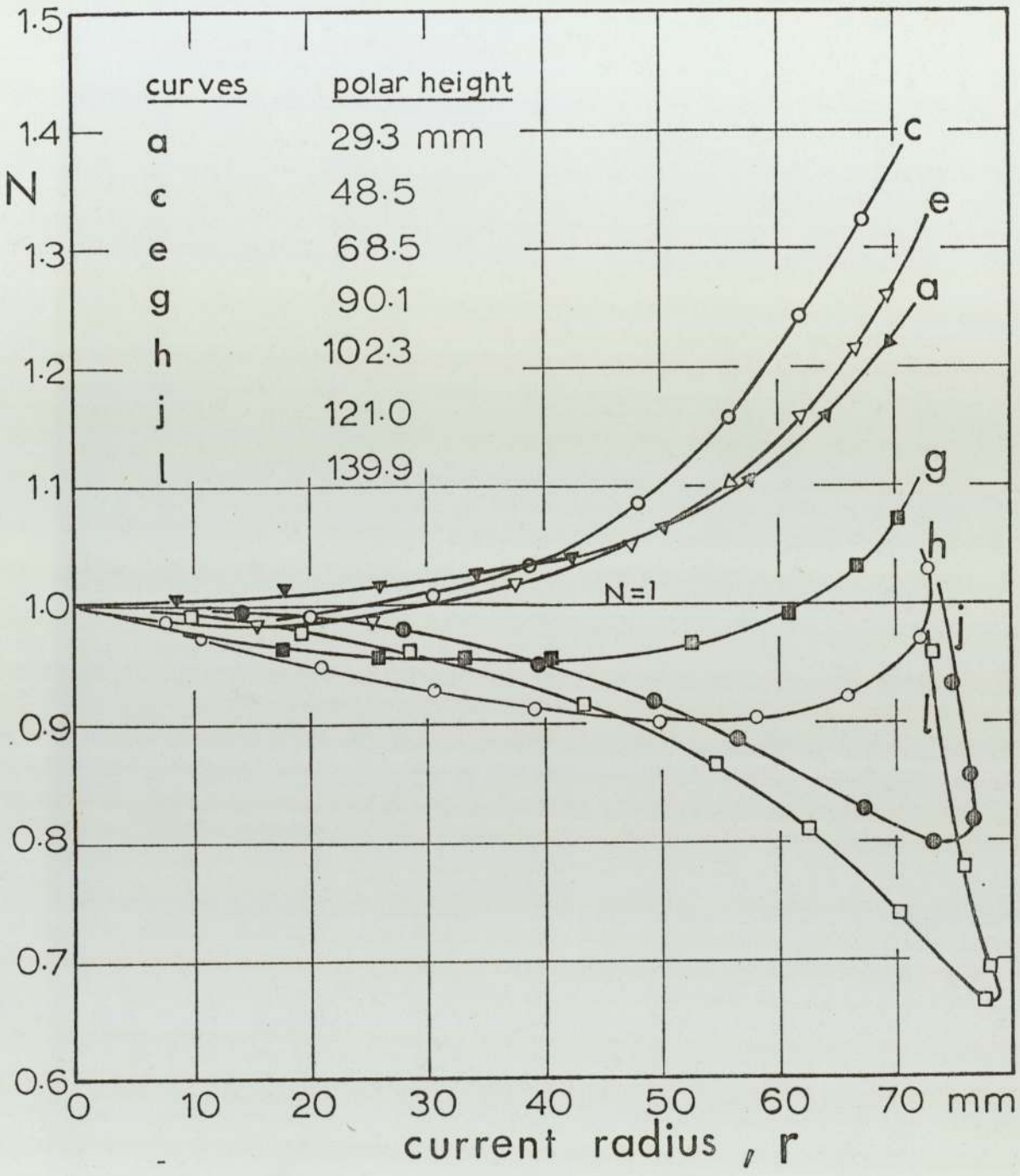

Fig. 6-18 – prolateness in the bulged specimen.

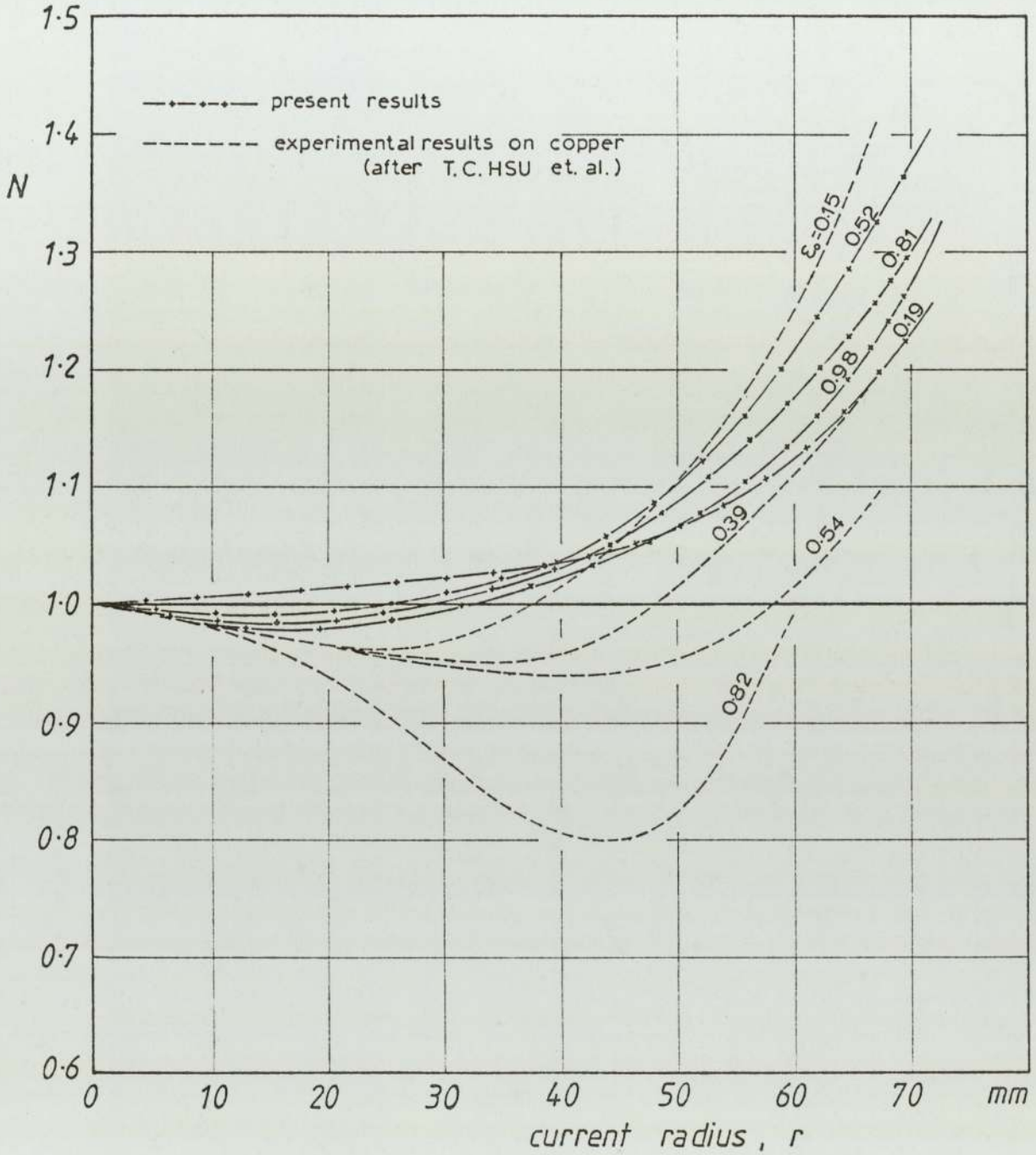

Fig. 6-19 – Comparison of prolateness between superplastic zn–22% al and copper specimens.

CHAPTER 7

FLOW STRESSES IN THE BULGE TEST

Chapter 7

7.1 Forces involved in the bulge test

It has been clearly shown in section (6.5.3) that the N value varies widely along the bulge profile, and is locally a sphere only at the pole and at an annular ring whose position shifts towards the die edge as deformation progresses. At everywhere before this annular ring is reached from the pole, the shell is prolate and becomes oblate after this ring is passed, Fig. (6.18). From the variation of the N values, it is possible to analyse the variation of the forces in the deformed shell for any particular stage of deformation. For the present analysis the second mode of deformation (stage b to f - $0.5 < {}^{H}/_{a} < 1.2$) is chosen as it represents a typical deformation in the bulge test. This analytical approach is also applicable to both the first and third modes of deformations.

As seen in section (3.2), there are two forces involved in the bulge test, namely ($\sigma_\theta t$) the force per unit length of the meridian section, and ($\sigma_s t$) the force per unit length of the circumferential section. The variation of these forces will be discussed in turn.

7.1.1 Meridional tension

The variation of the meridional tension may be

obtained by differentiating Eq. (3.5) with respect to r , hence

$$\frac{d(\sigma_s t)}{dr} = \frac{P}{2} \frac{d\rho_\theta}{dr} \qquad (7.1)$$

since the pressure (P) is constant, then comparison of Eqs. (6.8) and (7.1) yields,

$$\text{a) if } \frac{d\rho_\theta}{dr} > o \text{ then } \frac{d(\sigma_s t)}{dr} > o \text{ and } N < 1$$

$$\text{b) if } \frac{d\rho_\theta}{dr} = o \text{ then } \frac{d(\sigma_s t)}{dr} = o \text{ and } N = 1 \qquad (7.2)$$

$$\text{c) if } \frac{d\rho_\theta}{dr} < o \text{ then } \frac{d(\sigma_s t)}{dr} < o \text{ and } N > 1$$

By virtue of Eq. (7.2), in the region of prolateness (N<1), $\frac{d\rho_\theta}{dr}$ is always positive and the meridional tension is monotonically increasing, (Path ABC in Fig. 7.1). The annular region of unity N, corresponds to the maximum meridional force ($\frac{d(\sigma_s t)}{dr} = o$), Point C in Fig. (7.1), and when this point is passed $\frac{d(\sigma_s t)}{dr}$ becomes negative. Therefore, for successive deformations, a locus for $\frac{d(\sigma_s t)}{dr} = o$ representing maximum meridional force can be drawn. From the N distribution curve shown in Fig. (7.1), it is easy to visualise two separate features in the region to the left of the maximum ($\sigma_s t$) locus. These features are characterised by the minima of N. Thus, in spite of the property of N < 1 in this region, $\frac{dN}{dr}$ is negative

initially and then becomes positive towards the maximum ($\sigma_s t$) locus. Therefore, for the successive stages of deformation it is possible to draw a locus passing through point B in Fig. (7.1) to indicate minimum N ($\frac{dN}{dr} = o$).

7.1.2 Circumferential tension

The variation of the circumferential tension can be obtained from Eq. (3.6), thus

$$\sigma_\theta t = (2-N)\ \sigma_s t \qquad (7.3)$$

differentiating Eq. (7.3) with respect to r yields,

$$\frac{d(\sigma_\theta t)}{dr} = (2 - N)\ \frac{d(\sigma_s t)}{dr} - (\sigma_s t)\frac{dN}{dr} \qquad (7.4)$$

It can readily be seen from Fig. (7.1) that at the position near the pole (Path AB), $\frac{d(\sigma_s t)}{dr}$ is positive and $\frac{dN}{dr}$ is negative. Hence, Eq. (7.4) requires that $\frac{d(\sigma_\theta t)}{dr} > o$, and the circumferential force must be monotonically increasing. At everywhere in the specimen after the maximum ($\sigma_s t$) locus is passed (Path CD), both meridional and circumferential forces are decreasing functions since $\frac{d(\sigma_s t)}{dr} < o$ and $\frac{dN}{dr} > o$. In the area between the two loci $\frac{d(\sigma_s t)}{dr} = o$ and $\frac{dN}{dr} = o$ (Path BC), the circumferential force

becomes monotonically decreasing although the meridional tension is still increasing.

These three distinctive properties of AB, BC and CD in Fig. (7.1) may also be obtained by plotting ($\sigma_\theta t$) against ($\sigma_s t$) in Cartesian coordinates. These curves are shown in Fig. (7.2) with the line of 45 degrees, representing equal forces with unity N. The direction of the curves from the starting point on the line of 45° has a definite meaning. Along the line of 45 degrees, N is equal to one, and the forces are balanced biaxial stretching forces, (point A and C). Above this line, N is less than unity, the shape of the shell is prolate, and the circumferential force exceeds the meridional tangential (Path ABC); and below this line, N is greater than unity, the shape of the shell is oblate, and the relative magnitudes of the forces are reversed (Path CD). Therefore, all the curves take a spiral shape in the clockwise direction towards the die edge except those for the initial and final stages of deformation. It is evident that the curves for the initial stages of deformation must lie below the line of 45° , since the shells are totally oblate (e.g. curve a, in Fig. 7.2).

Some features of the forces per unit sectional length are noticeable in Fig. (7.2). Point B is the position r in the specimen where the resultant force

is maximum and this corresponds to a point having passed the minimum N value with N still less than unity but its gradient $\frac{dN}{dr}$ becomes positive. When the curves in Fig. (7.2) intersect the line of 45 degrees (N = 1) at C, the local surface is temporarily a sphere, and it can easily be shown that ρ_θ is maximum and the tangent at C in Fig. (7.2) then becomes vertical, giving $\frac{d(\sigma_s t)}{dr} = o$. The locus of this point (C) for successive stages is then represented by a horizontal line N = 1 and the $\frac{d(\sigma_s t)}{dr} = o$ locus in Fig. (7.1).

It can be seen from Fig. (7.2) that the position vector at point B has always a maximum value. Therefore, the locus of this point for successive stages represents the locus of the maximum resultant force which occurs only in the second mode of deformation ($0.5 < {}^{H}/_{a} < 1.2$), at $18 < r < 30$ mm.

The fact that the maximum resultant force does not occur at the pole can be explained by the following analysis.

Let F be the resultant force. By vector algebra

$$F^2 = (\sigma_\theta t)^2 + (\sigma_s t)^2 \qquad (7.5)$$

by substituting Eq. (7.3) into Eq. (7.5)

$$F^2 = (\sigma_s t)^2 . (1 - (2 - N)^2) \qquad (7.6)$$

$$F^2 = (\sigma_s t)^2 . (N^2 - 4N + 5)$$

Thus
$$F = (\sigma_s t) \cdot (N^2 - 4N + 5)^{\frac{1}{2}} \qquad (7.7)$$

$$= F_1 \cdot F_2$$

where
$$F_1 = \sigma_s t$$
$$F_2 = (N^2 - 4N + 5)^{\frac{1}{2}} \qquad (7.8)$$

In Eq. (7.8), F_1 is maximum along the maximum $(\sigma_s t)$ locus and F_2 is maximum along the minimum N locus. Some reflection will show that the maximum resultant force must occur at some position between the $\frac{dN}{dr} = o$ and $\frac{d(\sigma_s t)}{dr} = o$ loci, that is between points B and C in Fig. (7.1).

A striking feature of the curves in Fig. (7.2) is the reduction of resultant forces for the successive stages of deformation which is due to the constancy of pressure (P) and decrease of the principal curvatures as the forming progresses.

7.2 Flow stresses in the bulged specimen

Having obtained the trend of the force distribution curves in the deformed shell, it is possible to pursue

towards the flow stresses. This can simply be done by taking into account the thickness (t) in Eqs. (3.5) and (3.6). Thus the stress distribution curves can be plotted as in Figs. (7.3) and (7.4). Comparison between Figs. (7.2) and (7.3) shows that in the former, the loops in the curves above the line of 45 degrees (N = 1) are all in clockwise direction, whereas in the latter they are in anticlockwise direction. This reversal is due to the effect of the variation in the thickness (Fig. 7.5). The other noticeable difference between the force and the stress curves is the radial movement of the points on the stress curve near $r = o$ relative to the rest of the curve, outwards from the origin, and each movement is greater, the greater the variation in thickness. Obviously, if the shell were always a perfect sphere, with uniform thickness distribution, each stress distribution curve would collapse into a single point on the line for N = 1. For the actual shells, however, the stress curves cross this line only at the pole and at an annular ring which is locally a sphere. Elsewhere, the state of stresses is more complicated, because with increasing deformation, not only the magnitude of the stresses σ_θ and σ_s increases due to the thinning of the material, but the ratio between them changes also. The effect of severe thinning of material in the third mode of deformation ($^H/_a > 1.2$) on the stress distribution curves becomes conspicuous in Fig. (7.4), and at the

final stages of deformation (curves k and l), the stress curves cross the line for N = 1 only once and that is at the pole of the shell.

The intensity of triaxial stresses is measured by the effective stress which in this case is that for the Von Mises ellipses, as follows,

$$\sigma_\theta^2 - \sigma_\theta \sigma_s + \sigma_s^2 = \text{constant}$$

A series of Von Mises ellipses are plotted in Figs. (7.3) and (7.4) as guides to show that the greatest effective stress is not at the pole, except at some stages in the third mode of deformation (curves i to l). Before these stages the point of maximum effective stress remains near $r_o = 16$ mm.

This particular behaviour of the material in the biaxial test is very different from the uniaxial one in which the stress is inversely proportional to the cross-sectional area of the specimen at any particular stage, so that, the maximum stress always occurs at the thinnest section. This condition is also valid for a perfect spherical bulge with non-uniform profile thickness, but such a case can never occur experimentally in the usual test method. In the actual bulge test, because of the effects of ρ_θ and t, the maximum stress will occur at the thinnest section only when the curvature of the bulge does not affect the stress function.

The magnitude of the resultant stress follows that of the resultant force vector and the position of maximum resultant stress is between the $\frac{dN}{dr} = o$ and $\frac{d(\sigma_s t)}{dr} = o$ loci, that is between points B and C in Fig. (7.1). At the final stages of deformation the variation of the thickness near the pole is much greater than the variation of the curvatures, and because of the opposite effect of t on the stress function, the position of maximum stress shifts towards the pole of the shell.

In forming processes without draw-in and neglecting the effect of the die edge, the value of N varies between O and 1.5, Fig. (6.18). Thus the stress condition varies from the mean condition of balanced biaxial stretching ($\sigma_\theta = \sigma_s$) to those conditions of plane strain ($\sigma_\theta = 2\sigma_s$ and $\sigma_s = 2\sigma_\theta$). In the two conditions of plane strain at the extremes, at one extreme when $\sigma_\theta = 2\sigma_s$, the meridional tangential incremental strain tends to be zero, the circumferential expansion being compensated by thinning; and at the other extreme when $\sigma_s = 2\sigma_\theta$, the circumferential incremental strain tends to be zero, the stretch in the meridional tangential direction being also compensated by thinning. All the stress conditions inbetween these extremes may, in fact, be resolved into two components, a balanced biaxial stretching, and a stress for plane strain (or pure shear, as it is sometimes called); thus,

$$\sigma_\theta = \frac{\sigma_\theta + \sigma_s}{2} + \frac{\sigma_\theta - \sigma_s}{2} \qquad (7.9)$$

$$\sigma_s = \frac{\sigma_\theta + \sigma_s}{2} - \frac{\sigma_\theta - \sigma_s}{2} \qquad (7.9)$$

where the first terms of the right hand sides of Eq.(7.9) constitute a balanced biaxial stretching, and the second terms constitute the stress producing plane strain, or pure shear. The ratio between these two components is, of course, a function of N, or prolateness ($\bar{p}$), thus,

$$\frac{\frac{\sigma_\theta + \sigma_s}{2}}{\frac{\sigma_\theta - \sigma_s}{2}} = \frac{\bar{P} + 2}{\bar{P}} = \frac{3 - N}{1 - N} \qquad (7.10)$$

The balanced biaxial stretching stress is always positive (tensile), but the pure shear component in Eq. (7.10) can be positive or negative depending on the prolateness or oblateness of the deformed shell.

In Fig. (7.6), the pure shear stress is plotted against balanced-biaxial stress with the radial lines indicating the prolateness of the local surface. These lines are obtained from Eq. (7.10), and the line of N = 1 or the $(\frac{\sigma_\theta + \sigma_s}{2})$ axis denotes a sphere and the negative $(\frac{\sigma_\theta - \sigma_s}{2})$ axis shows an oblate spheroid of N = 1.5. If the surface of a deformed shell had been a sphere for all stages of deformation, everywhere the shell would be subjected to balanced biaxial stretching and the curves in Fig. (7.6) would collapse into a horizontal line.

As seen in Fig. (7.6), the maximum variation of the balanced biaxial stresses along the bulge increases with deformation, and the highest balanced biaxial stress on each curve corresponds to the pole of the bulge. The difference of the balanced biaxial stresses at the pole and annular ring also increases with severity of deformation until fracture takes place. The variation of pure shear stresses in the specimen between the pole and

die edge has the same pattern as balanced biaxial stresses, but at some stages in the third mode of deformation (curves h to k), the maximum pure shear stress variation increases tremendously. This maximum variation in terms of length along the $(\frac{\sigma_\theta - \sigma_s}{2})$ axis consists of two parts separated by the line $N = 1$. Thus the length above the line $N = 1$ represents pure shear stress variation in the prolate section of the shell; and the length beneath the line $N = 1$ shows the shear stress variation in the oblate region of the bulge. The shear stress in the bulged specimen can now be visualised clearly. In general, the shear stress variation in the prolate portion increases with deformation throughout the bulging process owing to the general increase of prolateness. The shear stress variation in the oblate portion, however, reduces its magnitude rapidly with further deformation.

7.3 Relationship between deviatoric stresses and prolateness

As discussed in section (4.4.1), any flow stress consists of two components, hydrostatic and deviatoric responsible for elastic and plastic deformation respectively. In the present analysis, the hydrostatic component is ignored since only large plastic strains are considered. States of deviatoric stress can be deduced from Eq. (4.18), thus

hydrostatic stress $\sigma_m = {}^1/3\ (\sigma_s + \sigma_\theta)$

deviatoric circumferential stress $\sigma'_\theta = \sigma_\theta - \sigma_m$ (7.11)

deviatoric meridional tangential stress $\sigma'_s = \sigma_s - \sigma_m$

and deviatoric through-thickness stress $\sigma'_t = -\sigma_m = -(\sigma'_\theta + \sigma'_s)$

It is possible to relate any state of deviatoric stress to the prolateness of the deformed shell by introducing the index of sphericality (N) into the Eq. (7.11). Therefore, by the definitions of σ_s and σ_θ given by Eqs. (3.5) and (3.6), the hydrostatic and deviatoric stresses are

$$\begin{aligned} \sigma_m &= \frac{3 - N}{3}\ \sigma_s \\ \sigma'_s &= \frac{N}{3}\ \sigma_s \\ \sigma'_\theta &= \frac{3 - 2N}{3}\ \sigma_s \\ \sigma'_t &= -\sigma_m = \frac{N - 3}{3}\ \sigma_s \end{aligned} \qquad (7.12)$$

The relationship between the non-dimensional stresses and index of sphericality are obtained by dividing the Eq. (7.12) by the meridional tangential stress. Thus,

$$\begin{aligned} \frac{\sigma_m}{\sigma_s} &= 1 - \frac{1}{3}\ N \\ \frac{\sigma'_s}{\sigma_s} &= \frac{1}{3}\ N \end{aligned} \qquad (7.13)$$

$$\frac{\sigma'_\theta}{\sigma_s} = 1 - \frac{2}{3} N$$

$$\frac{\sigma'_t}{\sigma_s} = \frac{1}{3} N - 1$$

These non-dimensional stresses in Eq. (7.13) are only functions of N so that when they are plotted against N, the dimensionless hydrostatic stress ($\frac{\sigma_m}{\sigma_s}$) becomes a straight line of slope ($-\,{}^1/_3$) passing through the coordinate (O, 1), line AE in Fig. (7.7). σ'_θ/σ_s is also a straight line (AD) of slope ($-\,{}^2/_3$) passing through the same coordinate. Similarly, the dimensionless deviatoric meridional tangential and through thickness stresses are both straight lines having positive slope of (${}^1/_3$), the former (line OD) passing through the origin, and the latter (line BC) passing through the point (O, -1) in Fig. (7.7). The two straight lines (OD) and (AD) intersect at N = 1, thus forming a triangle having vertices of coordinates O (O,O), A (O,1) and D (1, ${}^1/_3$). Moreover, for any given value of N, it can easily be shown that the prolateness of the shell corresponding to this N value is given by the vertical distance between the two sides (AD and OD) of the shaded triangle OAD in Fig. (7.7).

The above analysis suggests the possible use of the N value onto the clock diagram for deviatoric stress so

that prolateness ($\bar{P} \equiv 1 - N$) can be related to the characteristic indices (ζ) as shown in Fig. (7.8). The insets in Fig. (7.8) for $2<\zeta<8$ show the meridional sections of constant N surfaces which are discussed in Fig. (3.4). Thus, it is seen that within this region of $2<\zeta<8$, the surface is prolate only when $6<\zeta\leqslant 7$; and at everywhere of $2<\zeta<6$, the surface is always oblate. For the special case of $\zeta = 6$, the surface is spherical. Some reflection will show that the surface of the shell is always closed for $2<\zeta<7$ and becomes open in the region $7<\zeta<9$.

7.4 Deviatoric stresses in the bulge test

It has been shown in section (4.4.2) that the deviatoric stress components ($\acute{\sigma}_t$, $\acute{\sigma}_\theta$, $\acute{\sigma}_s$) of the biaxial principal stresses (σ_s ,σ_θ) in the bulge test have only two degrees of freedom, i.e. $\acute{\sigma}_t + \acute{\sigma}_\theta + \acute{\sigma}_s = 0$. This property is used for representation of states of deviatoric stress on the triangular coordinate system.

The set of curves in Figs. (7.9) and (7.10) represent states of deviatoric stress in the second and third modes of deformation of the specimen and are plotted on different scales for clarity. In these figures, the deviatoric stress paths and deviatoric stress distribution curves are represented by solid and dotted lines respectively. It can be deduced from Figs. (7.9) and (7.10) that the deviatoric stress paths for the second mode of deformation ($0.5 < H/a < 1.2$) are nearly

radial, specially for $0 < r_o < 32$ mm. In the third mode of deformation, however, the deviatoric stress paths are more curved when $r_o > 0$. The characteristic index (ζ) shifts from 5 o'clock to 7 o'clock as deformation progresses. The reason for this phenomenon can be explained by the N distribution curves, Fig. (6.14), and their effects on the clock diagram which are shown in Fig. (7.8).

At the initial stages of deformation the specimen is totally oblate, and therefore the deviatoric stress distribution curve crosses the line of $\zeta = 6$ only once and that is at the pole and the whole length of the curve lies in the region of $5 < \zeta \leq 6$ (not shown in Fig. 7.9). In the second mode and some stages in the third mode of deformation, the deformed shell is divided into two zones by an annular ring of perfect spherical surface (section 6.5.3), prolate inside and oblate outside it. Moreover, the local sphericality at the pole of the bulge is always a perfect sphere (N = 1). From Fig. (6.18) it may be concluded that, in the clock diagram for deviatoric stresses, the stress distribution curves must intersect the $\zeta = 6$ line twice, thus forming a loop in the region of prolateness ($6 < \zeta < 7$). The direction of the loops in the clock diagram in Figs. (7.9) and (7.10) can easily be seen by considering the meridional tangential stress condition at the pole and annular ring of perfect sphere. At these two positions in the bulge, N is unity and from Figs. (7.3) and (7.4), it can easily be deduced

from Eq. (7.10) that the loops must emerge in the counter-clockwise direction.

The start of the second mode of deformation characterised by curve (b) in Fig. (7.9) reveals that the local sphericality is less prolate before and less oblate after the annular ring of perfect sphere is reached on comparing with the sphericality at some final stage in the second mode of deformation (e.g. curve f in Fig. 7.9) so that change of direction of ζ results from the second to the third mode of deformation. For further deformation (curves g to k), the general trend is increasing prolateness so that the deviatoric stress paths have to curve towards the left of the $\zeta = 6$ line as shown in Fig. (7.10). At the final stages of deformation, the prolate region expands outwards and the whole shell becomes prolate. Thus, it can be seen from Fig. (7.10) that the deviatoric stress paths, especially near the die edge, are more drastically curved towards the prolate region of the clock diagram ($6 < \zeta < 7$) so that the entire stress distribution curve lies within this region.

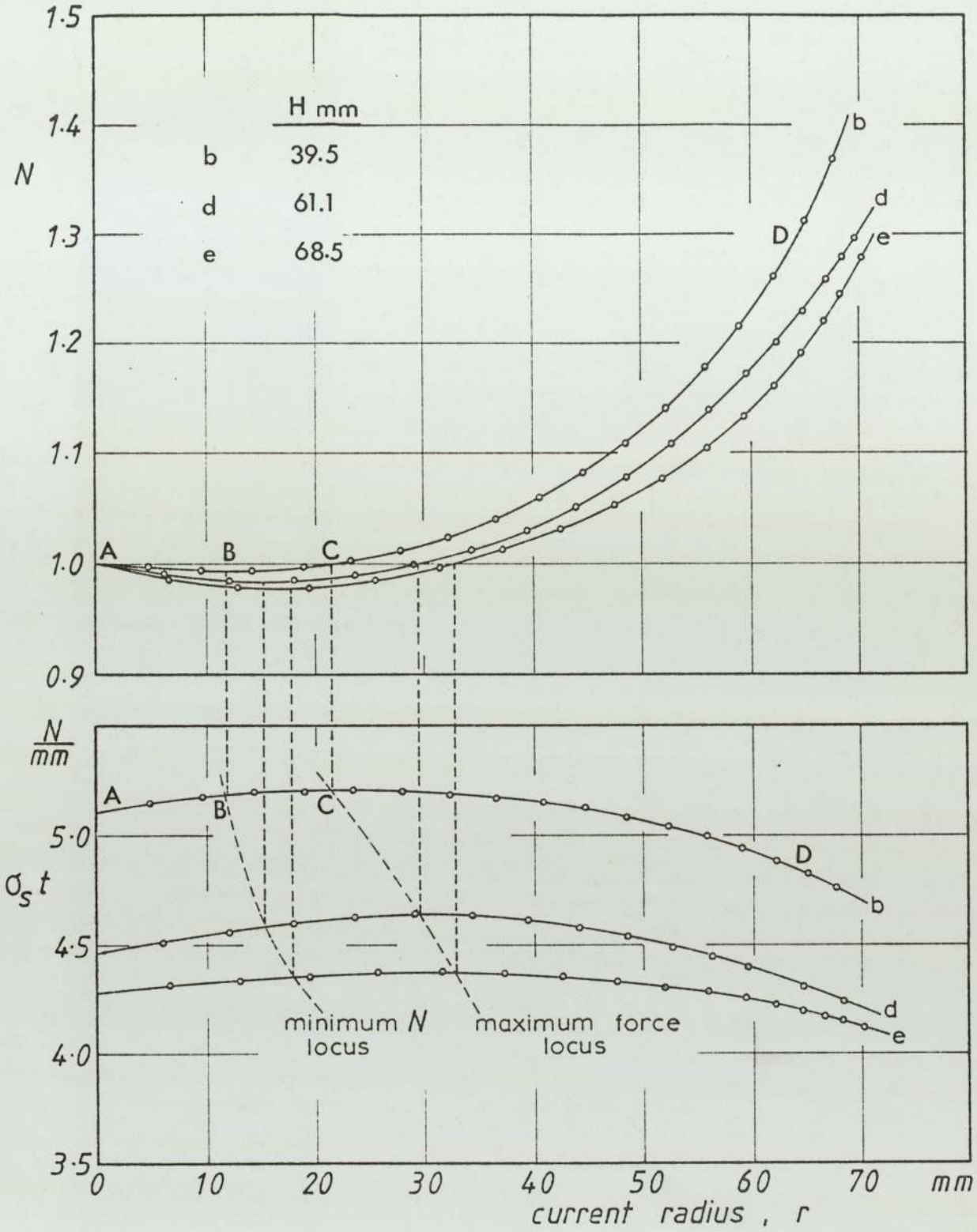

Fig. 7-1 – Variation of meridional force in the second mode of deformation.

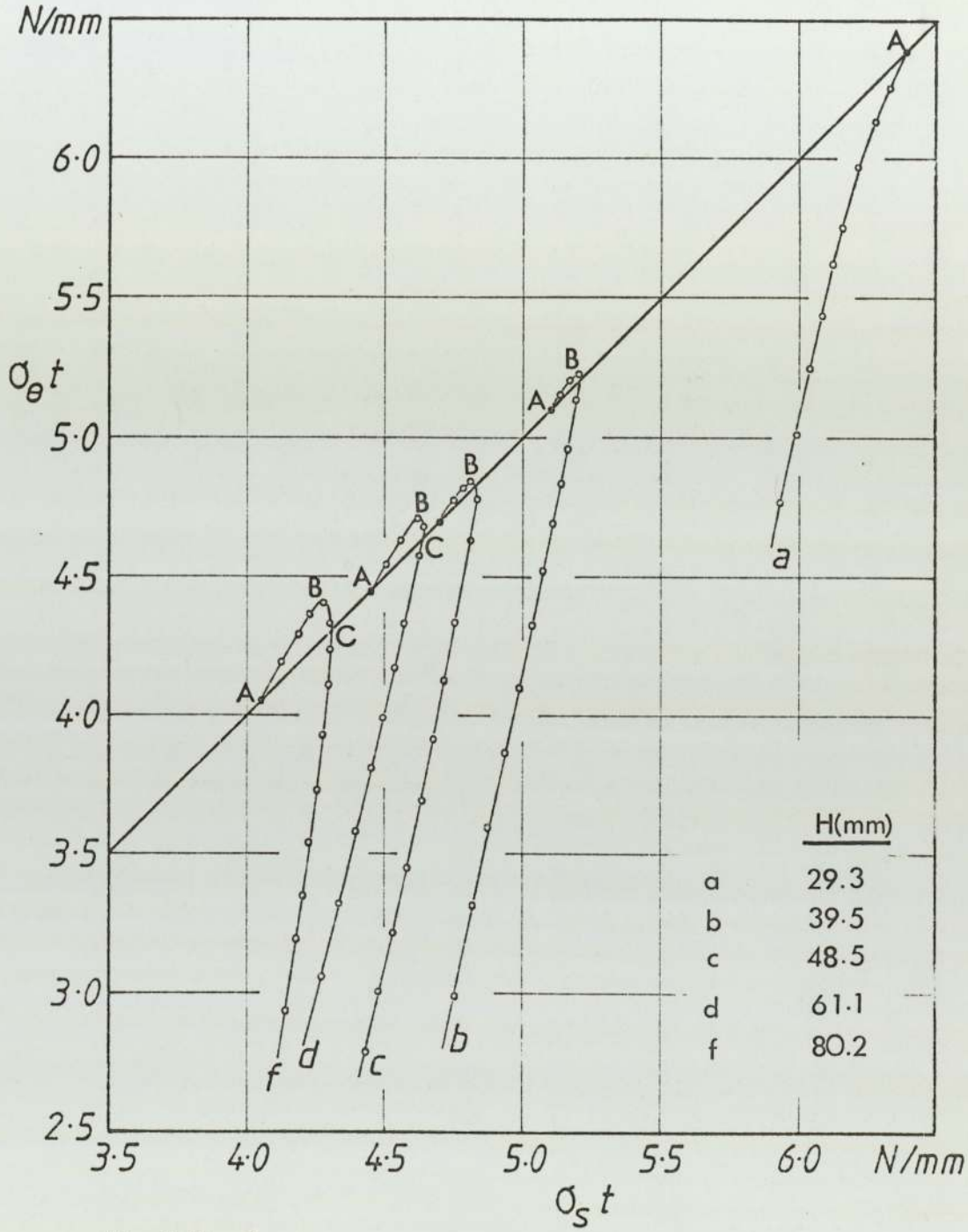

Fig. 7-2 – Forces per unit sectional length in the workpiece.

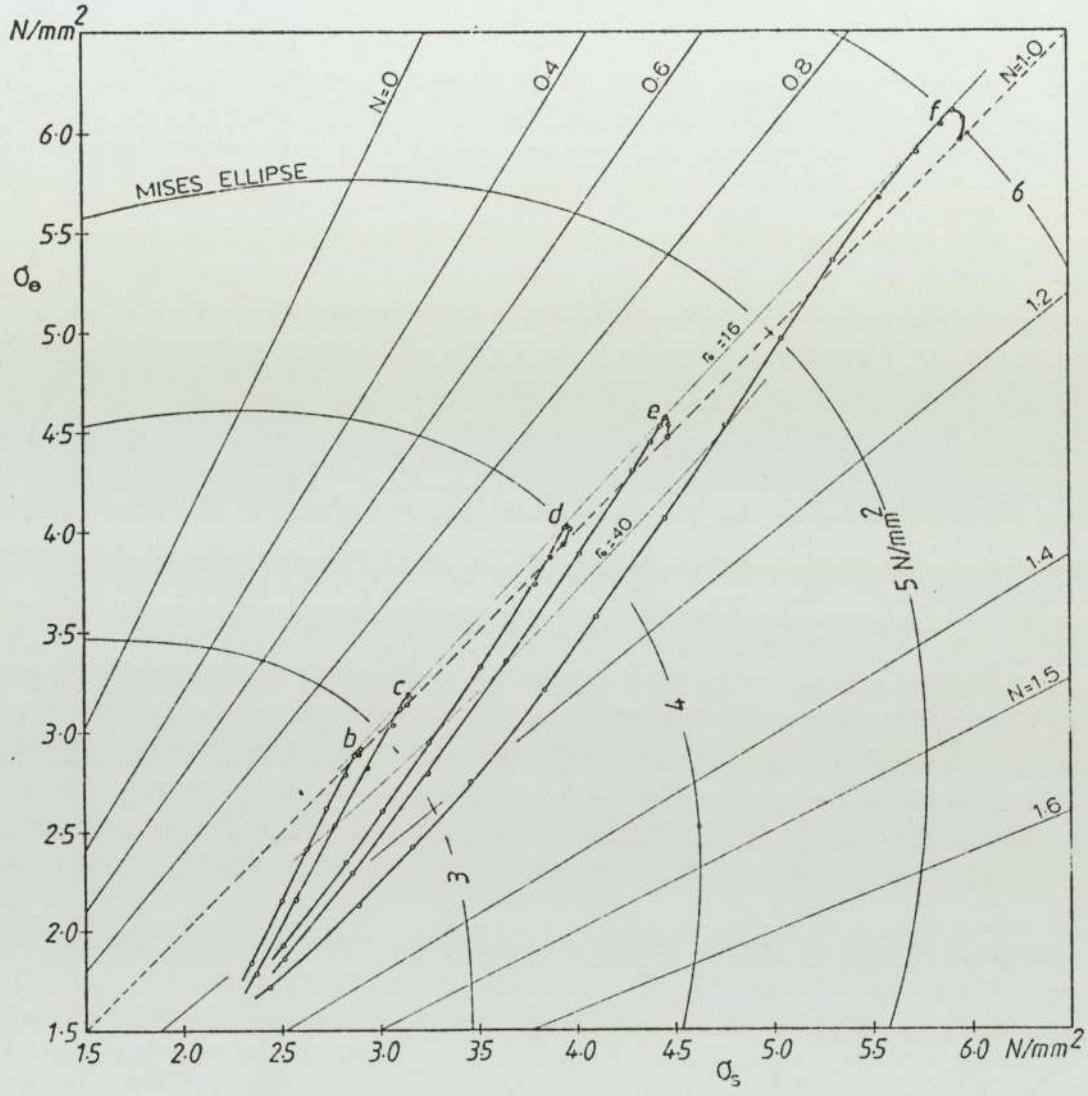

Fig. 7-3 – Stress distribution in the second mode of deformation.

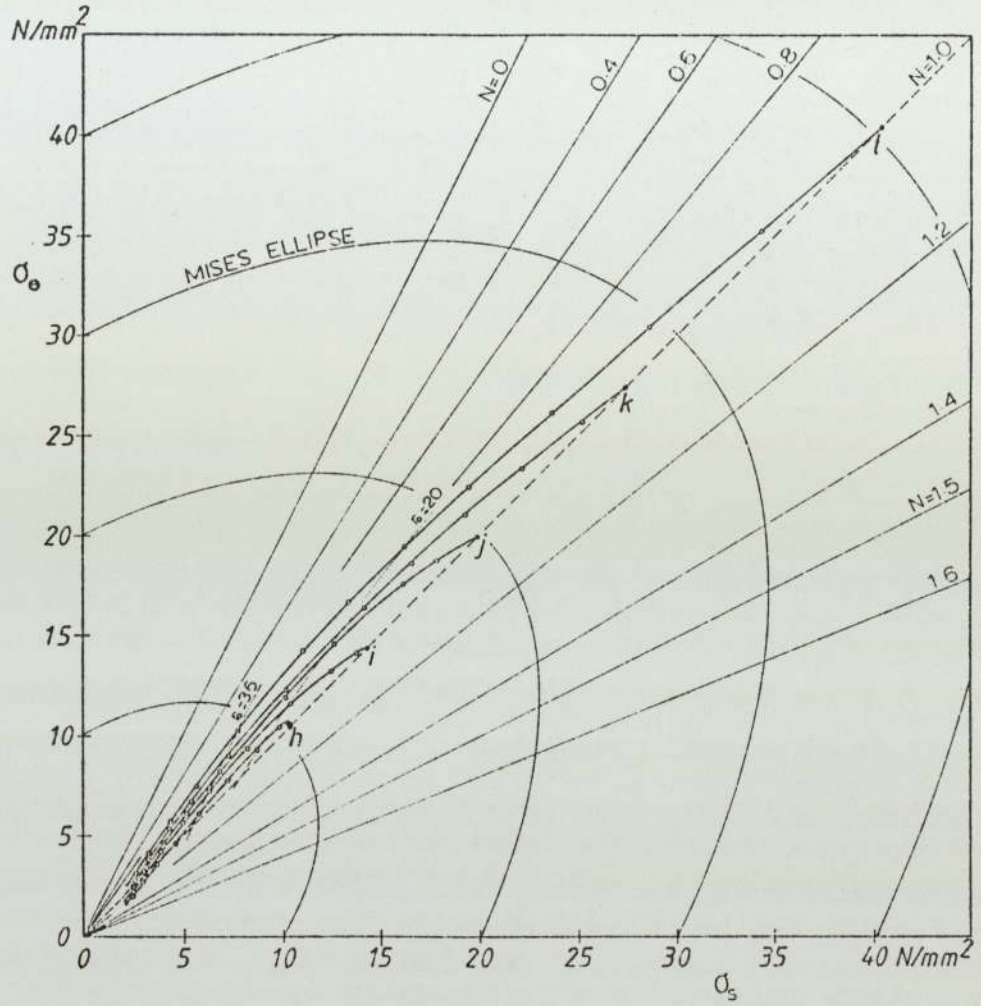

Fig. 7_4 – Stress distribution in the third mode of deformation.

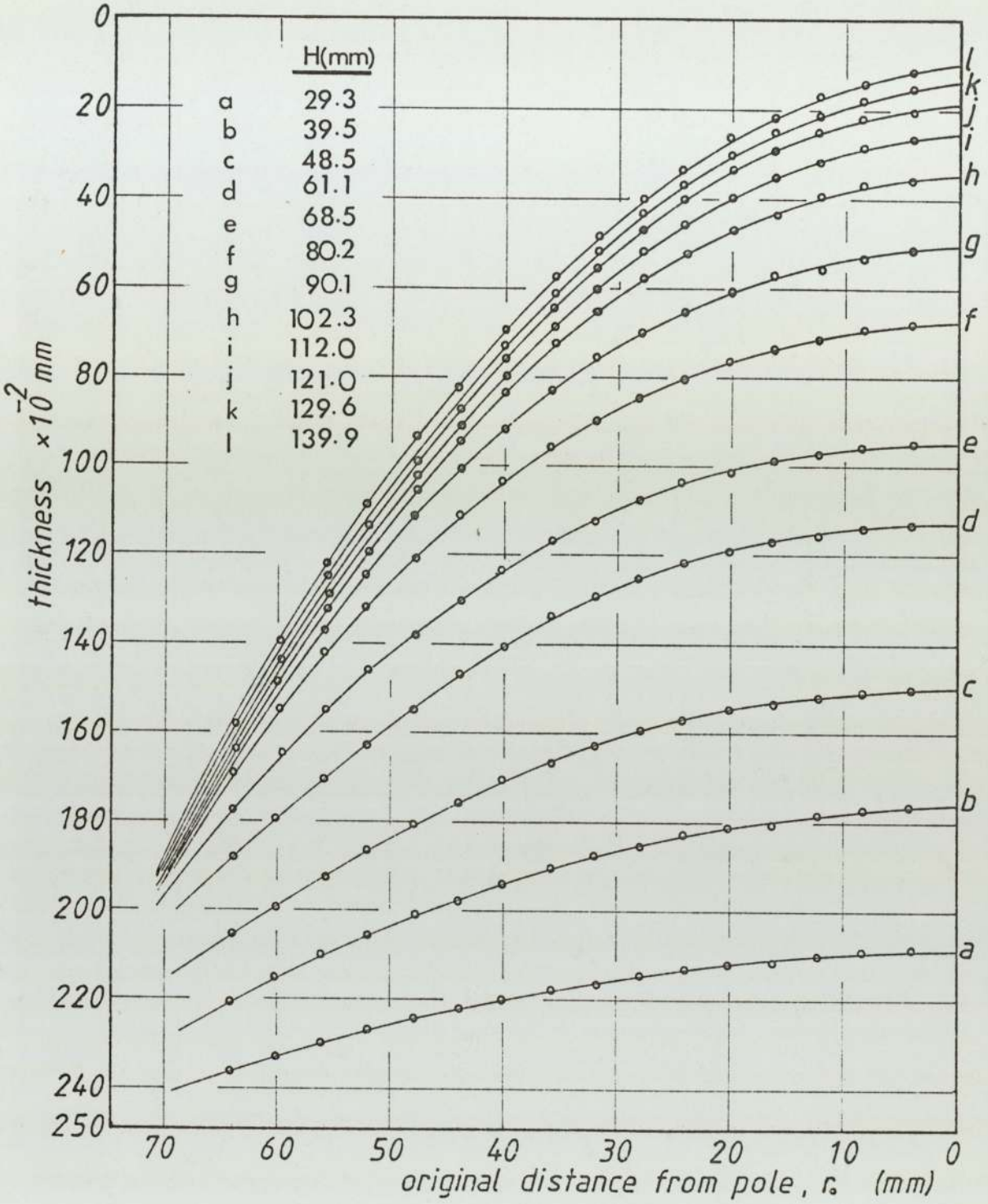

Fig. 7.5 – Thickness variations in the bulged specimen.

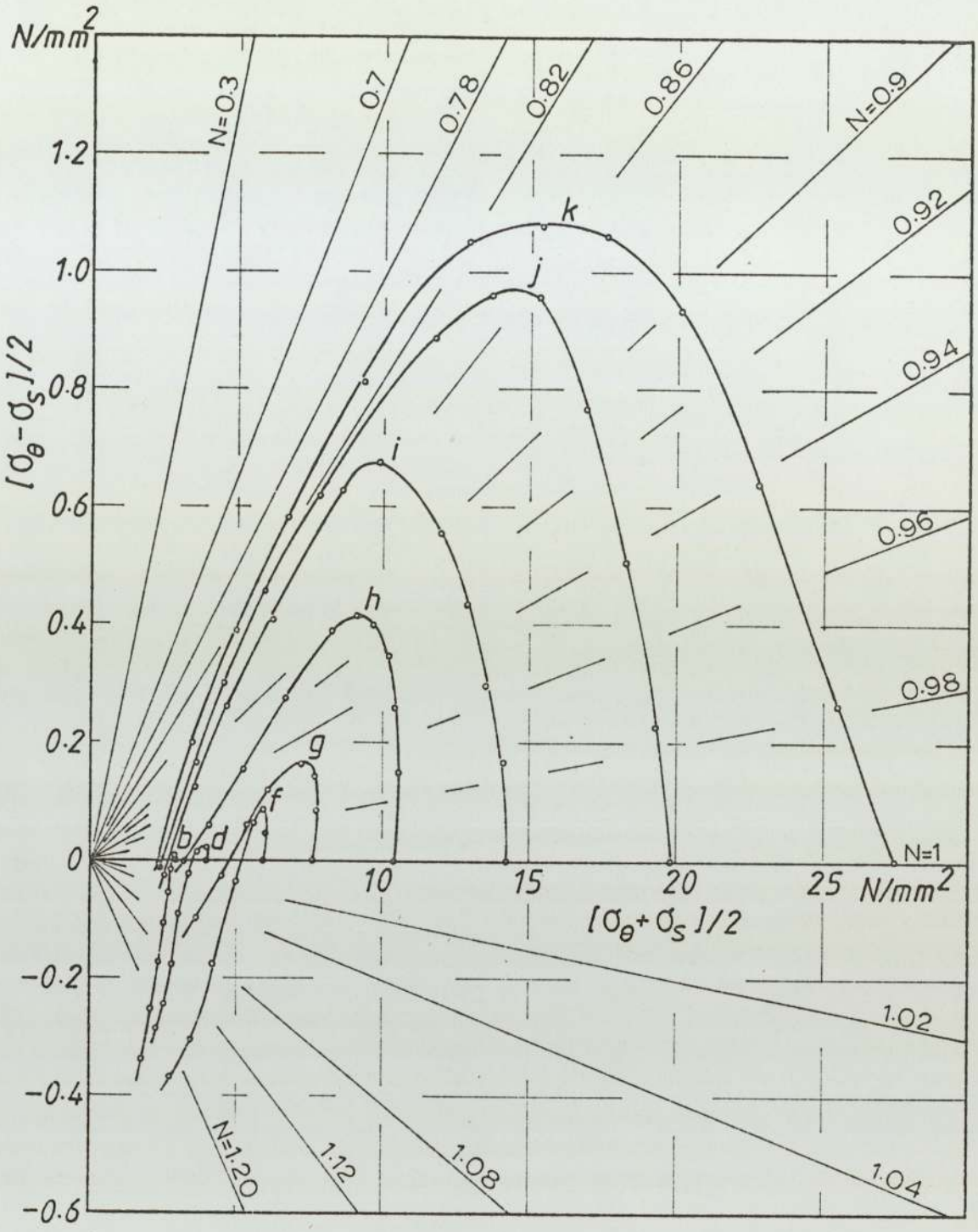

Fig. 7.6 – Balanced biaxial and pure shear stresses in the bulged specimen.

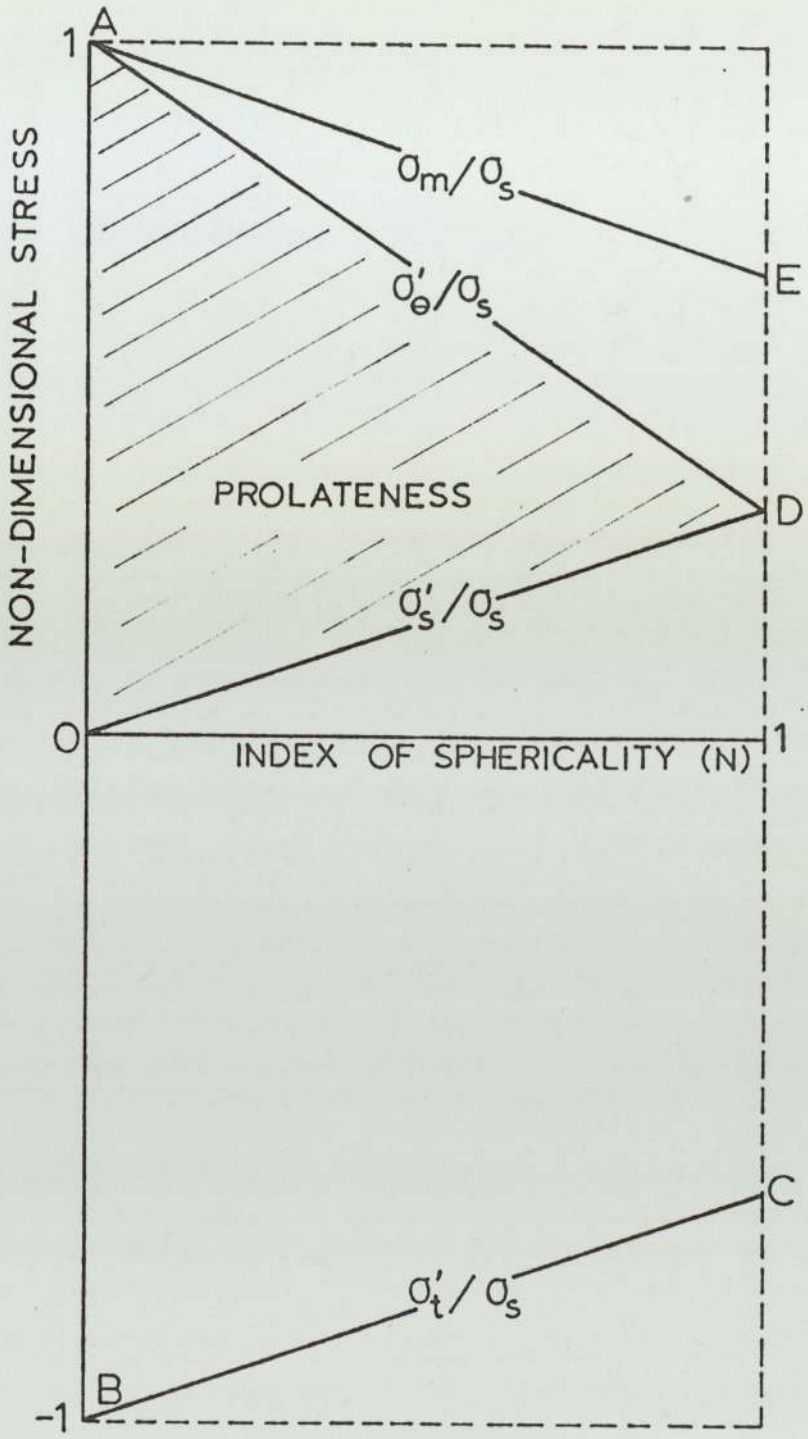

Fig. 7-7 - Non-dimensional deviatoric stresses in the bulge test .

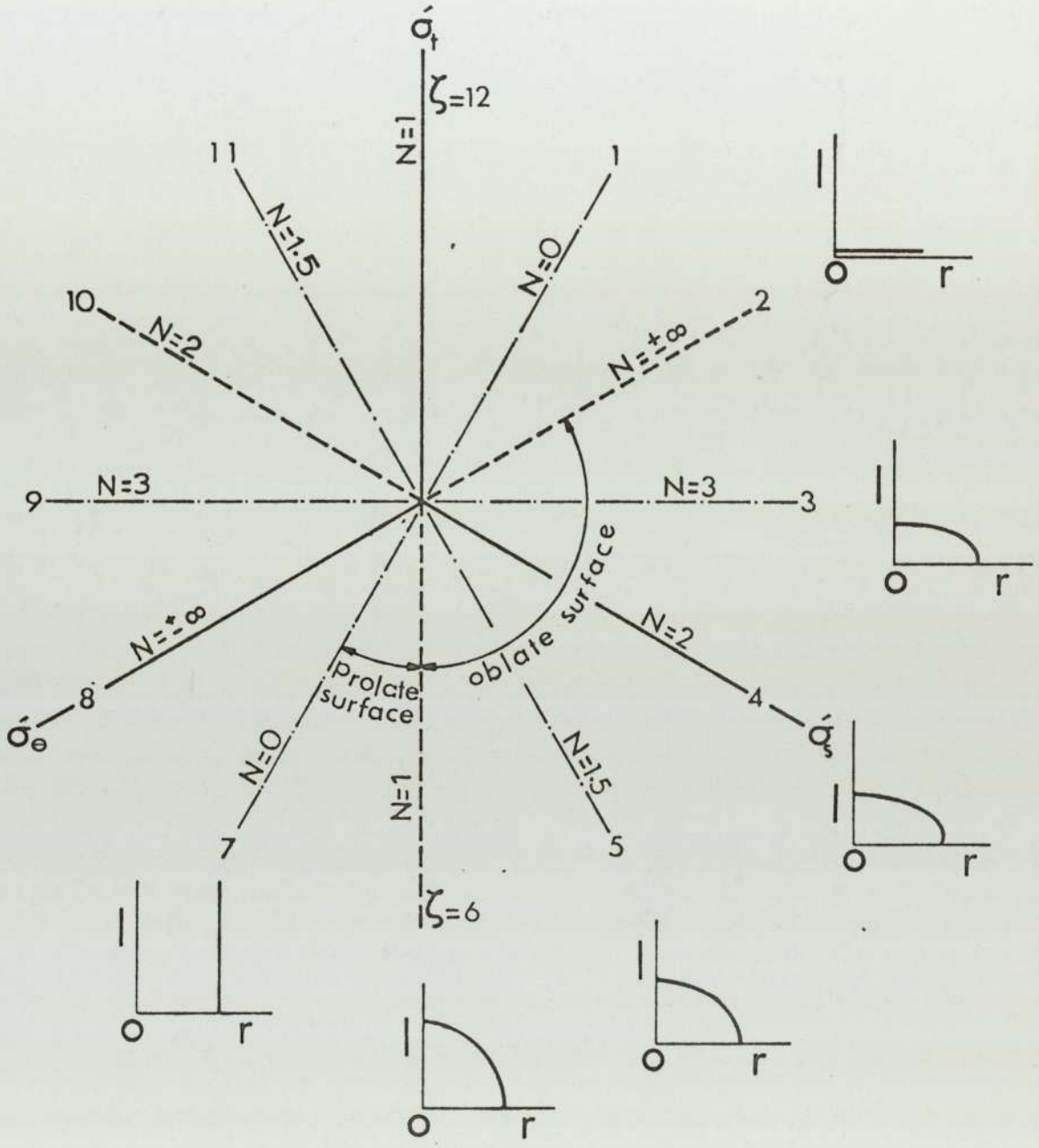

Fig. 7-8 – Prolateness and characteristic index for deviatoric stresses.

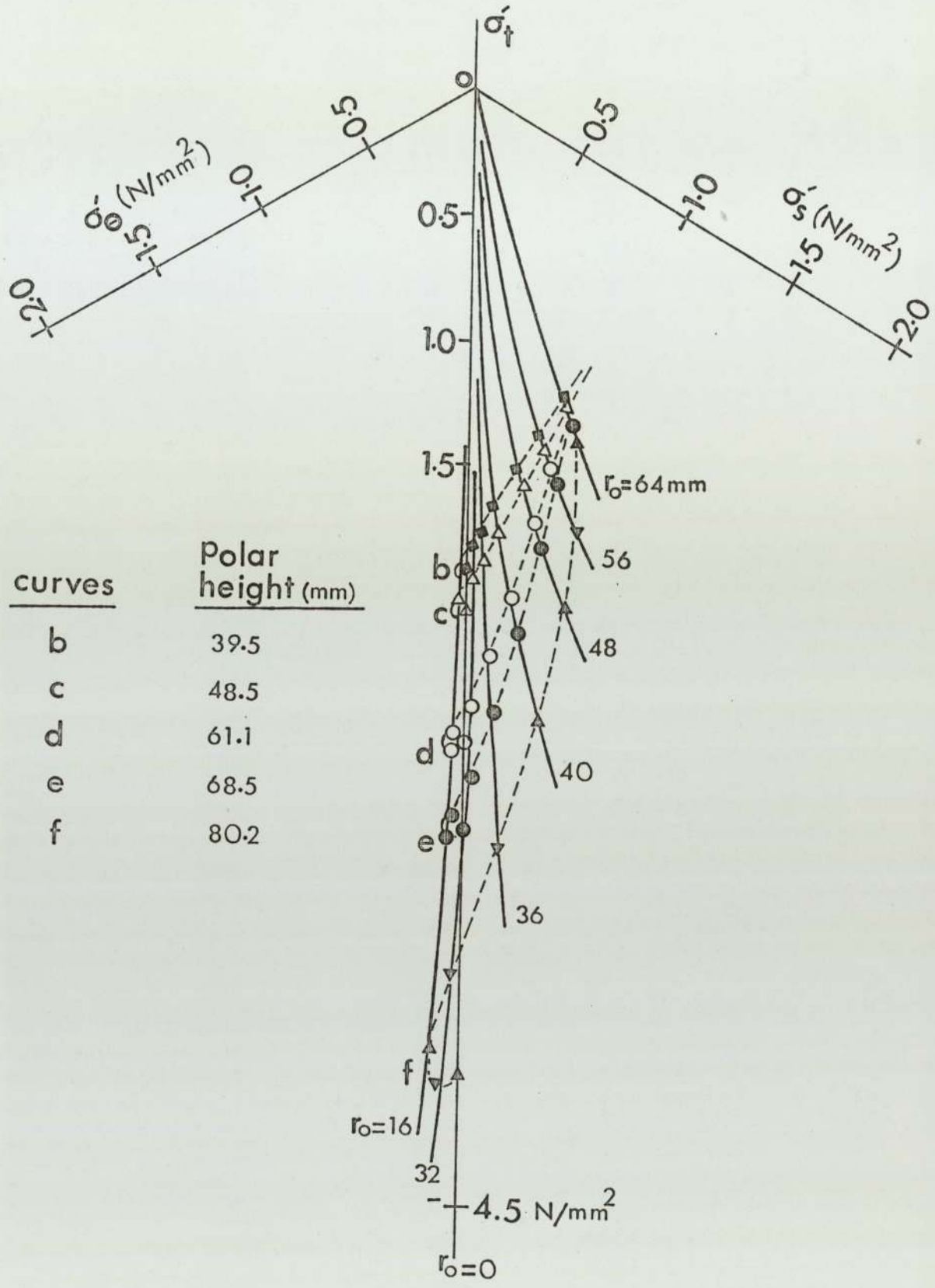

Fig. 7-9_ States of deviatoric stress in the second mode of deformation.

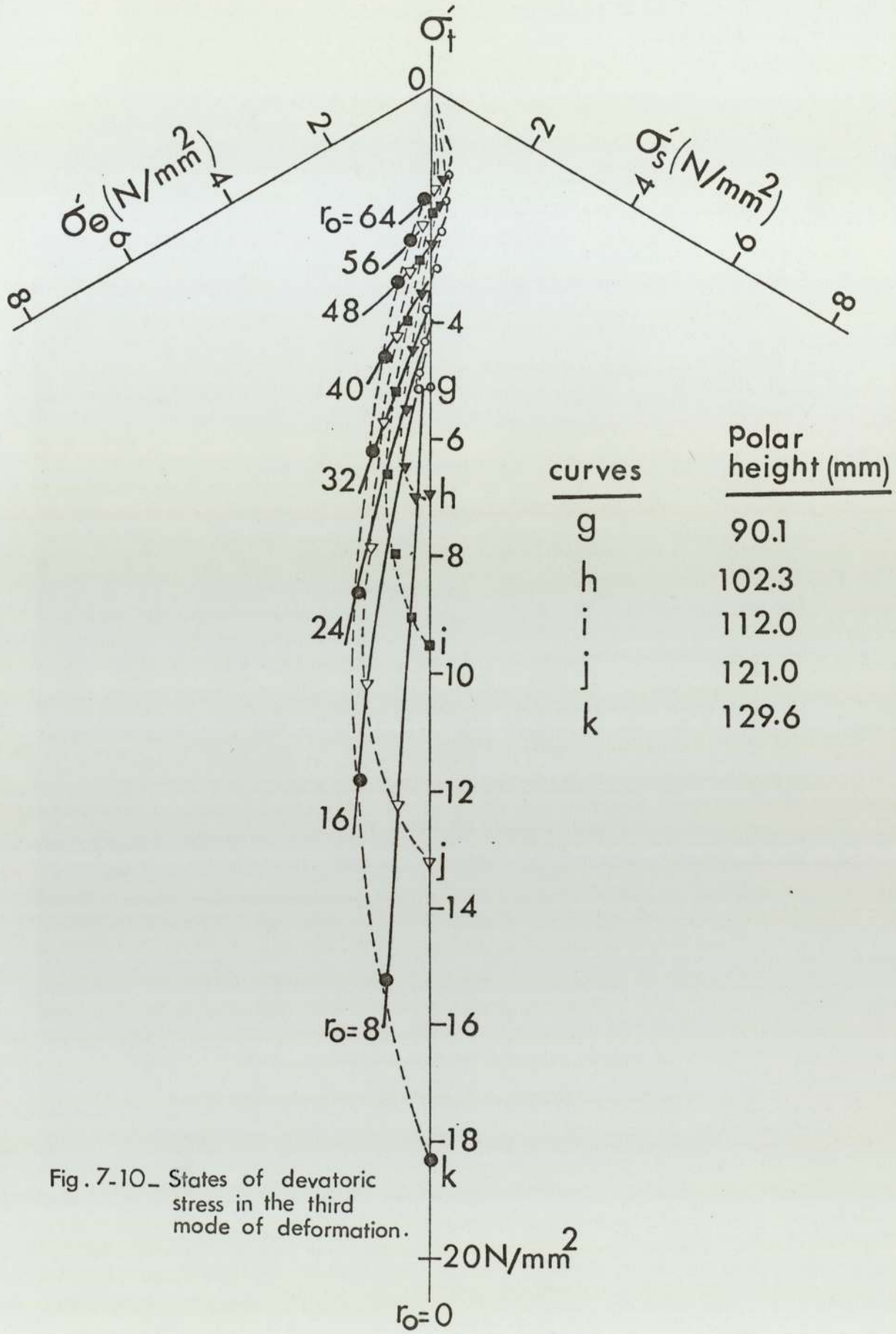

Fig. 7-10_ States of devatoric stress in the third mode of deformation.

CHAPTER 8

STRAINS AND STRAIN-RATES IN THE BULGE TEST

Chapter 8

Strain and Strain-Rates in the Bulge Test

This chapter is focussed on the detailed study of the states of strain and strain-rates of a real bulged specimen based on sections (3.3) to (3.5). The trace of the progress of deformation from one stage to the other of an element in the deformed specimen together with the states of strain are plotted in the triangular coordinate system. To serve as a basis for stress, strain and strain-rate relationship determination, states of strain-rate are also calculated and plotted in the triangular coordinate system.

8.1 Strain paths and strain distributions

As shown in section 4.2, the states of strain in the bulge test can graphically be represented as points in the triangular coordinate system. These points can be plotted from the experimental results not only for every stage in the deformation, but also along the entire specimen. These constitute the strain paths and strain distribution curves respectively.

Through the incompressibility condition of metals in plastic deformation, only two principal strains of the three are sufficient to define the state of strain of any elementary particle in the bulged specimen. In this project, the circumferential and through thickness strains are calculated from the following procedures:

The circumferential strain is simply calculated from Eq. (3.21) which is $\varepsilon_\theta = \ln (r/r_o)$, by measuring accurately the original and current radii. The through-thickness strain can be calculated from Eq. (3.22) which is $\varepsilon_t = \ln (t/t_o)$, by measuring the current thickness of the bulged specimen. However, due to inaccuracies of the thickness measurements specially at the final stages of deformation, a new way based on the measured angle of inclination of meridian section (θ) and circumferential strain (ε_θ) to calculate ε_t is proposed and used in this project. By differentiating ε_θ ($= \ln r/r_o$) with respect to r_o and substituting the term $\frac{dr}{dr_o}$ into that term in the definition of ε_s ($= \ln (\frac{dr}{dr_o} \frac{1}{\cos\theta})$), the following compatibility equation is obtained,

$$\varepsilon_s - \varepsilon_\theta = \ln \left(\frac{1+r_o \frac{d\varepsilon_\theta}{dr_o}}{\cos\theta}\right) \qquad (8.1)$$

Using the incompressibility equation, the through-thickness strain is,

$$\varepsilon_t = -2\varepsilon_\theta - \ln \left(\frac{1+r_o \frac{d\varepsilon_\theta}{dr_o}}{\cos\theta}\right) \qquad (8.2)$$

The value of $\frac{d\varepsilon_\theta}{dr_o}$ is derived from Fig. (8.1) by an adjustable set square; and the source of the largest error in the calculation of ε_t is in θ. The overall maximum error in ε_t is estimated to be less than 3 percent except for the region very near to the pole.

The characteristic index (η) of any state of strain can be decided by Eq. (8.1), or simply by the definition of ε_s and ε_θ. Thus,

$$\varepsilon_s - \varepsilon_\theta = \ln \left(\frac{dr}{dr_o} \frac{1}{\cos\theta} \frac{r_o}{r}\right) = \ln \left(\frac{1}{\cos\theta} \frac{d(\ln r)}{d(\ln r_o)}\right) \tag{8.3}$$

Obviously, for any stage of deformation, the bracketed term in Eq. (8.3) must have some positive values, that is,

$$\frac{dr}{dr_o} \frac{1}{\cos\theta} \frac{r_o}{r} > 0 \tag{8.4}$$

r and r_o are positive quantities, but $\cos\theta$ and $\frac{dr}{dr_o}$ can take both positive and negative values depending on the stage of deformation. By referring to Fig. (8.2), it is observed that up to stage "f" ($H/a < 1.2$) $\frac{dr}{dr_o}$ is always positive and $\cos\theta$ is also positive ($\theta < \pi/2$). When H/a exceeds 1.2, the bulge expands in axial direction, resulting in a negative $\cos\theta$ near the rim of the bulge ($\theta > \pi/2$). Over this region $\frac{dr}{dr_o}$ must be less than zero, meaning decrease of r with r_o. This condition is shown in Fig. (8.2).

The strain paths and strain distribution curves for superplastic Zn-Al eutectoid alloy in the bulge test are shown in Fig. (8.3) in which the solid and dotted

lines represent strain paths and strain distributions respectively. The maximum strain (ε_t) obtainable in the bulge test is much greater than the value -1.3 shown in Fig. (8.2) (specimen f, H = 80.2 mm), and is -3.44 when H is 142 mm and considerably exceeds -4.0 when the bulge breaks.

It is clearly shown in Eq. (8.3) that the characteristic index (η) in the bulge test is greater or less than 6 o'clock depending on whether $(\frac{dr}{dr_o} \frac{1}{\cos\theta} \frac{r_o}{r})$ is less or greater than unity respectively. For the curves plotted in Fig. (8.3), all the strain distribution curves lie in the region $5<\eta<7$ in accordance with Eq. (8.4) and the N variation in the shell.

It has been shown in section (6.5.3) that in the second and third modes of deformation, the bulge is divided into two zones by an annular ring of perfect spherical surface, prolate inside and oblate outside it. Moreover, the bulge is always a perfect sphere at the pole. Therefore, it may be concluded that the strain distribution curves in the triangular coordinate system must intersect the $\eta = 6$ line (the line of balanced biaxial stretching) twice and form a loop in the region of prolateness ($6<\eta<7$). Obviously, at the final stage of deformation, when the whole shell becomes prolate, the entire strain distribution curve lies within the prolate region of the diagram ($6<\eta<7$).

It is seen in Fig. (8.3) that the strain paths in the first and second mode of deformation are nearly radial along the specimen towards the die edge, indicating an almost constant strain ratio for any particular element particle during successive deformation. In the third mode of deformation (not shown in Fig. 8.3), every particle element is subjected to a different strain ratio at a different stage of deformation because the strain distribution curves shift to the left of the diagram at this stage.

8.2 Strain-rates in the bulge test

The principal strain rates, just like principal strains, have only two degrees of freedom as shown in Eq. (3.28), so that the triangular coordinate system may be used in the analysis of strain-rates. In order to comply with the use of this coordinate system for strains, the vertical axis denotes the through-thickness strain-rate; and the left and right hand axes represent the circumferential and meridional tangential strain-rates respectively.

It was suggested in Chapter 3 that the strain-rates in the bulge test can be obtained by measuring the rate of change of r, l and θ. However, it is more practicable to obtain the state of strain-rate simply by differentiating each principal strain with respect to time (T). This requires accurate measurements of time

which can be done easily by the method described in section (5.3.4). Fig. (8.4) shows the time-height relationship at a constant pressure of 0.103 N/mm^2. As seen in this figure, in the first mode of deformation, the bulge rate varies rapidly and there is an almost instantaneous expansion followed by a comparatively short period in which the bulge rate falls to an almost constant value. In the third mode of deformation, the bulge rate accelerates and finally leads to rupture.

Having obtained the time-height relationship in the bulge test, it is possible to construct the strain-time graph for any two of the three principal strains and differentiate them for the values of strain-rates. Since the initial stage of the bulging process is of short duration and the final stage leads quickly to rupture which results in relatively high strain-rates, therefore, the values of strain-rates cannot be shown clearly in the triangular coordinate system for the whole process of bulging. However, the greatest interest lies in the second mode of deformation in which the bulge rate is almost constant. By using the above method, the states of strain-rate and strain-rate paths are plotted in Fig. (8.5) as dotted and solid lines respectively.

An alternative method may be used to represent the state of strain rate ($\dot{\varepsilon}_t$, $\dot{\varepsilon}_\theta$, $\dot{\varepsilon}_s$) as a point in the triangular coordinate system by differentiating the strain path at the point (ε_t, ε_θ, ε_s) also in the triangular

coordinate system. The direction of the radial lines passing through the origin and ($\dot{\varepsilon}_t$, $\dot{\varepsilon}_\theta$, $\dot{\varepsilon}_s$) is also that of the tangent at the point (ε_t, ε_θ, ε_s) on the strain path.

The vertical strain-rate path pointing downwards in Fig. (8.5) represents a balanced biaxial stretch ($\dot{\varepsilon}_t$ negative). It is easily seen in this figure that the strain-rate paths are nearly radial along the specimen indicating an almost constant strain-rate ratio for any particular elementary particle during successive deformation.

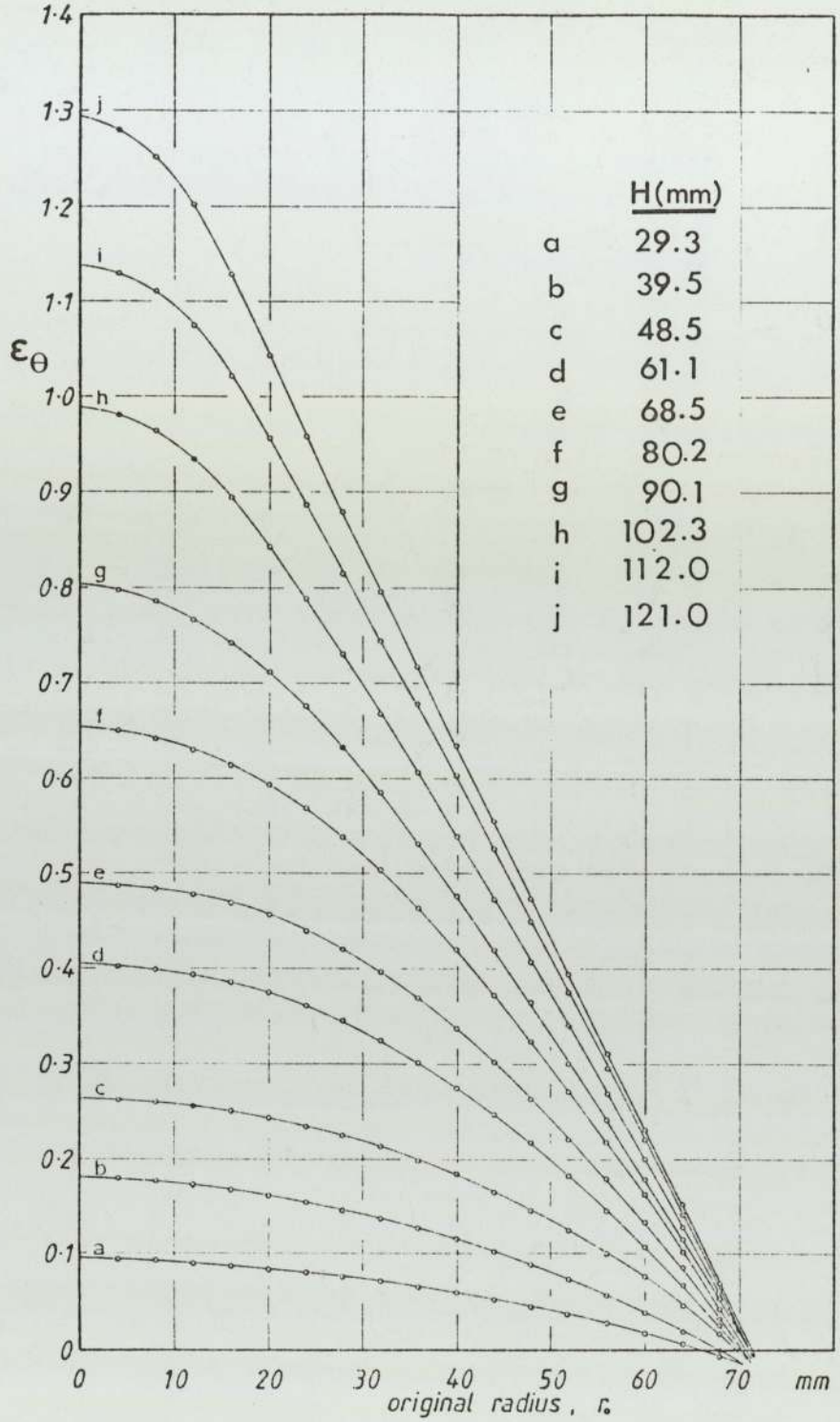

Fig. 8-1- Variations of circumferential strain in the bulged specimen .

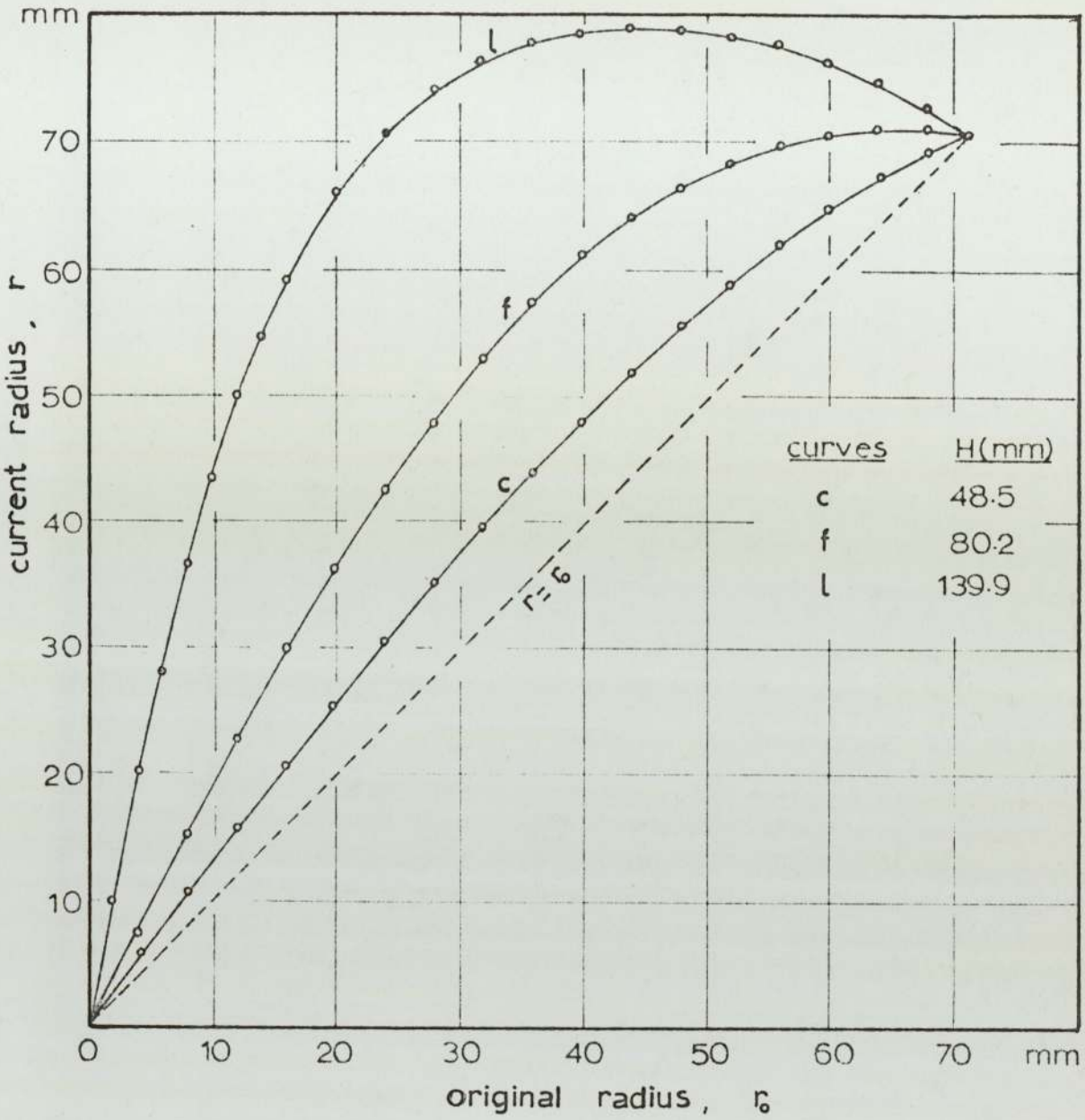

Fig.8-2- Radial movements of the material particles in the bulged specimens.

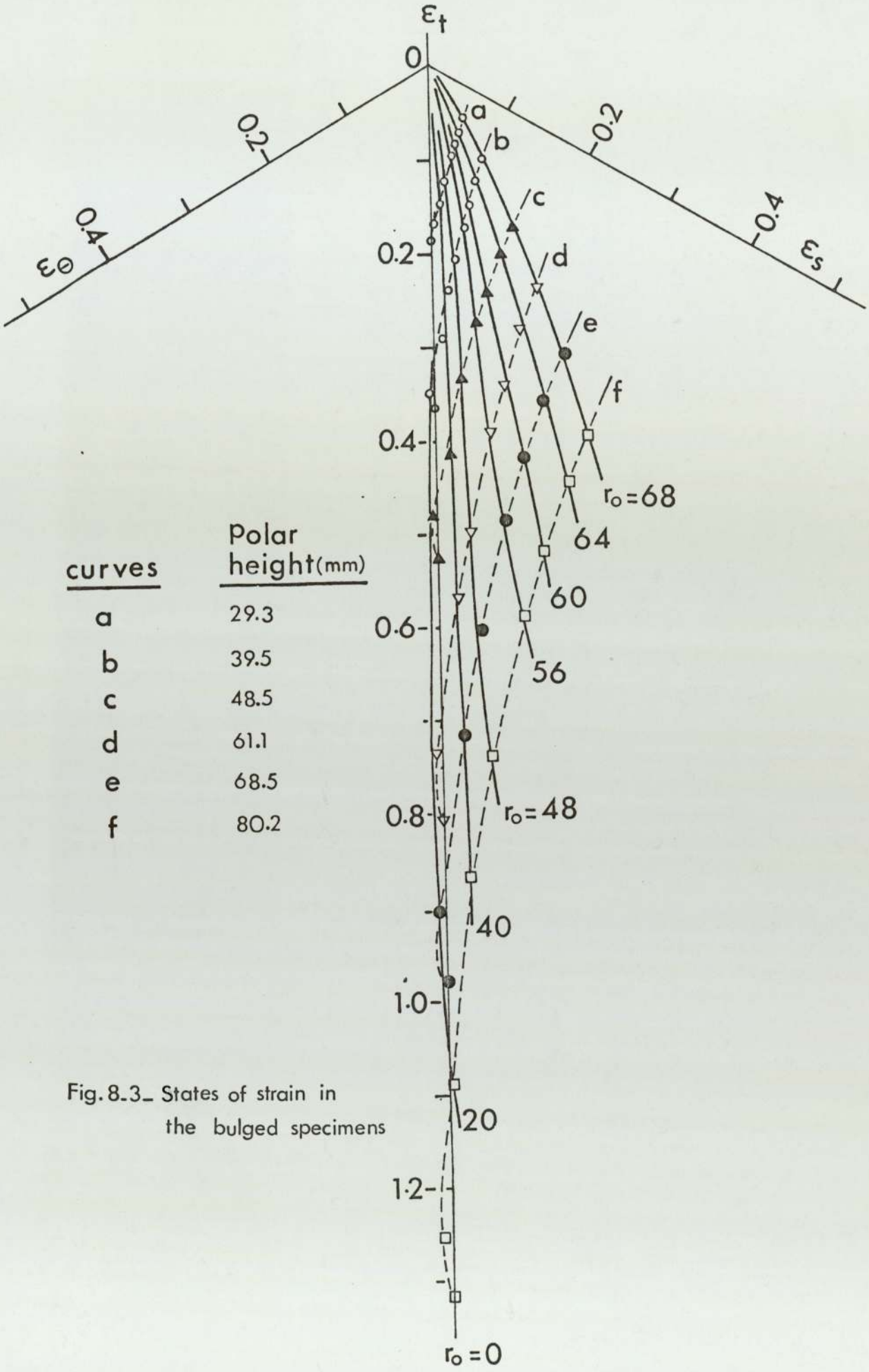

curves	Polar height(mm)
a	29.3
b	39.5
c	48.5
d	61.1
e	68.5
f	80.2

Fig. 8.3_ States of strain in the bulged specimens

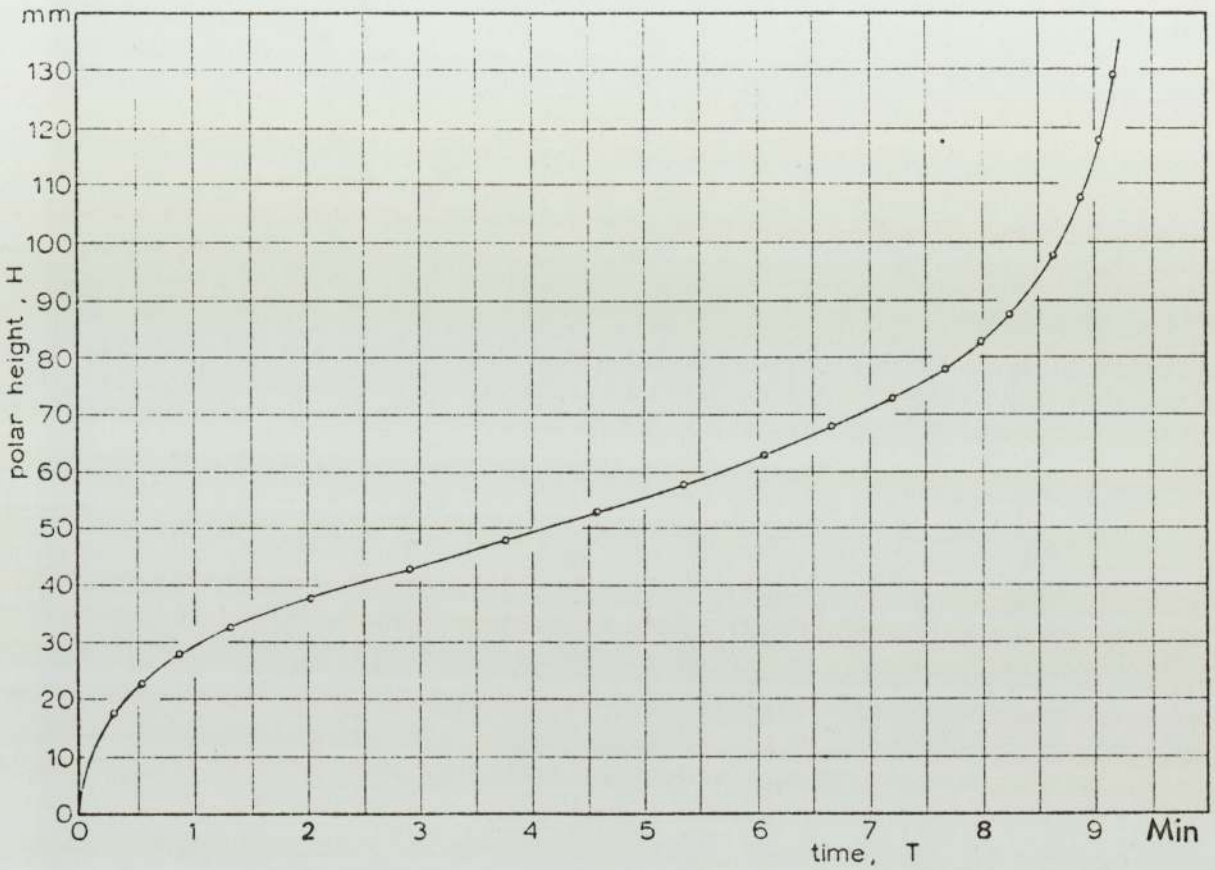

Fig.8-4- Bulge rate at constant pressure .

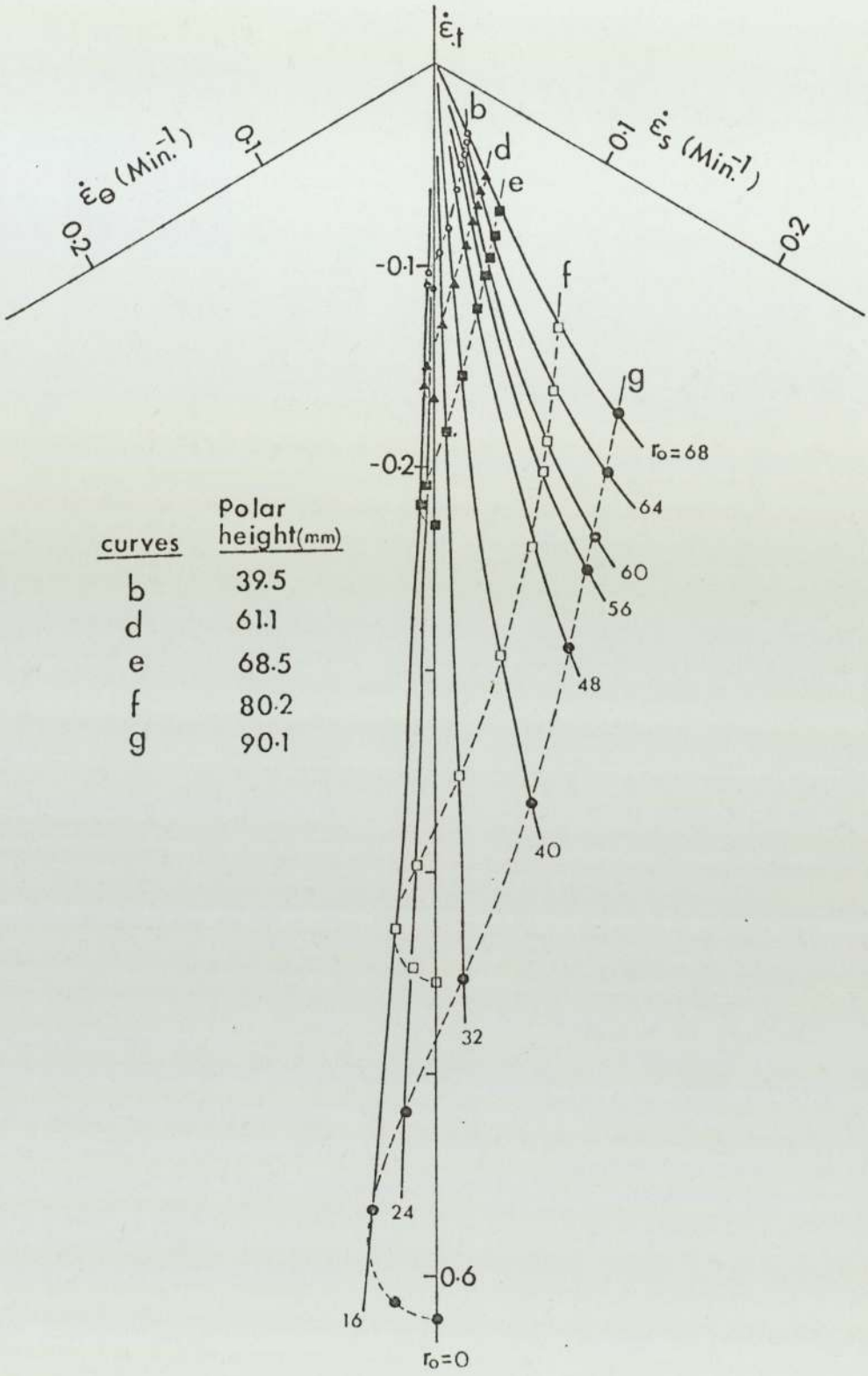

Fig. 8-5 – States of strain-rate in the bulged specimen.

CHAPTER 9

STRESS-STRAIN AND STRESS-STRAIN-RATE RELATIONSHIPS IN THE BULGE TEST

Chapter 9

Stress-strain and stress-strain rate Relationships in the Bulge Test

As described in Section (4.5), the stress, strain and strain-rate relationships of the material during deformation can be derived by superposing the three sets of triangular coordinate for stress, strain and strain-rate one into the other; and study the relationships in vectorial form. Thus, in the bulge test of superplastic material in which the deviatoric stress distribution curves are spaced between 5 and 7 o'clock as shown in Figs. (7.9) and (7.10), there are infinite numbers of such relationships along the entire bulge profile which can be expressed in vectorial form.

In the past papers on the bulge test of superplastic material (56 - 61), (64), (66 - 69), flow stress is assumed to be a unique function of strain-rate and any strain dependence is neglected. As a starting point in this chapter, let us investigate the validity of such an assumption by studying the stress-strain-rate relationship at the pole of the bulge, which is subjected to balanced biaxial stretching.

Since the pole of the bulge has zero prolateness (N = 1), the effective stress is simply the meridional-tangential stress defined as:

$$\bar{\sigma}_p = \frac{P\rho_p}{2t_p} \qquad (9.1)$$

where ρ_p is the polar curvature, and is obtained by extrapolation of the curves in Fig. (6.13). The effective strain-rate is the through-thickness strain-rate defined as:

$$\bar{\dot{\varepsilon}}_p = \dot{\varepsilon}_t = \ln \left(\frac{t_p}{t_o}\right) \qquad (9.2)$$

The variation of stress against strain rates is shown in Fig. (9.1) on the logarithmic scale for different constant pressures. Some features of the flow stresses and strain-rates are noticeable in this figure. As deformation proceeds, the stress in the diaphragm decreases, reaches a minimum and then increases rapidly. Similarly, the strain-rate in each test decreases initially and after reaching to a minimum value, increases sharply until fracture occurs. The growth of the bulge is indicated by arrows in Fig. (9.1).

As seen in Eq. (9.1), the variations of flow stress depends only upon the variations of the term $\left(\frac{\rho_p}{t_p}\right)$, since the pressure (P) is constant. At initial stages of deformation, as the bulge expands, the polar radius of curvature decreases rapidly and consequently $\left(\frac{\rho_p}{t_p}\right)$ decreases. Further deformation causes a little change in the magnitude of both polar curvature and polar thickness. At the final stages of deformation, however, severe thinning of the material together with a decrease of prolateness cause a sudden increase of flow stress. Fig. (9.2) illustrates the

variation of $\frac{\rho_p}{t_p}$ against polar height.

The experimental curves shown in Fig. (9.1) have different slopes, whereas the general shape of the curves should be the same for any applied pressure. The cause could be one or the combination of the following factors:

(i) inaccuracy of experimental measurements at high strain-rate tests;

(ii) fluctuation of temperature during the test;

(iii) the flow stress is a function of both the strain and the strain-rate.

However, it can be shown by further analysis of the results in Fig. (9.1) that the last reason mentioned above is the most likely one. In order to investigate this point further, let us consider Specimen C in Fig. (9.1); and study its behaviour in the triangular coordinate system.

For each point on the specimen there are three vectors for $\bar{\sigma}$, $\bar{\varepsilon}$ and $\bar{\dot{\varepsilon}}$ as in Fig. (9.3), where all the three quantities (stress, strain and strain-rate) are expressed non-dimensionally as fractions of the corresponding quantities at the pole. It can readily be seen from this figure that the vector for stress lies between the strain and the strain-rate vector. The two components of the stress vector ($\bar{\sigma}_{\varepsilon}$ and $\bar{\sigma}_{\dot{\varepsilon}}$) are shown in the inset of Fig. (9.3).

The mechanical behaviour of this superplastic material is described by Eq. (4.34), which is

$$\frac{\bar{\sigma}_{\varepsilon}}{\bar{\sigma}_{\dot{\varepsilon}}} = \frac{\sin \alpha}{\sin \beta} = Z$$

where Z represents the ratio of the solid to liquid behaviour (Section 4.5). Fig. (9.4) illustrates the variation of Z in the bulged specimen. As can be seen in this figure, when Z is zero, the material behaves like a liquid, in that the deviatoric stresses are entirely proportional to the strain-rates; when Z is infinitely large, the material behaves like an ordinary ductile material insensitive to the strain-rate; and when Z is unity, the material behaves as much like a solid as like a liquid, a pure mongrel, so to speak. As can be expected, nowhere in the bulge does the material behave entirely like a solid (Z less than infinity), but it behaves like a liquid at some values of r_o. Near the pole, the material is more and more quasi-solid as r_o increases. At the point where $N = 1$, the strain and strain-rate vectors are collinear and there it is empirically impossible to differentiate and theoretically meaningless to talk about strain-proportional and strain-rate-proportional stress components. Beyond $r_o = 40$ mm the material behaves most consistently, in fact it is everywhere about twice as quasi-liquid as it is quasi-solid (N nearly equals $\frac{1}{2}$).

It is now well worthwhile to return to Eq. (2.1) where the behaviour of a superplastic material is expressed as entirely strain-rate dependent. It has been shown in this study that at least one superplastic material does not behave like that at all. The superplastic material investigated in this study not only exhibits a mixture of quasi-solid and quasi-liquid behaviour, but the proportion between these two types of behaviour changes according to the stress ratio and the relative magnitudes of the strain and the strain-rate. In defence of Eq. (2.1), however, it should be added that it was originally based on the tension test in which it was impossible to distinguish between the strain-proportional and strain-rate proportional stresses. As is shown in Figs. (9.3) and (9.4), in a biaxial stress system involving curved strain paths, the stress system consists of the above mentioned two components of stress, hence the use of Eq. (2.1) is both unnecessary and misleading. Indeed, the merit of the bulge test lies precisely in averting the need to take the simplistic view of superplastic behaviour of materials represented by Eq. (2.1).

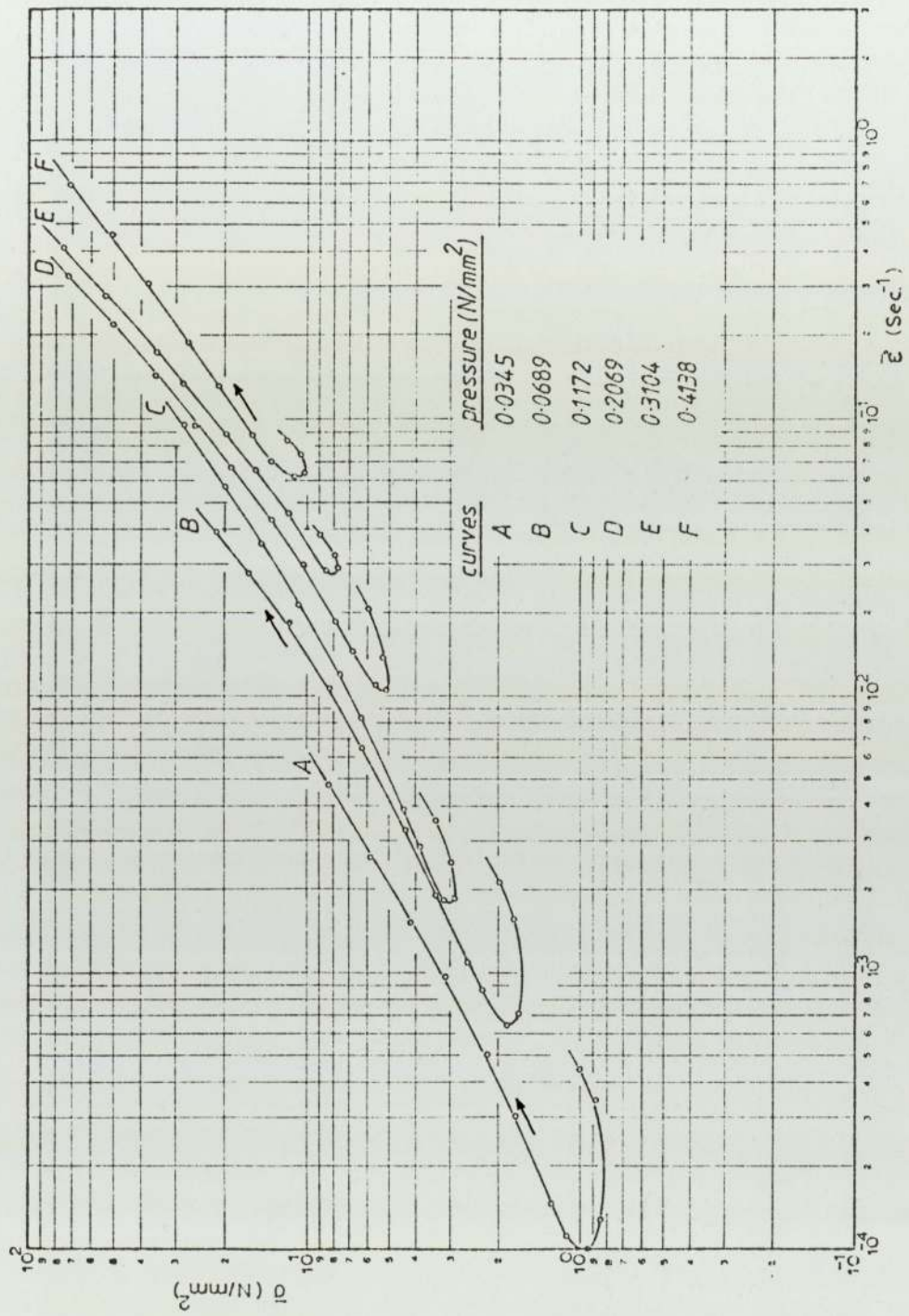

Fig. 9.1 – Effect of strain–rates on flow stress at constant pressures.

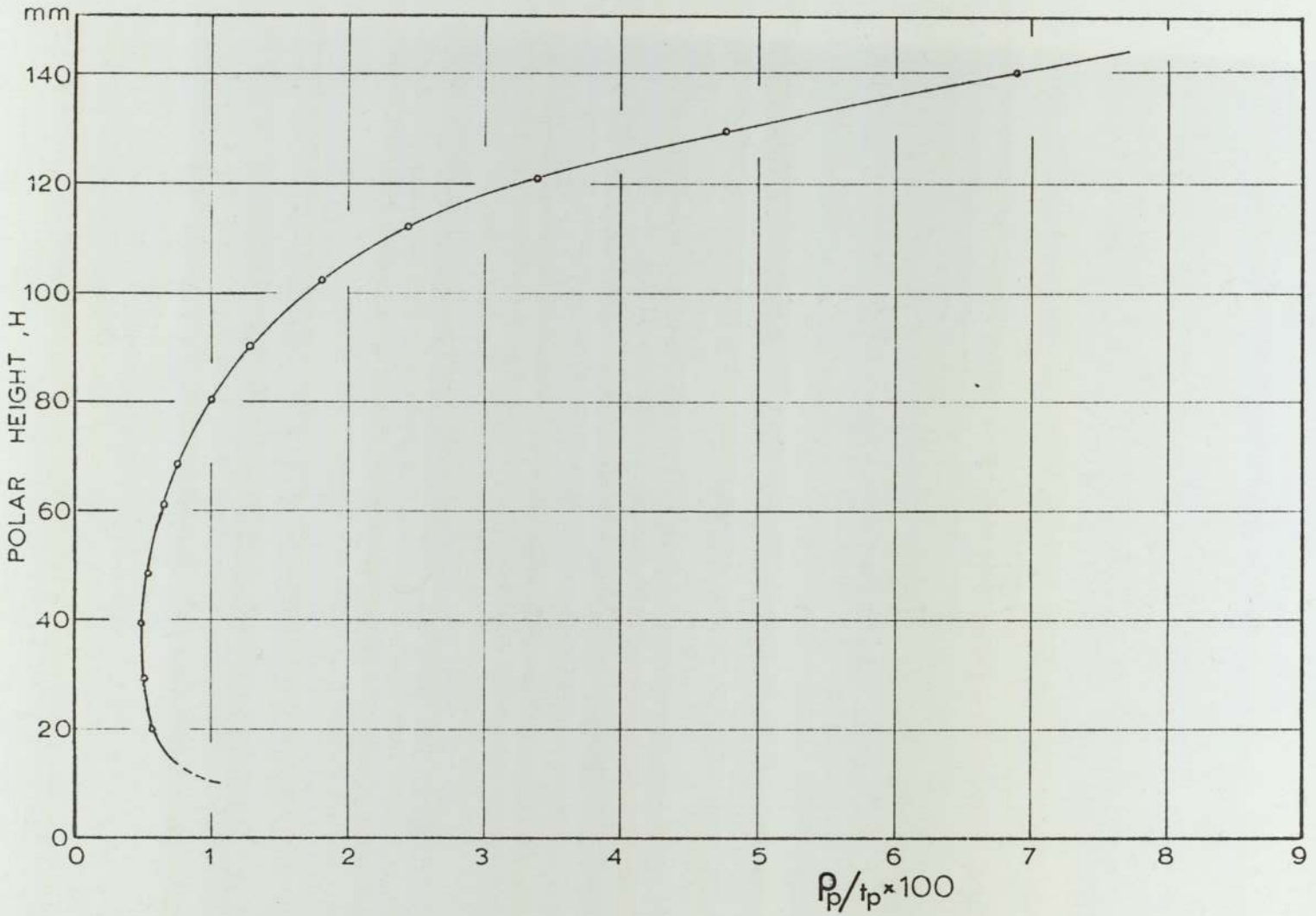

Fig.9-2- Variation of radius of curvature and thickness vs. polar height.

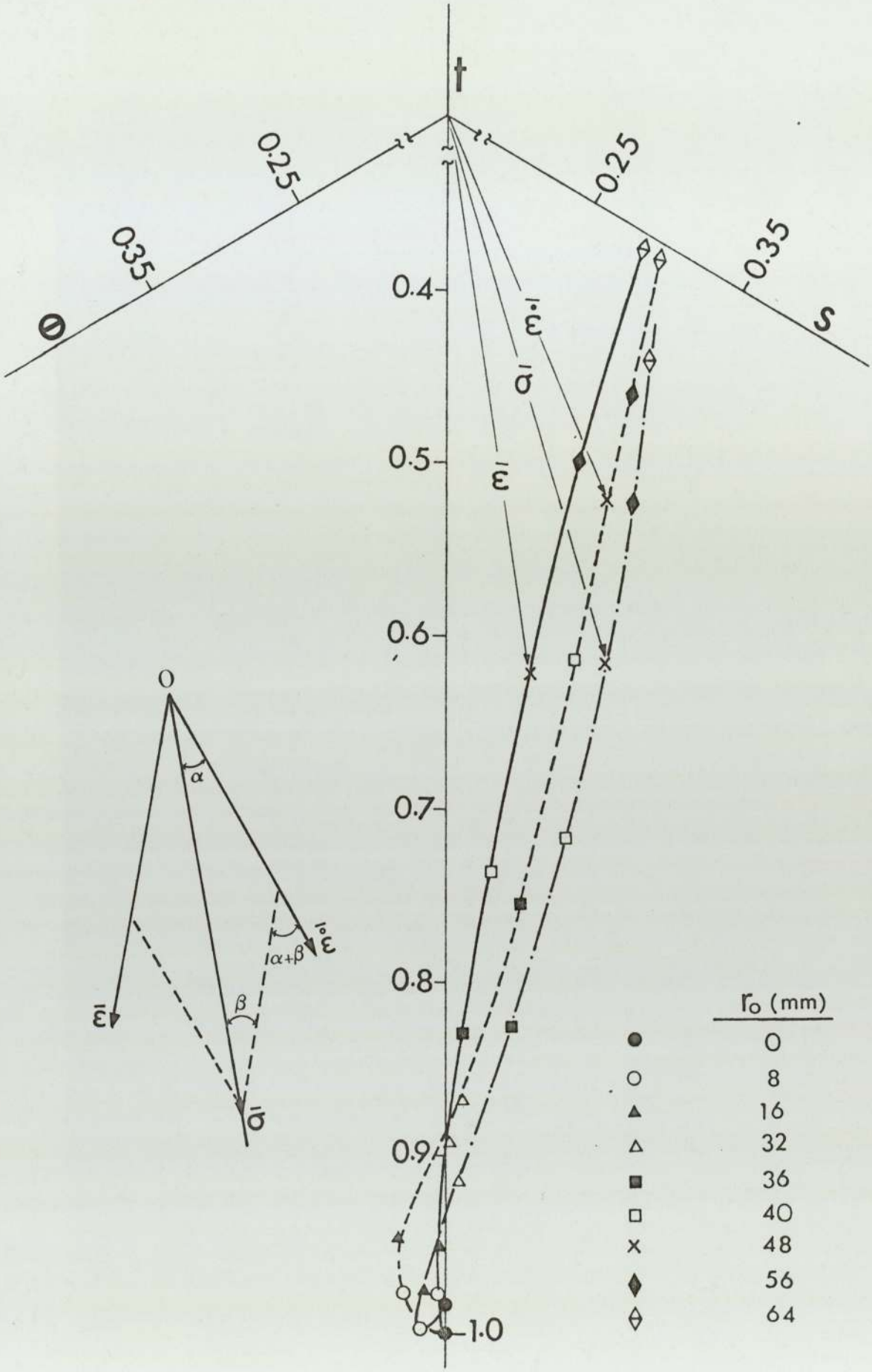

Fig. 9.3– Relationship between stress , strain and strain–rate in the specimen at the polar height of 68.5 mm .

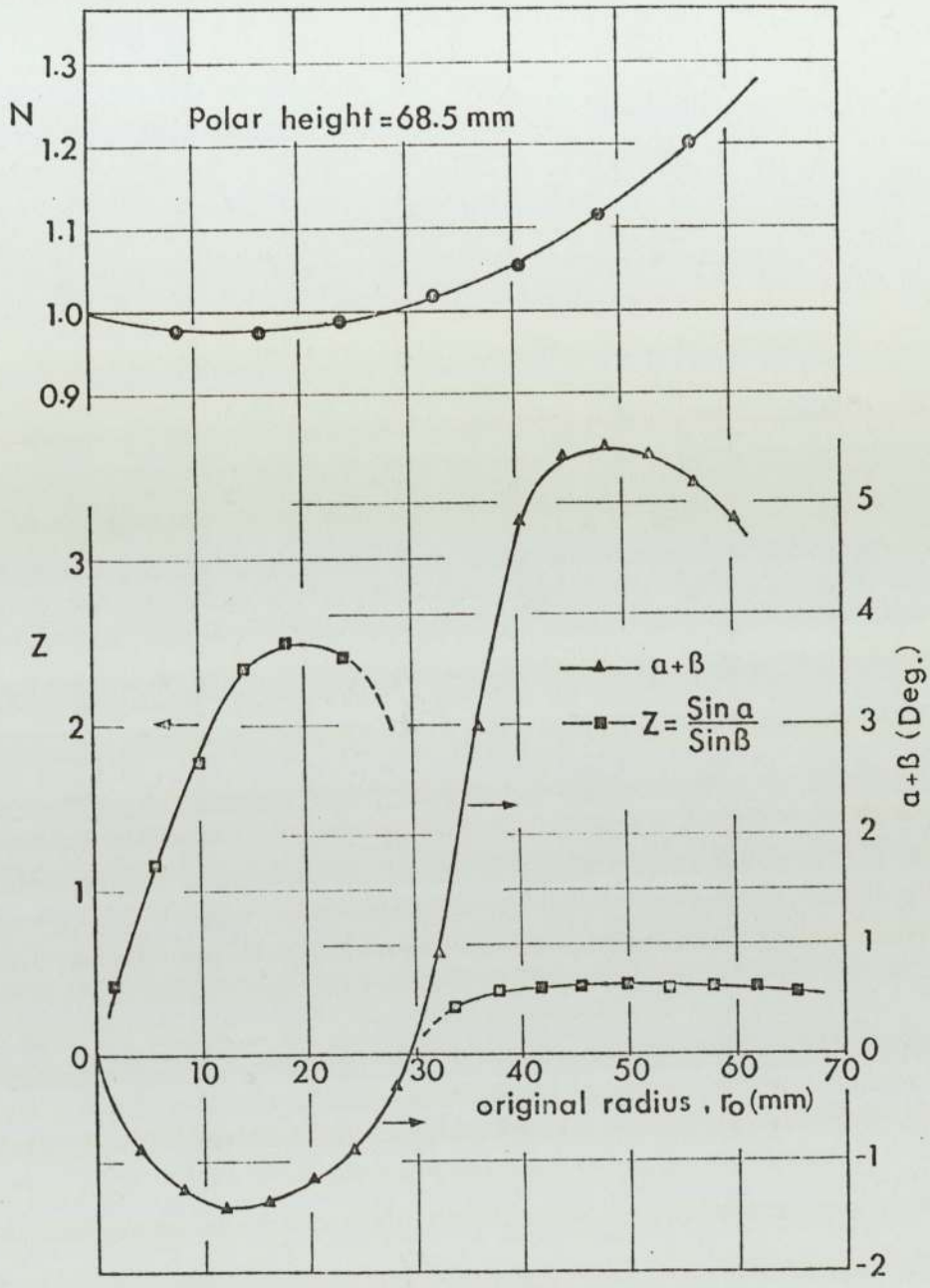

Fig. 9-4 – Ratio between the biaxial stresses and the difference between strain and strain-rate ratio.

CHAPTER 10

GENERAL CONCLUSIONS AND SUGGESTION FOR FURTHER WORK

Chapter 10

General Conclusions and Suggestion for Further Work

10.1 Conclusions

It has been shown that the simple relationship $\sigma = k\dot{\varepsilon}^m$ usually used to describe the superplastic flow in uniaxial tension test to be inadequate for biaxial stress system. The bulge test provides a suitable means of loading a superplastic sheet specimen to study the mechanical behaviour in biaxial tension. With the aid of principal curvatures the state of stress, strain and strain-rate can be accurately determined throughout the bulge test.

In this project the complex variations of the principal curvatures are measured at every point in the bulged specimen and the states of stress, strain and strain-rate are plotted in the triangular coordinate system instead of the usual Cartesian coordinate system.

In the past literature on the bulge test of superplastic materials, the surface is usually assumed to be spherical (56), (59), (64 - 67). It is shown here that such an assumption is far from being adequate in either predictive or interpretative theories. That such an assumption is inadequate is not only because the surface deviates from a sphere, but also because the exact deviation is of fundamental significance in the forming process. This

deviation is now quantitatively defined and the complexity of the geometry is revealed and measured. Another assumption which has been oversimplifying the problem is the constancy of the thickness of the whole sheet at any stage of the forming operation (56), (66). However, it is now shown that, non-uniformity in sheet thickness is an important practical consideration and in industrial applications may limit the acceptance of a particular alloy in pressure forming processes.

A method is devised and applied to present results of reporting the quasi-solid and quasi-liquid behaviour of a superplastic material under biaxial stresses, by resolving the state of stress into two components, the strain-proportional and the strain-rate-proportional components. The ratio between the magnitudes of these two components may be said to represent the relative predominance of the quasi-solid to the quasi-liquid behaviour of the material. It is found that the ratio between the quasi-solid and the quasi-liquid resistances to deformation by no means remains constant; in other words, the same material exhibits a different bias between its solid-like and liquid-like nature according to circumstances.

The data presented can form the basis of more refined predictive theories in the future, perhaps by step-by-step solutions using computer programmes, and the theoretical and experimental techniques can be used to solve specific problems. Apart from these techniques and results, however,

the final conclusion can be drawn in this project that the characteristic of axisymmetrical superplastic sheet forming by pneumatic pressure is both complex and delicate and cannot be fully observed except by careful analysis of very accurate measurements.

10.2 Suggestion for further work

The analysis presented in this thesis is applicable to co-axial deformations of superplastic materials. It may be possible to obtain some significant results on the behaviour of such materials under non-coaxial conditions. The standard bulge test using a circular die can be extended to elliptical dies and square dies with round corners. The square die may be used to draw some conclusions useful in practical forming processes. It would be of great interest if the thickness distribution of a non-circular diaphragm could be determined simply from the geometry of the bulge.

It is now clear that the behaviour of superplastic materials is not entirely strain-rate dependent. Therefore, further study of the parameters affecting superplastic flow is required, and a new relationship should be developed. The effect of grain size and temperature must be included in this relationship.

The experimental work presented in this investigation indicates clearly that the ratio between quasi-solid and

quasi-liquid resistance to deformation is never constant. Further work is, however, required to find the parameters affecting this function.

APPENDIX I

Specification of the work material

The test material used in this project was a zinc-aluminium alloy basically of eutectoid composition of 77.5% zinc - 22% Aluminium with 0.5% various additives to improve its properties, such as strength and creep resistance. The material was supplied by Imperial Smelting Corporation.

Thickness of the work material 1.27 mm, 1.91 mm and 2.54 mm

Physical Properties

Density (g/cm^3)	5.20
Specific heat ($cal/g/^oc$)	0.102
Thermal coefficient of expansion/^oC (20 - 100^oC)	22.86×10^{-6}
Electrical conductivity at 20^oC % I.A.C.S.	34
Modulus of Elasticity ($N\ mm^{-2}$)	42.76×10^3
Melting point ^oC	473
Thermal conductivity ($cal/cm^2/cm/sec/^oC$)	0.31

REFERENCES

1. W. Rosenhain, I.L. Haughton, & K.E. Bingham — "zinc alloys with aluminium and copper", J. inst. metals, 1920, 23 (1), pp. 261-324.

2. F. Hargreaves — "The ball hardness and the cold working of soft metals and eutectics", J. inst.metals, 1928, 39 (1), pp. 301-335.

3. C.H.M. Jenkins — "The strength of a cadmium-zinc and of a Tin-lead alloy solder", J. inst. metals, 1928, 40 (2), pp. 21-39.

4. C.E. Pearson — "The viscous properties of extruded eutectic alloys of lead-tine and bismuth-tin", J. inst. metals, 1934, 54, pp. 111-124.

5. E.E. Underwood — "A review of superplasticity and related phenomena", J. Metals, 1962, 14, pp. 914-919.

6. A.A. Bochvar & Z.A. Sviderkaya — "Superplasticity phenomenon in the alloys of zinc containing aluminium", IZvest. Akad.Nauk, SSSR, otdel, Tekhn, 1945, 9, pp. 821-824.

7. A.A. Presnyakov — "sverkhplasticknost metallov i splavov", Alma-Ata, 1969, Translated by Dr. C.B. Marinkov British Library Board, 1976.

8. F. Sauerwald — "on very ductile zinc-aluminium alloys", Archiv fur Metallkunde, 1949, 3 (5), pp. 165-173.

9. D. Oelschlagel — "Superplasticity in metals", J. Japan Inst. Metals, 1966, 6, pp. 11-20.

10. C.M. Packer & O.D. Sherby — "An interpretation of the superplasticity phenomenon in Two-phase alloys", Trans. A.S.M., 1967, 60, pp. 21-28.

11. A.A. Presnyakov & V.V. Chervyakova — "The phenomenon of super-plasticity in the aluminium-copper system", Izvest. Akad. Nauk, SSSR, 1958, (Tekhn), 3, pp. 120-121.

12. A.A. Presnyakov & V.V. Chervyakova — "On the super-ductility of alloys", Fizika Metallov i metallovedenie, 1959, 8 (1), pp. 114-121.

13. A.A. Presnyakov & G.V. Starikova — "Condition for the occurrence of superplasticity in cast eutectics", Izvest.Akad. Nauk, SSSR, Met. i. Topl., 1959, (Tekhn), 1, pp. 75-77.

14. A.A. Presnyakov & V.V. Chervyakova — "The superplasticity of eutectoid alloys of aluminium and zinc", Izvest.Akad.Nauk SSSR, Met. i. Topl., 1960, (Tekhn), 3, pp. 92-98.

15. W.A. Backofen, I.R. Turner & D.H. Avery — "Superplasticity in an Al-zn alloy", Trans. A.S.M. Guart, 1964, 57, pp. 980-990.

16. H.W. Hayden, R.C. Gibson & J.H. Brophy — "Superplastic metals", Scientific American, 1969, 220 (3), pp. 28-35.

17. H.W. Hayden, R.C. Gibson & J.H. Brophy — "Relationship between superplasticity and formability", Proc. Symp. on the relation between theory and practice of metal forming, Cleveland, Ohio, 1970, pp. 475-497.

18. R.B. Nicholson — "Exploitation through metallurgical development", plasticity and superplasticity; Development in their exploitation. Inst. of Metallurgists review course, Oct. 1969, pp. 19-37.

19. R.H. Johnson — "Superplasticity", Metallurgical Reviews, 1970, 15, pp. 115-134.

20. T.Y.M. Al-Naib & J.L. Duncan — "Superplasticity metal forming" Int. J. Mech. Sci., 1970, 12 (6), pp. 463-477.

21. J.W. Edington — "physical metallurgy of superplasticity", Metals Technology, 1976, 3, pp. 138-153.

22. J.W. Edington, K.N. Melton & C.P. Cutler — "Superplasticity", Progress in materials science, Pergamon Press, U.K., 1976, 21 (2), pp. 61-158.

23. S. Floreen — "Superplasticity in pure nickel", Scripta Metallurgica 1967, 1, pp. 19-23.

24. D.H. Avery & W.A. Backofen — "A structural basis for superplasticity", Trans. A.S.M. Guart., 1965, 58, pp. 551-562.

25. S.W. Zehr & W.A. Backofen — "Superplasticity in lead-tin alloys", Trans. A.S.M. Guart, 1968, 61, pp. 300-313.

26. M.J. Stowell, J.L. Robertson & B.M. Watts — "Structural changes during superplastic deformation of the Al-cu eutectic alloy", Met. Sci. J., 1969, 3, pp. 41-45.

27. P. Chaudhari — "Deformation behaviour of superplastic zn-al alloy", Acta Metallurgia, 1967, 15, pp. 1777-1786.

28. H.W. Hayden & J.H. Brophy — "The interrelation of grain size and superplastic deformation in Ni-Cr-Fe alloys", Trans. A.S.M. Guart., 1968, 61, pp. 542-549.

29. T.G. Langdon — "Grain boundary sliding as a deformation mechanism during creep", Phil. Mag., 1970, 22, pp. 689-700.

30. J. Weertman — "Theory of steady-state creep based on dislocation climb", J. Appl.Phys., 1955, 26 (10), pp. 1213-1221.

31. C.A.P. Horton & C.J. Beevers — "Anisotropy of grain boundary sliding in zinc bi-crystals examined in terms of a dislocation climb-glide mechanism", Acta Metallurgia, 1968, 16, pp. 733-741.

32. R. Raj & M.F. Ashby — "On grain boundary sliding and diffusional creep", Met. Trans. 1971, 2, pp. 1113-1127.

33. C.M. Packer, R.H. Johnson & O.D. Sherby — "Evidence for the importance of crystallographic slip during superplastic deformation of eutectic zinc-aluminium", Trans. A.I.M.E., 1968, 242, pp. 2485-2489.

34. R.H. Johnson, C.M. Packer, L. Anderson & O.D. Sherby — "Microstructure of superplastic alloys", Phil. Mag., 1968, 18, pp. 1309-1314.

35. A. Ball & M.M. Hutchinson — "Superplasticity in the aluminium-zinc eutectoid", Metal. Sci. J., 1969, 3, pp. 1-7.

36. R.C. Gifkins — "The measurement of grain boundary sliding in polycrystalline specimens", Metal Sci. J., 1973, 7, pp.15-19.

37. A.K. Mukherjee — "The rate controlling mechanism in superplasticity" Mater. Sci. Eng., 1971, 8 , pp. 83-89.

38. J. Gittus — "Creep, Viscoelasticity and creep fracture in solids", Applied Science Publisher Ltd. London, 1975, pp. 509-554.

39. M.F. Ashby & R.A. Verral — "Diffusion-Accommodated flow and superplasticity", Acta Metal., 1973, 21, pp. 149-163.

40. P.M. Hazzledine & D.E. Newbury — "A model for micrograin superplastic flow", Proc. Conf. on the microstructure and design of alloys, Cambridge, Aug. 1973, 1 (41), pp. 202-206.

41. A. Sauveur — "What is steel - another answer", Iron Age, 1924, 113, pp. 581-588.

42. M.G. Lozinsky & I.S. Simeonova — "Super-high ductility of commercial iron under cyclic fluctuations of temperature", Acta Met. 1959, 7, pp.709-715.

43. M. De Jong & G.W. Rathenau — "Mechanical properties of iron and some iron alloys while undergoing allotropic transformation", Acta Met., 1959, 7, pp. 246-253.

44. F.W. Chinard & O.D. Sherby — "Strength of iron during allotropic transformation", Acta Met., 1964, 12, pp. 911-919.

45. G.W. Greenwood & R.H. Johnson — "The deformation of metals under small stresses during phase transformation", Proc. Roy. Soc., 1965, 283A, pp. 403-422.

46. D. Oelschlagel V. Weiss — "Superplasticity of steel during the Ferite $\rightleftarrows$ Austerite transformation", Trans. A.S.M. Guart, 1966, 59, pp. 143-154.

47. M. De Jong & G.W. Rathenau — "Mechanical properties of an iron-carbon alloy during allotropic transformation", Acta Met. 1961, 9, pp. 714-720.

48. R.C. Lobb, E.C. Sykes & R.H. Johnson — "The superplastic behaviour of anisotropic metals thermally cycled under stress", Met. Sci. J., 1972, 6, pp. 33-39.

49. S.T. Konobeevsky, N.F. Pravdyuk & V.I. Kutaitsev — "The effect of irradiation on the structure and properties of structural materials", Int. Conf. Peaceful uses of atomic energy, 1955, Paper (8/P/680), 5 pp.

50. A.C. Roberts & A.H. Cottrell — "Creep of alpha uranium during irradiation with neutrons", Phil. Mag., 1956, 1, pp.711-717.

51. R. Kot & V. Weiss — "transformation plasticity in iron-nickel alloy", Met.Trans. 1970, 1, pp. 2685 - 2693.

52. L.F. Porter & R.C. Rosenthal — "effect of applied tensile stress on phase transformation in steel", Acta Met., 1959, 7, pp. 504-514.

53. H.P. Sattler & G. Wasserman — "Transformation plasticity during the martensitic transformation of iron with 30% Ni", J. Less Common Metals, 1972, 28, pp. 119-140.

54. G.R. Yoder & V. Weiss — "Superplasticity in eutectoid steel", Met. Trans., 1972, 3, pp. 675-681.

55. F.A. Mohamed, M.M.I. Ahmed & T.G. Langdon — "Factors influencing ductility in the superplastic zn - 22% al eutectoid" Met. Trans. A, 1977, 8A, pp. 933-938.

56. F. Jovane — "An approximate analysis of the superplastic forming of a thin circular diaphragm", Inst. J. Mech. Sci., 1968, 10, pp. 403-427.

57. T.H. Thomsen, D.L. Holt & W.A. Backofen — "Forming superplastic sheet metal in bulging dies", Metals Eng. Quart., 1970, 10, (2), pp. 1-7.

58. J. Hestbech, E.W. Langer & A. Rosen — "Bulging of the eutectoid zn-al alloy", J. Inst. Metals, 1971, 99, pp. 306-309.

59. D.L. Holt — "An analysis of the bulging of a superplastic sheet by lateral pressure", Int. J. Mech. Sci., 1970, 12, pp. 491-497.

60. W. Johnson, T.Y.M. Al-Naib & J.L. Duncan — "Superplastic forming techniques and strain distribution in a zn-al alloy", J. Inst. Metals, 1972, 100, pp. 45-50.

61. G.J. Cocks, G. Rowbottom & D.M.R. Taplin — "Bulge-forming characteristics of two superplastic copper alloys", Metal Technology, 1976, 3, pp. 332-337.

62. G.G.W. Clemas, S.T.S. Al-Hassani & W. Johnson — "The bulging of a superplastic sheet from a square die", Int. J. Mech. Sci., 1975, 17, pp. 711-718.

63. S. Tang — "Analysis of superplastic forming of Titanium sheet into shallow hat-section", Structures, Stuctural dynamics and Materials Conference, American Inst. Aeronautics & Astronautics Inc., 1978, pp. 256-261.

64. G.C. Cornfield & R.H. Johnson — "Forming of superplastic sheet metal", Int. J. Mech. Sci., 1970, 12 (6), pp. 479-490.

65. S. Tang & T.L. Robbins — "Bulging rupture of a superplastic sheet", Trans. A.S.M.E. J. Eng. Mater. Tech. Series H, 1974, 96 (1), pp. 77-79.

66. J.A. Belk, — "A quantitative model of the blow-forming of spherical surfaces in superplastic sheet metal", Int. J. Mech. Sci., 1975, 17, pp. 505-511.

67. J.F. Brandon, H. Lecoanet & C. Oytana — "A new formulation for the bulging of viscous sheet materials", Int. J. Mech. Sci., 1979, 21, pp. 379-386.

68. J.P. Lechten, J.C. Patrat & B. Baudelet — "Theoretical and experimental analysis of the bulge test in superplastic region", Revue de physique appliquee, 1977, 12, pp. 7-14.

69. I.H. Wilson, J.L. Duncan & W. Johnson — "Biaxial creep testing", J. Mech. Eng. Sci., 1971, 13 (6), pp. 397-403.

70. T.C. Hsu, H.M. Shang, T.C. Lee & S.Y. Lee — "Flow stresses in sheet material formed into nearly spherical shapes", Trans. A.S.M.E., J. Eng. Mat. Tech. Series H., 1975, 97 (1), pp. 57-65.

71. Z. Marcinial — "Graphical representation of stress and strain", Nadbitka Z Archivum Mechaniki Stosowanej, 1951, pp. 261-273.

72. T.C. Hsu — "The characteristics of coaxial and non-coaxial strain paths", J. Strain Analysis, 1966, 1 (3), pp. 216-223.

73. T.C. Hsu — "The effect of the rotation of the stress axes on the yield criterion of prestrained materials", A.S.M.E. Winter Annual Meeting, Chicago, 1965, Paper No. 65-WA/Met-4.

74. T.C. Hsu, W.R. Dowle, C.Y. Choi & P.K. Lee — "Strain histories and strain distributions in a cup drawing operation", A.S.M.E. Winter Annual Meeting, New York, 1970, Paper No.70-WA/ Prod.-6.

75. P.K. Lee, C.Y. Choi & T.C. Hsu — "Effect of draw-in on formability in axisymmetrical sheet metal forming", A.S.M.E. Winter Annual Meeting, New York, 1972, Paper No. 72-WA/ Prod - 1.

76. T.C. Hsu — "Some remarks on sheet metal formability and its measurement", Proc. Int. Conf. on Mechanical Behaviour of Materials, Japan, Aug. 1971, 1, pp. 206-217.

77. T.C. Hsu — "Present scope and future trend of sheet metal forming research", Int. J. Prod. Res., 1974, 12 (1), pp. 99-115.

78. R. Hill — "The mathematical theory of plasticity", Oxford Clarendon Press, 1950.

79. K. Nuttal — "The relationship between microstructure and mechanical properties of the super-plastic zn-al eutectoid alloy", Ph.D. Thesis, Manchester University, U.K. , 1969.

80. D.S. Fields, Jr. & J.F. Hubert — "Superplastic metal forming", Advances in deformation processing, Sagamore Army Materials Research Conf. Proceedings (21), Plenum Press, 1978, U.S.A.

81. W.B. Morrison — "The elongation of superplastic alloys", Trans. A.I.M.E. 1968, 242, pp. 2221-2227.

82. P. Lukac & P. Malek — "Superplasticity in a zn-al alloy", 5th Inter. Conf. on the strength of metals and alloys, Aachen, West Germany, Aug. 1979, 1, pp. 369-374.

83. K. Nuttall — "Superplasticity above the invariant in the eutectoid zn-al alloy", J. Inst. Metals, 1971, 99, pp. 291-292.

84. H.M. Shang & T.C. Hsu — "Deformation and curvatures in sheet metals in the bulge test", Trans. A.S.M.E. Series B, 1979, 101 (3), pp. 341-347.

85. Y. Tomita & R. Sowerby — "An approximate analysis for studying the deformation mechanics of rate sensitive materials", Int. J. Mech. Sci., 1978, 20, pp. 361-371.

86. K.A. Padmanabham & G.J. Davies — "Superplasticity", Materials Research and Engineering, Springer-Verlag, 1980, 2, 292 pp.

87. W. Johnson & P.B. Mellor — "Plasticity for Mechanical Engineers", D. Van Nostrand Co. Ltd., London, 1962,

88. A.K. Ghosh & C.H. Hamilton — "On Constant Membrane stress test for superplastic metals", Met. Trans. A, 1980, 11A, pp. 1915-1918.

89. S. Tang — "Progress in mechanics of superplasticity", Advances in Materials Technology in the Americas. San Francisco, U.S.A., Aug. 1980, 2, pp. 43-50.

90. I.M. Bidhendi & T.C. Hsu — "A Rheological Study of a superplastic sheet metal forming process", Proc. 8th Int. Congress on Rheology, Napoli/Italy, Sept. 1980, 3, pp. 585-590.

91. T.C. Hsu & I.M. Bidhendi — "A study of strain and strain-rate dependent properties of a superplastic n-al alloy under biaxial stresses", To be published in A.S.M.E.